FOI-R–0489–SE
October 2002
ISSN 1650-1942

Scientific Report

Martin Sjögren

Comparison of Spectral Element and Finite Difference Methods for Electromagnetic Wave Propagation over a Material Discontinuity

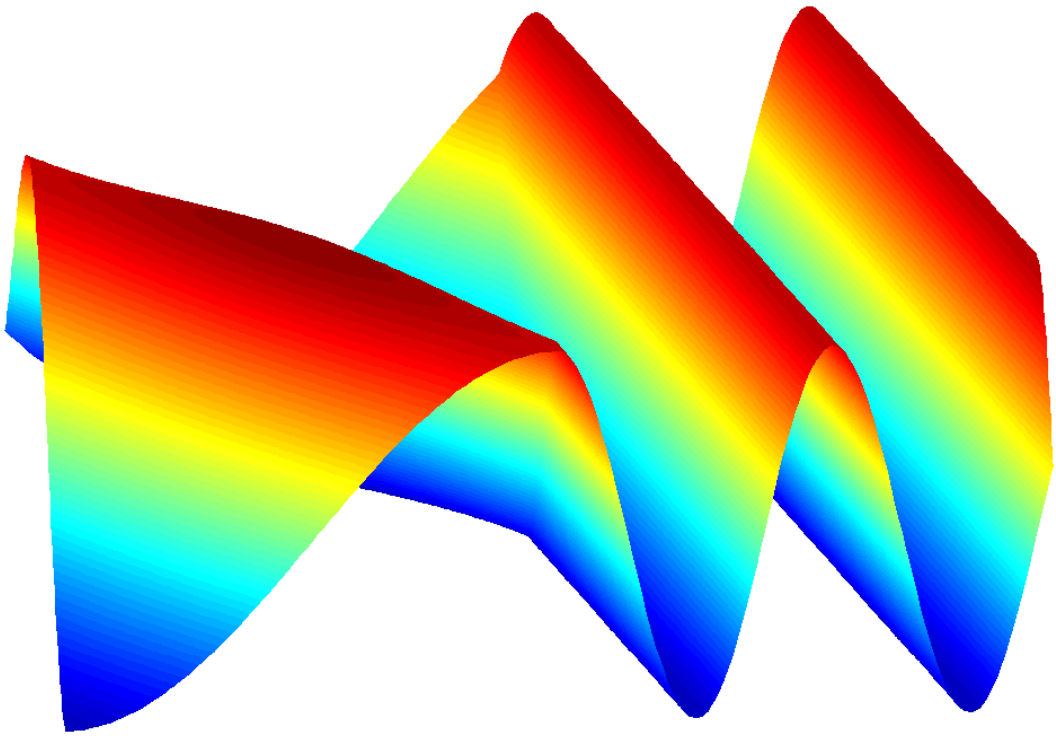

Division of Aeronautics, FFA
SE-172 90 STOCKHOLM

FOI – Swedish Defence Research Agency
Division of Aeronautics, FFA
SE-172 90 STOCKHOLM

FOI-R–0489–SE
October 2002
ISSN 1650-1942

Scientific Report

Martin Sjögren

Comparison of Spectral Element and Finite Difference Methods for Electromagnetic Wave Propagation over a Material Discontinuity

Division of Aeronautics, FFA
SE-172 90 STOCKHOLM

Abstract

In this report, Maxwell’s equations are solved for the case of an electromagnetic wave propagating over a material discontinuity. The numerical calculation of the solution to the problem is performed with a high-order spectral element method on an unstructured grid as well as with a high-order finite difference method on a structured grid. The results and errors of the two computations are compared, and efficiency, long-time stability and the order of accuracy are analyzed.

Contents

1 Introduction

Technological applications such as stealth design of aircraft, development of high-speed optical communication systems for computing, and analysis of the radiation from cellphone antennas all depend on the theories of electromagnetism. The equations that govern these, and a vast amount of other, physical phenomena are the Maxwell equations, formulated in the late 1800's. Since only a small fraction of the posed electromagnetic problems are analytically solvable, the development of good numerical approximate solutions of the equations is of significant importance. There is a variety of different numerical methods that deal with Maxwell's equations. Two methods that are used to solve time-dependent problems with high demands on accuracy are the high-order finite difference time domain method (FDTD) and the high-order spectral element method. These two methods will in this report be applied on a simple electromagnetic reflection-refraction problem and the results of the two will be evaluated and compared. An emphasis will be put on the efficiency and long-time stability of the methods.

The situation treated in this report, where electromagnetic waves are reflected by material interfaces, is of uttermost significance when the desired applications are radar signatures of aircraft and other vehicles. Being able to correctly represent material coatings in the computations is vital for the radar cross section calculations in the aim for stealthy moving objects.

2 Problem Description

2.1 General Formulation of Electromagnetics

The foundations of electromagnetics, upon which all specific applications rest, are the well-known Maxwell equations

$$\boldsymbol{\nabla} \times \boldsymbol{E} = -\frac{\partial \boldsymbol{B}}{\partial t}, \tag{2.1a}$$

$$\boldsymbol{\nabla} \times \boldsymbol{H} = \boldsymbol{J} + \frac{\partial \boldsymbol{D}}{\partial t}, \tag{2.1b}$$

$$\boldsymbol{\nabla} \cdot \boldsymbol{D} = \rho, \tag{2.1c}$$

$$\boldsymbol{\nabla} \cdot \boldsymbol{B} = 0. \tag{2.1d}$$

Here, $\boldsymbol{E}$ $[V/m]$ and $\boldsymbol{H}$ $[A/m]$ are the electric and magnetic field intensities, $\boldsymbol{D}$ $[C/m^2]$ and $\boldsymbol{B}$ $[T]$ the electric and magnetic flux densities, $\boldsymbol{J}$ $[A/m^2]$ the electric current density, and ρ $[C/m^3]$ is the density of electrical charges.

The electromagnetic quantities are in general distributed in some sort of material other than vacuum. A material can be electromagnetically characterized by its permittivity ϵ $[F/m]$ and permeability μ $[H/m]$. In general, ϵ and μ are rather complicated complex tensors, but for a simple medium, i.e. an isotropic, homogeneous, time-invariant and linear material, they simplify to real scalar constants. The absolute permittivity ϵ and the absolute permeability μ are related to the free-space values $\epsilon_0 \approx 8.854 \cdot 10^{-12}$ F/m and $\mu_0 = 4\pi \cdot 10^{-7}$ H/m, by the dimensionless constants called relative permittivity ϵ_r and relative permeability μ_r by $\epsilon = \epsilon_0 \epsilon_r$ and $\mu = \mu_0 \mu_r$. When glancing through tables of material properties, the relative values, ϵ_r and μ_r, are the ones you are most likely to find.

Combining the permittivity and the permeability of a material one reaches another common parameter that describes a material, i.e. the intrinsic impedance

$$\eta = \sqrt{\frac{\mu}{\epsilon}}. \tag{2.2}$$

The absolute permittivity and permeability relate the electromagnetic intensities and flux densities by

$$\boldsymbol{D} = \epsilon \boldsymbol{E}, \tag{2.3a}$$

$$\boldsymbol{B} = \mu \boldsymbol{H}. \tag{2.3b}$$

Another characteristic quantity for a material is its conductivity σ $[S/m]$. This parameter relates the current density to the electric field strength in a material,

$$\boldsymbol{J} = \sigma \boldsymbol{E}. \tag{2.4}$$

To solve Maxwell's equations generally, boundary conditions are needed. With a boundary surface S separating the regions 1 and 2 such as in Figure 2.1, where

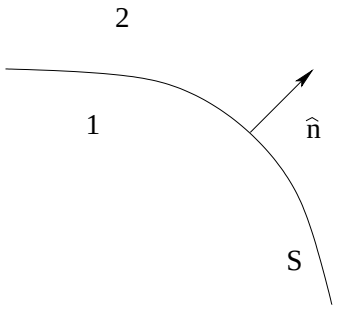

Figure 2.1. Schematic picture of two regions separated by a surface S. The normal $\hat{\boldsymbol{n}}$ points out of region 1 into region 2.

the normal unit vector $\hat{\boldsymbol{n}}$ is pointing out from region 1, the following boundary condition relations evolve:

$$\hat{\boldsymbol{n}} \times (\boldsymbol{E}_1 - \boldsymbol{E}_2) = 0, \tag{2.5a}$$

$$\hat{\boldsymbol{n}} \times (\boldsymbol{H}_1 - \boldsymbol{H}_2) = \boldsymbol{J}_S, \tag{2.5b}$$

$$\hat{\boldsymbol{n}} \cdot (\boldsymbol{D}_1 - \boldsymbol{D}_2) = \rho_S, \tag{2.5c}$$

$$\hat{\boldsymbol{n}} \cdot (\boldsymbol{B}_1 - \boldsymbol{B}_2) = 0. \tag{2.5d}$$

Here, $\boldsymbol{J}_s\ [A/m]$ is the surface current density on the surface S and $\rho_s\ [C/m^2]$ is the surface charge density on S.

In perfectly conducting materials the electric charges are totally free, i.e. the conductivity σ is infinite. Had we introduced a set of free electrons in the interior of the material, an electric field would have been set up, repelling the charges. Because of the unlimited mobility of the charges, they would continue to move away from each other until they reach the conductor surface. Hence, a perfect conductor has no interior charges, and all charges reside on the surface of the material. Since no charges are located within the material, there can be no current flowing there, but the charges on the surface may conduct a surface current. So, for a perfect electric conductor

$$\rho = 0, \quad \boldsymbol{J} = \boldsymbol{0}, \tag{2.6}$$

however, the charge and current densities can instead be expressed on the surface of the material by ρ_S and $\boldsymbol{J}_S$.

On the other hand, most real physical materials do not show the property of infinite conductivity. The electric forces from the atomic nuclei in combination with their electron clouds also interact with the charge carrying electrons. These forces prevent the mobile electrons from being totally free, and hence the conductivity becomes finite. This allows the mobile electrons to distribute themselves within the material, and the charge and current distributions can be described by ρ and $\boldsymbol{J}$ only. In the case of such a non-perfect conductor, neither surface charges nor surface currents will exist in the material, i.e.

$$\rho_S = 0, \quad \boldsymbol{J}_S = \boldsymbol{0}. \tag{2.7}$$

2.2 Scaling of Quantities

For reasons of convenience when we are correlating small wavelengths to large frequencies, it is advantageous to transform all the electromagnetic quantities to

dimensionless quantities. We will choose a characteristic length L, typically the size of a wavelength, to scale the coordinates, and the speed of light in vacuum, $c_0 = \frac{1}{\sqrt{\epsilon_0 \mu_0}} \approx 3 \cdot 10^8 \; m/s$, to make time dimensionless

$$x = \frac{x_d}{L}, \tag{2.8a}$$

$$t = \frac{c_0 t_d}{L}. \tag{2.8b}$$

The subscript d indicates the physical quantity in the correct dimensional unit.

Making the material parameters non-dimensional is simple, we just divide them by the vacuum values, i.e. $\epsilon = \frac{\epsilon_d}{\epsilon_0} = \epsilon_r$ and $\mu = \frac{\mu_d}{\mu_0} = \mu_r$. This together with the transformations

$$\boldsymbol{E} = \frac{\boldsymbol{E}_d}{E_0}, \tag{2.9a}$$

$$\boldsymbol{H} = \frac{\sqrt{\mu_0}\boldsymbol{H}_d}{\sqrt{\epsilon_0}E_0}, \tag{2.9b}$$

$$\boldsymbol{J} = \frac{\sqrt{\mu_0}\boldsymbol{J}_d L}{\sqrt{\epsilon_0}E_0}, \tag{2.9c}$$

where E_0 is a characteristic electric field amplitude, make all the entries in Maxwell's equations dimensionless. Equations (2.1a) - (2.5d) remain true as long as we use the scaling factors described above. These equations should have had all quantities indexed by the subscript d had we wanted to be stringent, but they have been left out in order to conserve the usual appearance of Maxwell's equations.

The relation between the dimensional speed of light c_d, the dimensional wavelength λ_d and the dimensional frequency f_d is $c_d = f_d \lambda_d$. Wavelength scales as $\lambda = \frac{\lambda_d}{L}$ since it is a length measure, and frequency scales as $f = \frac{f_d L}{c_0}$ since it has the dimensions of $[\text{time}]^{-1}$. This means that $c \equiv f\lambda = \frac{c_d}{c_0} = \frac{1}{\sqrt{\epsilon\mu}}$, i.e. in practice we have a scaled dimensionless speed of light c, where $0 < c \leq 1$, and the case where c is unity is where the light travels in vacuum.

The remainder of this report will contain these dimensionless, scaled electromagnetic quantities only.

2.3 Problem Specifics

In order to compare two different numerical schemes, and to be able to relate these to an analytical solution, it is necessary to construct a simple sample problem. It is possible to include the non-trivial physical processes of reflection and refraction of an electromagnetic wave in a simple geometry and still keep an analytical pen-and-paper solution as reference. Hence, we let the physical problem to be solved in our case be a two-dimensional reflection-refraction situation where a plane electromagnetic wave encounters a material discontinuity. As aircraft often are coated by different reflection absorbing materials, this is a significant problem when thinking in terms of radar signatures.

In Figure 2.2 our incoming plane wave first propagates in material 1 in the left half-plane $x < 0$. The domain $x > 0$ on the other hand, is made up of material 2, with its own properties. Hence, at $x = 0$, there is a material discontinuity. The incident angle of the incoming plane wave to the normal of the material discontinuity is θ_i.

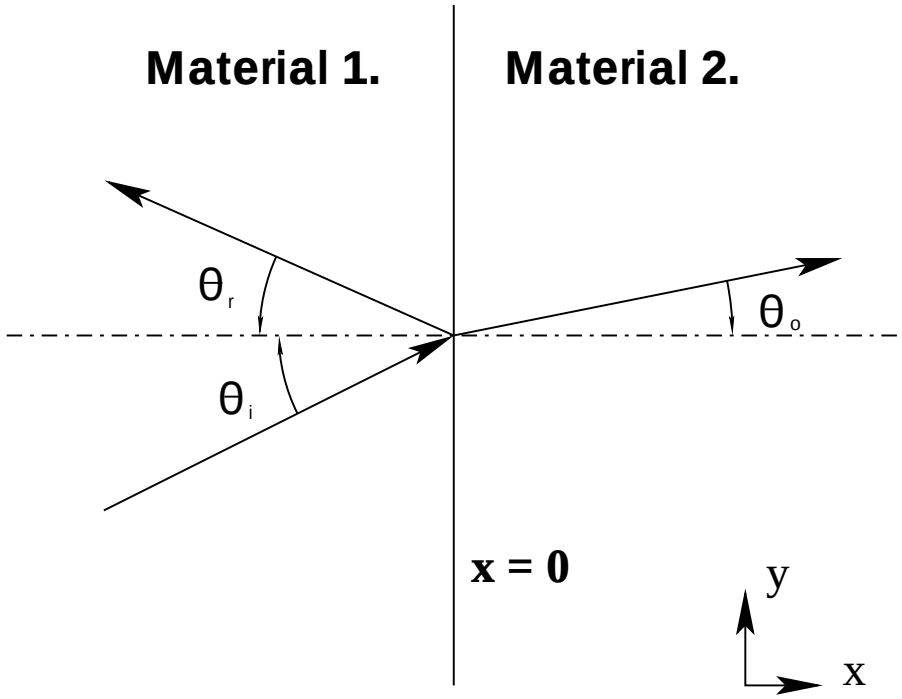

Figure 2.2. Schematic setup of the physical problem. The two materials are connected at $x = 0$, and part of the incoming EM-wave penetrates material 2, while another part bounces off the material discontinuity.

The discontinuity will split the incoming wave into two different wave components, one part of the wave will be reflected and the other refracted. The reflected wave leaves the discontinuity at an angle θ_r to the normal of the discontinuity while the refracted wave continues to travel in the forward x-direction at an angle θ_o to the surface normal.

In this particular problem we choose to deal with dielectric materials where the relative permittivities and permeabilities are $\epsilon_{r_1} = 1$, $\mu_{r_1} = 1$, $\epsilon_{r_2} = 4$, and $\mu_{r_2} = 1$. Since dielectrica support no free currents, $\sigma_1 = \sigma_2 = 0$. Utilizing the scaled dimensionless quantities described in Section 2.2, this means that we will have a speed of light $c_1 = 1$ in material 1, and a speed of light $c_2 = 0.5$ in the second material. We choose a dimensionless frequency of 1 and remember that the frequency of a wave is constant independent of material (see Section 2.4.1), so that $f_1 = f_2 = 1$. This gives a constant angular frequency $\omega = \omega_1 = \omega_2 = 2\pi$. This choice of frequency leads us to a dimensionless wavelength of $\lambda_1 = 1$ in medium 1, and a wavelength of $\lambda_2 = 0.5$ in medium 2.

To make this problem suitable for computational purposes, we will size the computational domain according to our choice of wavelengths. We restrict ourselves to the dimensionless region $-1 < x < 1$, $0 < y < 1$, the length scale of which is one wavelength λ_1 in medium 1, and two wavelengths λ_2 in medium 2.

We have now described the problem in dimensionless terms. For the remainder of this report, all quantities used will be dimensionless and based on these dimen-

sionless premises.

The full set of Maxwell equations, (2.1a)-(2.1d), can be reduced to the first two equations (2.1a) and (2.1b) in combination with the continuity equation,

$$\boldsymbol{\nabla} \cdot \boldsymbol{J} + \frac{\partial \rho}{\partial t} = 0, \tag{2.10}$$

by making the physically reasonable assumptions that

$$\boldsymbol{B}(\boldsymbol{r}, t = -\infty) = \boldsymbol{D}(\boldsymbol{r}, t = -\infty) = \boldsymbol{0}, \quad \rho(\boldsymbol{r}, t = -\infty) = 0. \tag{2.11}$$

(2.11) states that space is chargeless and free of fields at the beginning of time, which is a sensible assumption. At some later time $t > -\infty$, electromagnetic events may occur and change the values of the field strengths and charge density, but before this happens, the electromagnetic variables above are zeroed out.

The redundancy of (2.1d) can be seen by taking the divergence of (2.1a),

$$\boldsymbol{\nabla} \cdot \big(\boldsymbol{\nabla} \times \boldsymbol{E}\big) = -\frac{\partial \big(\boldsymbol{\nabla} \cdot \boldsymbol{B}\big)}{\partial t} = 0. \tag{2.12}$$

The divergence of $\boldsymbol{B}$ is obviously constant, and since (2.11) indicates that $\boldsymbol{B}(\boldsymbol{r}, t = -\infty) = \boldsymbol{0}$, the result is that

$$\boldsymbol{\nabla} \cdot \boldsymbol{B}(\boldsymbol{r}, t) = \boldsymbol{\nabla} \cdot \boldsymbol{B}(\boldsymbol{r}, t = -\infty) = 0, \tag{2.13}$$

which means that (2.1d) follows directly from (2.1a).

Taking the divergence of (2.1b) yields

$$\boldsymbol{\nabla} \cdot \big(\boldsymbol{\nabla} \times \boldsymbol{H}\big) = \boldsymbol{\nabla} \cdot \boldsymbol{J} + \frac{\partial \big(\boldsymbol{\nabla} \cdot \boldsymbol{D}\big)}{\partial t} = 0. \tag{2.14}$$

Using the continuity equation (2.10) we know that $\boldsymbol{\nabla} \cdot \boldsymbol{J} = -\frac{\partial \rho}{\partial t}$. Substituting this into (2.14) leads to

$$\frac{\partial}{\partial t}\big(\boldsymbol{\nabla} \cdot \boldsymbol{D} - \rho\big) = 0. \tag{2.15}$$

In general we have

$$\begin{aligned} \boldsymbol{\nabla} \cdot \boldsymbol{D}(\boldsymbol{r}, t) - \rho(\boldsymbol{r}, t) = \quad & \boldsymbol{\nabla} \cdot \boldsymbol{D}(\boldsymbol{r}, t = -\infty) - \rho(\boldsymbol{r}, t = -\infty) \\ & + \int_{-\infty}^{t} \frac{\partial}{\partial t'}\big(\boldsymbol{\nabla} \cdot \boldsymbol{D} - \rho\big) dt'. \end{aligned} \tag{2.16}$$

The physical assumptions in (2.11) together with (2.15) amount to vanishing terms on the right side of the equal sign, which means that using (2.1b) and (2.10), we reach $\boldsymbol{\nabla} \cdot \boldsymbol{D} = \rho$, and we make (2.1c) redundant.

This shows that the latter two of Maxwell's equations, i.e. the divergence relations (2.1c) and (2.1d), can be viewed as consistency relations arising from the curl relations (2.1a) and (2.1b) and the continuity equation of charge conservation, (2.10).

Having reduced the vital number of Maxwell equations to two, it is also favorable to reduce the number of unknown fields to two instead of four. This is where

the constitutive material relations, equations (2.3a) and (2.3b) come in. When we deal with simple media, this becomes particularly easy. To get the total picture of how all the electric and magnetic field variables; $\boldsymbol{E}(\boldsymbol{r},t)$, $\boldsymbol{H}(\boldsymbol{r},t)$, $\boldsymbol{D}(\boldsymbol{r},t)$ and $\boldsymbol{B}(\boldsymbol{r},t)$ propagate in space and time, it suffices to look merely at the field intensities, $\boldsymbol{E}(\boldsymbol{r},t)$ and $\boldsymbol{H}(\boldsymbol{r},t)$, in combination with the material parameters.

All that needs to be done for simple media such as ours, is to rewrite the first two equations, i.e. (2.1a) and (2.1b), and then solve for $\boldsymbol{E}(\boldsymbol{r},t)$ and $\boldsymbol{H}(\boldsymbol{r},t)$ in what becomes

$$\epsilon\frac{\partial \boldsymbol{E}}{\partial t} = \boldsymbol{\nabla}\times\boldsymbol{H}, \tag{2.17a}$$

$$\mu\frac{\partial \boldsymbol{H}}{\partial t} = -\boldsymbol{\nabla}\times\boldsymbol{E}, \tag{2.17b}$$

with proper initial and boundary conditions.

In two dimensions, the equations (2.17a) and (2.17b) above decouple into two independent sets of three scalar equations. These sets are usually referred to as modes. The transverse electric mode (TE-mode) involves the quantities E_x, E_y and H_z and is written as

$$\epsilon\frac{\partial E_x}{\partial t} = \frac{\partial H_z}{\partial y}, \tag{2.18a}$$

$$\epsilon\frac{\partial E_y}{\partial t} = -\frac{\partial H_z}{\partial x}, \tag{2.18b}$$

$$\mu\frac{\partial H_z}{\partial t} = \frac{\partial E_x}{\partial y} - \frac{\partial E_y}{\partial x}, \tag{2.18c}$$

while the transverse magnetic mode (TM-mode) encapsulates the H_x, H_y and E_z-variables with the equations

$$\mu\frac{\partial H_x}{\partial t} = -\frac{\partial E_z}{\partial y}, \tag{2.19a}$$

$$\mu\frac{\partial H_y}{\partial t} = \frac{\partial E_z}{\partial x}, \tag{2.19b}$$

$$\epsilon\frac{\partial E_z}{\partial t} = \frac{\partial H_y}{\partial x} - \frac{\partial H_x}{\partial y}. \tag{2.19c}$$

These two modes exist simultaneously and independently without mutual interaction. For a general case, we need to solve both of the modes to get the complete field information. However, it is convenient to choose the coordinate system so that only one of the modes is of importance. For our particular case, where we have the propagation of a plane wave, we will let the incoming wave exist only in the transverse electric variables, $\boldsymbol{E} = E_x\hat{\boldsymbol{e}}_x + E_y\hat{\boldsymbol{e}}_y$ and $\boldsymbol{H} = H_z\hat{\boldsymbol{e}}_z$. Such a situation where the $\boldsymbol{E}$-field lies entirely in the plane of propagation is called parallel polarization. If we were to use the transverse magnetic mode, we would be utilizing perpendicular polarization instead.

2.4 Analytical Solution

Since we have defined our problem in two-dimensions and in the transverse electric mode, we are aiming for the solution of

$$\epsilon \frac{\partial E_x}{\partial t} = \frac{\partial H_z}{\partial y}, \tag{2.20a}$$

$$\epsilon \frac{\partial E_y}{\partial t} = -\frac{\partial H_z}{\partial x}, \tag{2.20b}$$

$$\mu \frac{\partial H_z}{\partial t} = \frac{\partial E_x}{\partial y} - \frac{\partial E_y}{\partial x}. \tag{2.20c}$$

The entire purpose of this report is to evaluate how well two different numerical algorithms solve this problem. The problem is nevertheless analytically solvable. We will compare the numerical solutions to this analytical solution and analyze the numerical errors that arize through discretization.

In the derivation of the analytical solution, let us not restrict ourselves to two dimensions for a while. The full three-dimensional equations of interest for simple, non-conducting media are equations (2.17a) and (2.17b). Taking the curl of these equations, and combining them, using some standard vector relations, yields the wave equations

$$\boldsymbol{\nabla}^2 \boldsymbol{E} - \frac{1}{c^2} \frac{\partial^2 \boldsymbol{E}}{\partial t^2} = 0, \tag{2.21a}$$

$$\boldsymbol{\nabla}^2 \boldsymbol{H} - \frac{1}{c^2} \frac{\partial^2 \boldsymbol{H}}{\partial t^2} = 0. \tag{2.21b}$$

Here, $c = \frac{1}{\sqrt{\mu\epsilon}}$ is the wave's speed of propagation.

Real time-harmonic solutions to the wave equations are

$$\boldsymbol{E}(\boldsymbol{r}, t) = \mathfrak{Re}[\mathbb{E}(\boldsymbol{r}) e^{j\omega t}], \tag{2.22a}$$

$$\boldsymbol{H}(\boldsymbol{r}, t) = \mathfrak{Re}[\mathbb{H}(\boldsymbol{r}) e^{j\omega t}], \tag{2.22b}$$

where we have used the standard phasor notation, splitting the time-harmonic fields into factors that deal separately with the variations in space and time.

$\mathbb{E}(\boldsymbol{r}) = \boldsymbol{E}_0 e^{-j\boldsymbol{k}\cdot\boldsymbol{r}}$ and $\mathbb{H}(\boldsymbol{r}) = \boldsymbol{H}_0 e^{-j\boldsymbol{k}\cdot\boldsymbol{r}}$ are the complex phasors describing the spatial part of the fields and e^{jwt} is the factor describing the wavelike nature of the field as in propagates in time where j is the imaginary unit. $\omega = 2\pi f$ is the wave's angular frequency, λ its wavelength, and $\boldsymbol{k} = k\hat{\boldsymbol{e}}_k$ is its wave vector, $\hat{\boldsymbol{e}}_k$ being the unit vector pointing in the direction of propagation and $k = \omega\sqrt{\mu\epsilon} = \frac{2\pi}{\lambda}$ the wave number. The real part of the phasor gives the initial condition of the field. The wave's angular frequency ω is material independent, i.e. it will be the same in both region 1 and 2. The wavelength λ and the wavenumber k are on the other hand material dependent and will hence vary between the two regions.

If solutions (2.22a) and (2.22b) are substituted into equation (2.17b), then the relation between the phasors turns out to be

$$\mathbb{H} = \frac{1}{\eta} \hat{\boldsymbol{e}}_k \times \mathbb{E}, \tag{2.23}$$

where $\eta = \sqrt{\frac{\mu}{\epsilon}}$ is the intrinsic impedance of the medium, see equation (2.2). (2.23) is of course the familiar perpendicular field property pertaining to plane electromagnetic waves in lossless materials.

This allows us to define the incoming (index i), reflected (index r) and refracted (index o) waves that all are solutions to Maxwell's equations as

$$\mathbb{E}_i = \boldsymbol{E}_{i0} e^{-j(\boldsymbol{k}_i \cdot \boldsymbol{r})}, \tag{2.24a}$$

$$\mathbb{H}_i = \frac{1}{\eta_i}\, \hat{\boldsymbol{e}}_{k_i} \times \boldsymbol{E}_{i0} e^{-j(\boldsymbol{k}_i \cdot \boldsymbol{r})}, \tag{2.24b}$$

$$\mathbb{E}_r = \boldsymbol{E}_{r0} e^{-j(\boldsymbol{k}_r \cdot \boldsymbol{r})}, \tag{2.24c}$$

$$\mathbb{H}_r = \frac{1}{\eta_i}\, \hat{\boldsymbol{e}}_{k_r} \times \boldsymbol{E}_{r0} e^{-j(\boldsymbol{k}_r \cdot \boldsymbol{r})}, \tag{2.24d}$$

$$\mathbb{E}_o = \boldsymbol{E}_{o0} e^{-j(\boldsymbol{k}_o \cdot \boldsymbol{r})}, \tag{2.24e}$$

$$\mathbb{H}_o = \frac{1}{\eta_o}\, \hat{\boldsymbol{e}}_{k_o} \times \boldsymbol{E}_{o0} e^{-j(\boldsymbol{k}_o \cdot \boldsymbol{r})}. \tag{2.24f}$$

We keep in mind that the actual fields are achieved by utilizing the phasor relations in equations (2.22a) and (2.22b).

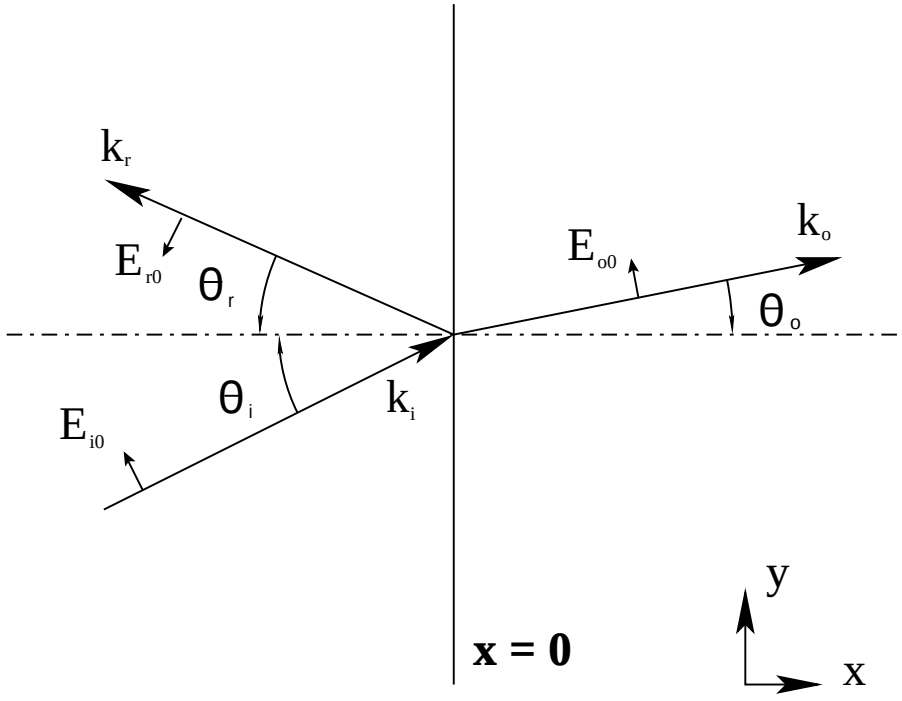

Figure 2.3. Electrical field vectors $\boldsymbol{E}_{i0}$, $\boldsymbol{E}_{r0}$ and $\boldsymbol{E}_{o0}$, as well as the wave vectors $\boldsymbol{k}_i$, $\boldsymbol{k}_r$ and $\boldsymbol{k}_o$ shown schematically.

With our geometry, where we look at the TE-mode in parallel polarization, the incoming, reflected and refracted amplitudes become $\boldsymbol{E}_{i0} = E_{i0}(-\sin\theta_i \hat{\boldsymbol{e}}_x + \cos\theta_i \hat{\boldsymbol{e}}_y)$, $\boldsymbol{E}_{r0} = E_{r0}(-\sin\theta_r \hat{\boldsymbol{e}}_x - \cos\theta_r \hat{\boldsymbol{e}}_y)$ and $\boldsymbol{E}_{o0} = E_{o0}(-\sin\theta_o \hat{\boldsymbol{e}}_x + \cos\theta_o \hat{\boldsymbol{e}}_y)$. To completely solve the problem we need to determine the reflected and refracted amplitudes. To do this, we need to dig into the gory details of the material interface at $x = 0$.

2.4.1 Interface Treatment

At $x = 0$ we have our material discontinuity. There are several boundary conditions, namely (2.5a) - (2.5d), that apply to this interface. Let us first examine boundary condition (2.5a). Putting in the complex representation of the $\boldsymbol{E}$-field using the electric field phasors in (2.24a), (2.24c) and (2.24e) we get

$$\hat{\boldsymbol{n}} \times \Big(\boldsymbol{E}_{i0} e^{-j(\boldsymbol{k}_i \cdot \boldsymbol{r} - \omega_i t)} + \boldsymbol{E}_{r0} e^{-j(\boldsymbol{k}_r \cdot \boldsymbol{r} - \omega_r t)} - \boldsymbol{E}_{o0} e^{-j(\boldsymbol{k}_o \cdot \boldsymbol{r} - \omega_o t)} \Big) \Big|_{x=0} = 0. \quad (2.25)$$

In order for this to hold at all points and all times on the interface $x = 0$, the phase factors of the different waves must be equal on $x = 0$, i.e.

$$e^{-j(\boldsymbol{k}_i \cdot \boldsymbol{r} - \omega_i t)} \Big|_{x=0} = e^{-j(\boldsymbol{k}_r \cdot \boldsymbol{r} - \omega_r t)} \Big|_{x=0} = e^{-j(\boldsymbol{k}_o \cdot \boldsymbol{r} - \omega_o t)} \Big|_{x=0}. \quad (2.26)$$

These equalities can only be satisfied for all y, z and t when

$$(\boldsymbol{k}_i \cdot \boldsymbol{r} - \omega_i t) \Big|_{x=0} = (\boldsymbol{k}_r \cdot \boldsymbol{r} - \omega_r t) \Big|_{x=0} = (\boldsymbol{k}_o \cdot \boldsymbol{r} - \omega_o t) \Big|_{x=0}. \quad (2.27)$$

At $\boldsymbol{r} = \boldsymbol{0}$ this is true for all t only if

$$\omega_i = \omega_r = \omega_o. \quad (2.28)$$

With the angular frequencies equal,

$$(\boldsymbol{k}_i \cdot \boldsymbol{r}) \Big|_{x=0} = (\boldsymbol{k}_r \cdot \boldsymbol{r}) \Big|_{x=0} = (\boldsymbol{k}_o \cdot \boldsymbol{r}) \Big|_{x=0} \quad (2.29)$$

remains.

Therefore, (2.28) indicates that the frequency of the wave will be independent of material. With the wave vectors $\boldsymbol{k}_i = k_i(\hat{\boldsymbol{e}}_x \cos\theta_i + \hat{\boldsymbol{e}}_y \sin\theta_i)$, $\boldsymbol{k}_r = k_r(\hat{\boldsymbol{e}}_x \cos\theta_r + \hat{\boldsymbol{e}}_y \sin\theta_r)$ and $\boldsymbol{k}_o = k_o(\hat{\boldsymbol{e}}_x \cos\theta_o + \hat{\boldsymbol{e}}_y \sin\theta_o)$ equation (2.29) simplifies to

$$y k_i \sin\theta_i = y k_r \sin\theta_r = y k_o \sin\theta_o. \quad (2.30)$$

This holds for all y if

$$k_i \sin\theta_i = k_r \sin\theta_r = k_o \sin\theta_o. \quad (2.31)$$

Since the angular frequency as well as the permittivity and permeability are constant in material 1, and the relation between angular frequency ω and wave number k is $k = \omega\sqrt{\epsilon\mu}$, the consequence must be that $k_i = k_r$ and hence that the incident angle is equal to the reflected, i.e.

$$\theta_i = \theta_r. \quad (2.32)$$

Equation (2.31) indicates that the incident and refracted angles are related by

$$k_i \sin\theta_i = k_o \sin\theta_o, \quad (2.33)$$

which is Snell's famous law of refraction. With these relations, we can express all the angles in the problem in terms of the angle of incidence.

What remains now is to somehow relate the scalar amplitudes E_{r0} and E_{o0} to the incoming amplitude E_{i0}. For this we use the boundary conditions at the interface $x = 0$. Equations (2.5a) and (2.5b), where we apply the properties of dielectrica to set $\boldsymbol{J}_S = \mathbf{0}$, together with the equality of the phase factors at the interface, yield the reflection and refraction coefficients, $\Gamma_{\shortparallel}$ and $\tau_{\shortparallel}$ for parallel polarization

$$\Gamma_{\shortparallel} = \frac{E_{r0}}{E_{i0}} = \frac{\eta_1 \cos\theta_i - \eta_2 \cos\theta_o}{\eta_1 \cos\theta_i + \eta_2 \cos\theta_o}, \tag{2.34a}$$

$$\tau_{\shortparallel} = \frac{E_{o0}}{E_{i0}} = \frac{2\eta_2 \cos\theta_i}{\eta_1 \cos\theta_i + \eta_2 \cos\theta_o}. \tag{2.34b}$$

Here, η_1 and η_2 are the intrinsic impedances in material 1 and 2 respectively, see equation (2.2).

Putting all of this together, we reach the analytical solution

$$\begin{aligned}
\boldsymbol{E}_i(x,y,t) &= E_{i0}(-\sin\theta_i \hat{\boldsymbol{e}}_x + \cos\theta_i \hat{\boldsymbol{e}}_y) \cdot \\
&\quad \cdot \cos(\omega t - k_1(x\cos\theta_i + y\sin\theta_i)), && \text{(2.35a)} \\
\boldsymbol{H}_i(x,y,t) &= \frac{E_{i0}\hat{\boldsymbol{e}}_z}{\eta_1}\cos(\omega t - k_1(x\cos\theta_i + y\sin\theta_i)), && \text{(2.35b)} \\
\boldsymbol{E}_r(x,y,t) &= \Gamma_{\shortparallel} E_{i0}(-\sin\theta_i \hat{\boldsymbol{e}}_x - \cos\theta_i \hat{\boldsymbol{e}}_y) \cdot \\
&\quad \cdot \cos(\omega t - k_1(-x\cos\theta_i + y\sin\theta_i)), && \text{(2.35c)} \\
\boldsymbol{H}_r(x,y,t) &= \frac{\Gamma_{\shortparallel} E_{i0}\hat{\boldsymbol{e}}_z}{\eta_1}\cos(\omega t - k_1(-x\cos\theta_i + y\sin\theta_i)), && \text{(2.35d)} \\
\boldsymbol{E}_o(x,y,t) &= \tau_{\shortparallel} E_{i0}(-\sin\theta_o \hat{\boldsymbol{e}}_x + \cos\theta_o \hat{\boldsymbol{e}}_y) \cdot \\
&\quad \cdot \cos(\omega t - k_2(x\cos\theta_o + y\sin\theta_o)), && \text{(2.35e)} \\
\boldsymbol{H}_o(x,y,t) &= \frac{\tau_{\shortparallel} E_{i0}\hat{\boldsymbol{e}}_z}{\eta_2}\cos(\omega t - k_2(x\cos\theta_o + y\sin\theta_o)), && \text{(2.35f)}
\end{aligned}$$

with $k_1 = \omega\sqrt{\mu_1\epsilon_1}$, $k_2 = \omega\sqrt{\mu_2\epsilon_2}$ and $\theta_o = \arcsin(\frac{k_i}{k_o}\sin\theta_i)$.

As mentioned in Section 2.3 about the problem specifics, the material parameters in our case are $\epsilon_1 = 1$, $\mu_1 = 1$, $\epsilon_2 = 4$, and $\mu_2 = 1$. In our computations we will use the incoming angles $\theta_i = \frac{\pi}{3}$, $\theta_i = \frac{\pi}{6}$ and $\theta_i = \theta_B$, where θ_B is the Brewster angle that yields a reflection coefficient $\Gamma_{\shortparallel} = 0$. We will also normalize the amplitude of the incoming wave to $E_{i0} = 1$.

In the left domain, i.e. in material 1, we have two waves, the incident and the reflected. To obtain the total field in this region, we just need to add the incident and reflected fields by means of superposition.

In equations (2.35a) - (2.35f) we have an exact solution that will serve as a guideline for the numerical schemes to strive for.

3 Numerical Methods

To solve problems in electromagnetism, we need a framework that deals with the Maxwell equations in a general fashion. One has to be able to model different settings, such as geometries and materials, and this is impossible to do analytically for all possible cases. Therefore, the focus turns to general numerical methods. The purpose of this report is to evaluate how well a high-order numerical spectral method performs in electromagnetic calculations in comparison to a high-order finite difference method. The simple test case described in the previous section will provide a setting where we will be able to compare the numerical results to the true analytical solution, i.e. expressions (2.35a) - (2.35f), yielding a measure of the error of the methods.

3.1 High-Order Spectral Method

Our objective in this section is to briefly introduce a high-order spectral method on unstructured grids for time-domain electromagnetics. A more complete description of the method can be found in [3]. Solving differential equations, an agile handling of complex geometries comes almost invariably from the use of unstructured grids. This spectral method does indeed rely on and use the powers of such an unstructured mesh.

The computational domain, upon which the spectral framework is to be active, is divided into non-overlapping elements called simplices. In the case of a two-dimensional domain, these simplices are triangles. With a three-dimensional geometry in mind, tetrahedrons fill out the domain.

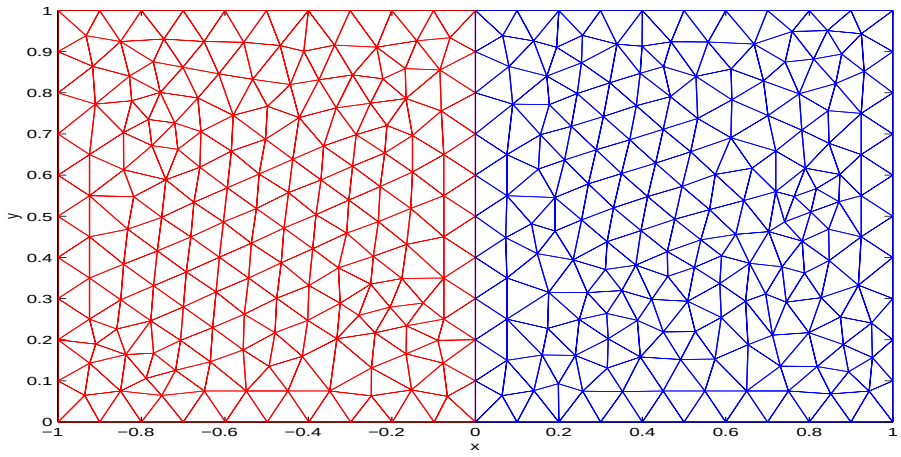

Figure 3.1. Unstructured grid for spectral element method with grid spacing $\Delta x = 0.1$ at the boundaries. At $x = 0$, the material transition occurs.

Rather than seeking a globally continuous solution of the Maxwell equations, continuous solutions are sought on the separate simplices, allowing for discontinuities over the element borders. The equations are still satisfied, but in the weaker Galerkin sense.

On each simplex, a set of interpolation nodes is defined. For the exact placement of the nodes, we refer to [8]. The purpose of the nodes is to serve as interpolation points for an elementwise continuous solution. The more nodes we use, the higher

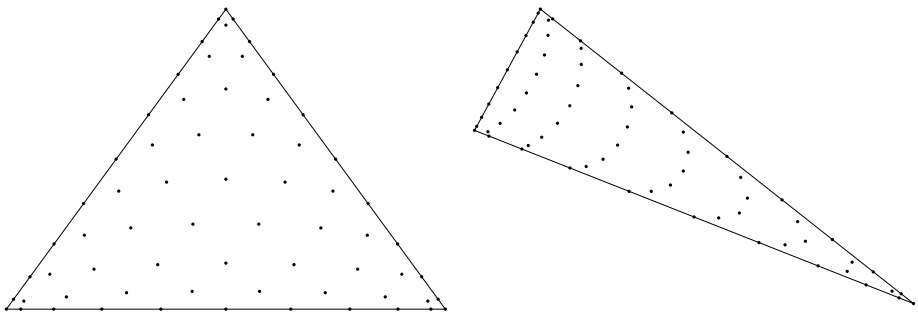

Figure 3.2. Examples of nodal sets in triangles when the interpolation is carried out to the 10^{th} order.

order interpolation polynomials we can utilize to get a better numerical approximation of the solution. The number of nodes per simplex is directly related to the order of the interpolation polynomial by

$$N_n^d = \frac{1}{d!}\prod_{i=1}^{d}(n+i), \tag{3.1}$$

where d is the geometrical dimension of the computational domain, n the maximum order of the interpolation polynomial and N_n^d is the corresponding number of nodes in the simplex.

3.1.1 Computational Scheme

Let us first treat the computational scheme in a general three-dimensional fashion. The connection to our specific, two-dimensional problem can then be reached by introducing a set of suitable simplifications.

3.1.1.1 General Description

Our problem gives rise to the reduced Maxwell curl-equations (2.17a) and (2.17b), i.e.

$$\epsilon\frac{\partial \boldsymbol{E}(\boldsymbol{r},t)}{\partial t} = \boldsymbol{\nabla}\times\boldsymbol{H}(\boldsymbol{r},t), \tag{3.2a}$$

$$\mu\frac{\partial \boldsymbol{H}(\boldsymbol{r},t)}{\partial t} = -\boldsymbol{\nabla}\times\boldsymbol{E}(\boldsymbol{r},t), \tag{3.2b}$$

for $\boldsymbol{E}$ and $\boldsymbol{H}$. Let us reformulate these equations into

$$Q(\boldsymbol{r})\frac{\partial \boldsymbol{q}(\boldsymbol{r},t)}{\partial t} + \nabla\cdot\boldsymbol{F}(\boldsymbol{q}(\boldsymbol{r},t)) = 0 \tag{3.3}$$

in order to save some space and labor. We have hereby introduced the state vector

$$\boldsymbol{q}(\boldsymbol{r},t) = \begin{bmatrix} \boldsymbol{E}(\boldsymbol{r},t) \\ \boldsymbol{H}(\boldsymbol{r},t) \end{bmatrix}, \tag{3.4}$$

and the flux

$$\boldsymbol{F}_i(\boldsymbol{q}(\boldsymbol{r},t)) = \begin{bmatrix} -\hat{\boldsymbol{e}}_i\times\boldsymbol{H}(\boldsymbol{r},t) \\ \hat{\boldsymbol{e}}_i\times\boldsymbol{E}(\boldsymbol{r},t) \end{bmatrix}. \tag{3.5}$$

$\hat{\boldsymbol{e}}_i$ are of course the three Cartesian unit vectors for $i = x, y, z$. In the full three-dimensional case, $\boldsymbol{q}$ and $\boldsymbol{F}(\boldsymbol{q})$ are vectors with 6 components. In this case, the coefficient matrix $Q(\boldsymbol{r})$ becomes $Q(\boldsymbol{r}) = diag\Big(\epsilon(\boldsymbol{r}), \epsilon(\boldsymbol{r}), \epsilon(\boldsymbol{r}), \mu(\boldsymbol{r}), \mu(\boldsymbol{r}), \mu(\boldsymbol{r})\Big)$.

Now, the purpose of this entire business is to seek the field solutions $\boldsymbol{q}(\boldsymbol{r}, t)$. As hinted above, the spectral method approaches this solution by means of interpolation. We assume that the exact solution $\boldsymbol{q}(\boldsymbol{r}, t)$ can be well mimicked by the numerical approximation $\boldsymbol{q}_N(\boldsymbol{r}, t)$ locally on a simplex D in such a way that

$$\boldsymbol{q}(\boldsymbol{r}, t) \approx \boldsymbol{q}_N(\boldsymbol{r}, t) = \sum_{i=1}^{N} \boldsymbol{q}_N(\boldsymbol{r}_i, t) L_i(\boldsymbol{r}), \quad \boldsymbol{r} \in D, \tag{3.6}$$

where $L_i(\boldsymbol{r})$ are the Lagrangian interpolation polynomials on the particular simplex of interest. The Lagrangian polynomials span the space in which the numerical approximation resides. The numerical approximation $\boldsymbol{q}_N(\boldsymbol{r}, t)\big|_D$ will be a continuous function inside D, but when many simplices are connected, the global numerical solution will show discontinuities over the faces of the simplices.

On a single particular simplex D, there are N interpolation nodes, numbered by the index i. Each node gives rise to 6 unknown field variables, so that the simplex will house $6N$ degrees of freedom. In the same way as $\boldsymbol{q}$ could be approximated by the Lagrangian interpolation polynomials, so can the flux $\boldsymbol{F}(\boldsymbol{q})$ and every other physical quantity. This leads us to choose a scheme that satisfies equation (3.3) in the following, weak way $\forall i \in \{1, 2, \ldots, N\}$:

$$\int_D \Big(Q\frac{\partial \boldsymbol{q}_N}{\partial t} + \nabla \cdot \boldsymbol{F}_N\Big) L_i d\boldsymbol{r} = \oint_{\partial D} \tau L_i \hat{\boldsymbol{n}} \cdot [\boldsymbol{F}_N^-] dS(\boldsymbol{r}). \tag{3.7}$$

In (3.7) we have introduced a penalty term on the right hand side of the equation. This term deals with the discontinuities that arise from the discrete element organization and compensates for the flux exiting the simplex D due to these discontinuities. Compare this to the discontinuous Galerkin method [9].

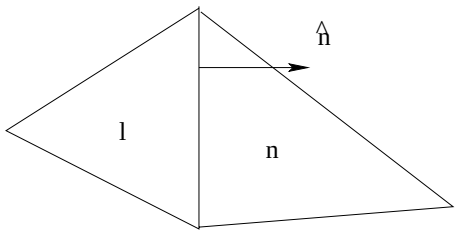

Figure 3.3. Two neighboring elements at the interface.

Let us take a closer look at the penalty term. First, τ is a scalar parameter that determines the strength of the penalty term. The larger τ is, the stronger the penalty term is enforced. The value of this parameter will be discussed later. $\hat{\boldsymbol{n}}$ is the normal vector to the element border, pointing away from the simplex. $[\boldsymbol{F}_N^-]$ is the difference in upwind flux at the interface between the present simplex D and its neighbor cell. The flux $\boldsymbol{F}_N$ described earlier can be decomposed into upwind and downwind fluxes, $\boldsymbol{F}_N^-$ and $\boldsymbol{F}_N^+$, by $\boldsymbol{F}_N = \boldsymbol{F}_N^- + \boldsymbol{F}_N^+$. These fluxes are related to the characteristics of Maxwell's equations. The upwind flux $\boldsymbol{F}_N^-$ is the part of the flux that can be written using only the incoming characteristic variables and

is basically the flux entering the local simplex from the neighbor cell. The flux splitting will be discussed in detail in appendix C.

If we let the left simplex in Figure 3.3 be designated l for local and the right simplex n for neighbor, then the explicit form of the jump in the normal component of the upwind flux over the cell boundary used in the penalty term becomes, (see appendix C)

$$\hat{\boldsymbol{n}} \cdot [\boldsymbol{F}_N^-] = \begin{bmatrix} \bar{Z}^{-1}\hat{\boldsymbol{n}} \times \Big(Z^n[\boldsymbol{H}_N] - \hat{\boldsymbol{n}} \times [\boldsymbol{E}_N] \Big) \\ \bar{Y}^{-1}\hat{\boldsymbol{n}} \times \Big(-Y^n[\boldsymbol{E}_N] - \hat{\boldsymbol{n}} \times [\boldsymbol{H}_N] \Big) \end{bmatrix}. \tag{3.8}$$

where the bracketed fields denote the jump in the numerical field values over the element border, i.e.

$$[\boldsymbol{E}_N] = \boldsymbol{E}_N^n - \boldsymbol{E}_N^l, \tag{3.9a}$$

$$[\boldsymbol{H}_N] = \boldsymbol{H}_N^n - \boldsymbol{H}_N^l, \tag{3.9b}$$

with the superscript 'n' referring to fields calculated in the neighboring simplex while 'l' denotes the field values of the present element, see Figure 3.4.

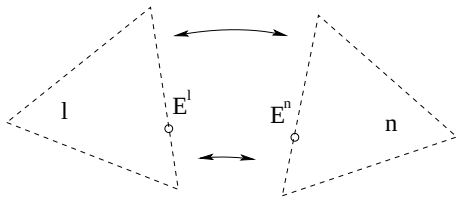

Figure 3.4. Two neighboring elements split apart graphically to show the notion of the 'l' and 'n' superscripts. The values $\boldsymbol{E}^l$ and $\boldsymbol{E}^n$ are calculated for the same geometrical point $\boldsymbol{r}$, but $\boldsymbol{E}^l$ is computed in element 'l' whereas $\boldsymbol{E}^n$ is computed in element 'n'.

Z is the material impedance and Y the material conductance

$$Z^{l,n} = \eta^{l,n} = \frac{1}{Y^{l,n}} = \sqrt{\frac{\mu^{l,n}}{\epsilon^{l,n}}}, \tag{3.10}$$

and $\bar{Z}$ and $\bar{Y}$ are the sums of them over the interface

$$\bar{Z} = Z^l + Z^n, \tag{3.11a}$$

$$\bar{Y} = Y^l + Y^n. \tag{3.11b}$$

Returning to the main issue, we have discretized the simplex into N interpolation nodes. We need to find the values $\boldsymbol{q}_N(\boldsymbol{r}_i, t)$ for all indices i in order to be able to interpolate to a continuous solution. Making use of our interpolating assumption, $\boldsymbol{f}_N(\boldsymbol{r}, t) = \sum_{i=1}^N \boldsymbol{f}_N(\boldsymbol{r}_i, t) L_i(\boldsymbol{r})$, where $\boldsymbol{f}_N(\boldsymbol{r}, t)$ is arbitrary, we can write out the semi-discrete form of equation (3.7)

$$\sum_{j=1}^{N} (M_{ij} \frac{\partial \boldsymbol{q}_N^j}{\partial t} + \boldsymbol{S}_{ij} \cdot \boldsymbol{F}_N^j) = \sum_{l=1}^{N_{\partial D}} \Omega_{il} \hat{\boldsymbol{n}} \cdot [\boldsymbol{F}_N^-]^l, \tag{3.12a}$$

$$\forall i \in \{1, 2, \ldots, N\}$$

where $\boldsymbol{q}_N^j = \boldsymbol{q}_N(\boldsymbol{r}_j, t)$, $\boldsymbol{F}_N^j = \boldsymbol{F}_N\big(\boldsymbol{q}_N(\boldsymbol{r}_j, t)\big)$ and $[\boldsymbol{F}_N^-]^l = \big[\boldsymbol{F}_N^-\big(\boldsymbol{q}_N(\boldsymbol{r}_l, t)\big)\big]$ and l runs over all the interpolation nodes on the boundary, ∂D, while i and j

run over all the nodes in the entire simplex D. Here we have introduced the mass matrix M_{ij}, the stiffness matrix $\boldsymbol{S}_{ij}$ and the face-based mass matrix Ω_{il} as

$$M_{ij} = \big(L_i(\boldsymbol{r}), Q(\boldsymbol{r})L_j(\boldsymbol{r})\big)_D \tag{3.13a}$$

$$\boldsymbol{S}_{ij} = \big(L_i(\boldsymbol{r}), \boldsymbol{\nabla} L_j(\boldsymbol{r})\big)_D \tag{3.13b}$$

$$\Omega_{il} = \big(L_i(\boldsymbol{r}), \tau(\boldsymbol{r})L_l(\boldsymbol{r})\big)_{\partial D} \tag{3.13c}$$

where we have used the inner product representations

$$\big(f(\boldsymbol{r}), g(\boldsymbol{r})\big)_D = \int_D f(\boldsymbol{r})g(\boldsymbol{r})d\boldsymbol{r}, \tag{3.14a}$$

$$\big(f(\boldsymbol{r}), g(\boldsymbol{r})\big)_{\partial D} = \int_{\partial D} f(\boldsymbol{r})g(\boldsymbol{r})dS(\boldsymbol{r}). \tag{3.14b}$$

Relation (3.12a) is a system of N equations, each separate equation being a vector equation with six components in three dimensions. This system can be written in matrix notation as

$$M\frac{\partial \boldsymbol{q}_N}{\partial t} + \boldsymbol{S}\cdot\boldsymbol{F}_N = \Omega\hat{\boldsymbol{n}}\cdot[\boldsymbol{F}_N^-]. \tag{3.15}$$

With this in place, a system of ordinary differential equations with respect to time emerges,

$$\frac{\partial \boldsymbol{q}_N}{\partial t} = -M^{-1}\boldsymbol{S}\cdot\boldsymbol{F}_N + M^{-1}\Omega\hat{\boldsymbol{n}}\cdot[\boldsymbol{F}_N^-], \tag{3.16}$$

and a well-known method such as the Runge-Kutta scheme can be used for the time integration. We only need to initialize the mass and stiffness matrices, which can be done once and for all. To solve the problem in the entire computational domain consisting of many simplices, one such system of equations has to be solved for each element. Apart from the penalty terms were field values from two elements are needed, the simplices decouple fully, and this makes parallel computations easily implemented and favorable.

To completely describe the scheme, we need to specify the interpolation polynomials, $L_i(\boldsymbol{r})$. We recall that they were defined as

$$\boldsymbol{q}(\boldsymbol{r},t) \approx \boldsymbol{q}_N(\boldsymbol{r},t) = \sum_{i=1}^{N} \boldsymbol{q}_N(\boldsymbol{r}_i,t)L_i(\boldsymbol{r}). \tag{3.17}$$

It is convenient to first expand $\boldsymbol{q}_N(\boldsymbol{r},t)$ in an orthonormal basis $\psi_i(\boldsymbol{r})$. This basis spans the polynomial space

$$\mathrm{P}_n = \mathrm{span}\{x^a y^b z^c \mid a,b,c \geq 0;\ a+b+c \leq n\} = \mathrm{span}\{\psi_i(\boldsymbol{r})\}_i^N, \tag{3.18}$$

where n is the maximum polynomial order and $N = \dim(\mathrm{P}_n)$ is the number of nodes per simplex given by (3.1). A proper orthonormal basis $\{\psi_i\}_{i=1}^N$ can be found in [5], [6]. For a standard tetrahedron I,

$$\mathrm{I} = \{(\xi,\eta,\zeta) \in \mathbb{R}^3 \mid \xi,\eta,\zeta \geq -1;\ \xi+\eta+\zeta \leq 1\}, \tag{3.19}$$

this takes the form of

$$\psi_i(\boldsymbol{\xi}) = \frac{\tilde{\psi}_i(\boldsymbol{\xi})}{\sqrt{\gamma_i}}, \tag{3.20}$$

where

$$\begin{aligned}\tilde{\psi}_i(\boldsymbol{\xi}) = \tilde{\psi}_{\alpha_1\alpha_2\alpha_3}(\boldsymbol{\xi}) = \quad & P_{\alpha_1}^{(0,0)}(r)(\frac{1-s}{2})^{\alpha_1} \cdot \\ & \cdot P_{\alpha_2}^{(2\alpha_1+1,0)}(s)(\frac{1-t}{2})^{\alpha_1+\alpha_2}. \\ & \cdot P_{\alpha_3}^{(2\alpha_1+2\alpha_2+1,0)}(t)\end{aligned} \tag{3.21}$$

and the normalization factor

$$\gamma_i = \gamma_{\alpha_1\alpha_2\alpha_3} = \frac{2}{2\alpha_1+1} \cdot \frac{2^{2\alpha_1+2}}{2(\alpha_1+\alpha_2)+2} \cdot \frac{2^{2(\alpha_1+\alpha_2)+3}}{2(\alpha_1+\alpha_2+\alpha_3)+3}. \tag{3.22}$$

Here, $P_n^{(\alpha,\beta)}(x)$ represents the classical Jacobi polynomial of order n, and we have introduced the substitutions

$$r = -\frac{2(1+\xi)}{\eta+\zeta} - 1, \tag{3.23a}$$

$$s = -\frac{2(1+\eta)}{1-\zeta} - 1, \tag{3.23b}$$

$$t = \zeta. \tag{3.23c}$$

The index i on ψ_i reflects some chosen ordering of α_1, α_2, and α_3 so that $i \in \{1, 2, ..., N\}$ and

$$\mathrm{P}_n = \mathrm{span}\{\psi_{\alpha_1\alpha_2\alpha_3} \mid \alpha_1, \alpha_2, \alpha_3 \geq 0;\ \alpha_1+\alpha_2+\alpha_3 \leq n\}. \tag{3.24}$$

This basis can then be transformed from the coordinate system $\boldsymbol{\xi} = (\xi, \eta, \zeta)$ in the standard tetrahedron I to the appropriate basis in the coordinates $\boldsymbol{r} = (x, y, z)$ in tetrahedron D by the transformation $\boldsymbol{\xi} = \Psi(\boldsymbol{r})$.

The basis $\psi_i(\boldsymbol{r})$ allows us to write

$$\boldsymbol{q}_N(\boldsymbol{r}, t) = \sum_{j=1}^{N} \hat{\boldsymbol{q}}_j(t)\psi_j(\boldsymbol{r}). \tag{3.25}$$

Evaluating this at the location $\boldsymbol{r}_i$, inserting it into equation (3.17) and comparing it to equation (3.25) using orthogonality yields

$$\psi_j(\boldsymbol{r}) = \sum_{i=1}^{N} \psi_j(\boldsymbol{r}_i)L_i(\boldsymbol{r}) \quad \forall j, \tag{3.26}$$

or in matrix notation

$$\boldsymbol{\psi} = V^T\boldsymbol{L}, \tag{3.27}$$

where $\psi_i = \psi_i(\boldsymbol{r})$, $V_{ij}^T = \psi_i(\boldsymbol{r}_j)$ and $L_j = L_j(\boldsymbol{r})$.

By utilizing this defined basis $\psi_i(\boldsymbol{r})$, we can now solve for the interpolation polynomials,

$$\boldsymbol{L} = (V^T)^{-1}\boldsymbol{\psi}, \tag{3.28}$$

and with these computed, we can precalculate the matrices M, $\boldsymbol{S}$ and Ω for the scheme in equation (3.16).

Now, Ω is somewhat different from the others since it is a semi-face-based matrix with N rows and $N_{\partial D}$ columns, while M and $\boldsymbol{S}$ both are $N \times N$-matrices. The elements $\Omega_{il} = (L_i(\boldsymbol{r}), L_l(\boldsymbol{r}))_{\partial D}$ contain the Lagrangian interpolation polynomials on the face, $L_l(\boldsymbol{r})$. In the case of a two-dimensional face, these follow the exact same conditions as above, with the exception that the basis functions are given by

$$\tilde{\psi}_l(\xi, \eta) = \tilde{\psi}_{\alpha_1 \alpha_2 0}(\xi, \eta, -1). \tag{3.29}$$

If the face were one-dimensional, then this would in the same fashion lead to the face-based basis functions

$$\tilde{\psi}_l(\xi) = \tilde{\psi}_{\alpha_1 00}(\xi, -1, -1). \tag{3.30}$$

With these matrices initialized, we are all set to get the scheme in equation (3.16) rolling. We use the 4^{th} order, 5 stage low-storage Runge-Kutta scheme to solve the differential equation for the unknowns $\boldsymbol{q}_N$. The unknowns are in fact the electric and magnetic fields at the discrete interpolation nodes $\boldsymbol{r}_j$,

$$\boldsymbol{q}_N^j = \boldsymbol{q}_N(\boldsymbol{r}_j, t) = \begin{bmatrix} \boldsymbol{E}(\boldsymbol{r}_j, t) \\ \boldsymbol{H}(\boldsymbol{r}_j, t) \end{bmatrix}. \tag{3.31}$$

If we have the desire to construct a continuous solution for $\boldsymbol{E}(\boldsymbol{r}, t)$ or $\boldsymbol{H}(\boldsymbol{r}, t)$, then we just have to utilize the prescribed Lagrangian interpolation approximation

$$\boldsymbol{q}(\boldsymbol{r}, t) \approx \boldsymbol{q}_N(\boldsymbol{r}, t) = \sum_{i=1}^{N} \boldsymbol{q}_N(\boldsymbol{r}_i, t) L_i(\boldsymbol{r}) \tag{3.32}$$

with our calculated point values $\boldsymbol{q}_N(\boldsymbol{r}_i, t)$.

3.1.1.2 Problem Specific Scheme

Since we are dealing with a simple two-dimensional model-problem, we can easily introduce a number of simplifications to the general scheme above. First of all, instead of the full three-dimensional problem in equations (3.2a) and (3.2b), we can look at the reduced transverse electric mode equations (2.18a), (2.18b) and (2.18c). This brings down the size of all vectors and matrices from 6 to 3. The interpolation polynomials in each simplex will be two-dimensional, whereas the face polynomials will have only one spatial dimension. The total number of interpolation nodes residing in each triangular element will be $N = \frac{1}{2}(n+1)(n+2)$, and $N_{\partial D} = (n+1)$ nodes will be spread out on each face of the triangle. In addition, by using merely straight-sided triangles, the transformations from the standard triangle become simple as the coordinate transformation Jacobian turns constant. A case with these simplifications has been implemented in a MATLAB-code, and the results will be discussed in chapter 4.

3.2 High Order Finite Difference Method

The name of the game for finite difference methods is to approximate spatial derivatives by finite differences. Performing a finite difference calculation, one needs to discretize the computational domain into nodes. The values of the solution at the different nodal points will be used in order to calculate the differences that approximate the actual derivatives in the differential equation at hand. In order to do this effectively, it is convenient to use structured grids that make it easy to build the differences in a general fashion for all points in the domain.

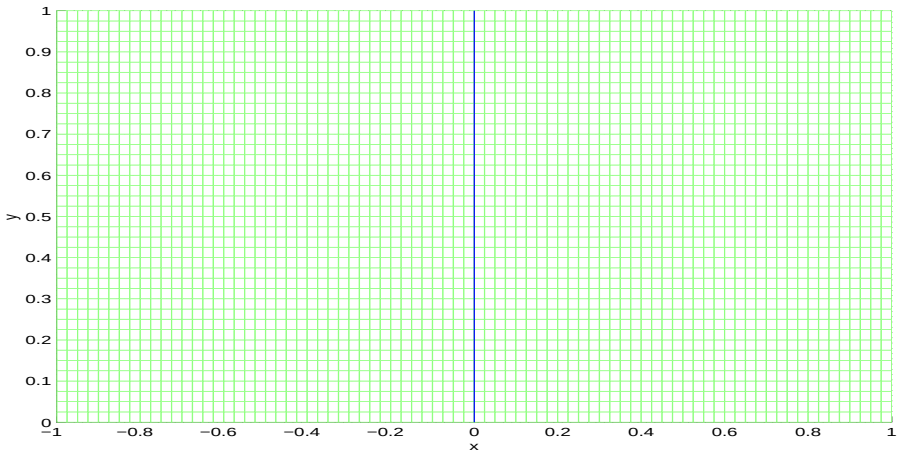

Figure 3.5. Structured grid with spacing $\Delta x = \Delta y = 0.025$.

A finite difference method is fairly straightforward to implement into a computer code, at least for a simple geometry. However, for complex bodies and different materials, sophisticated mapping procedures are required. The metric coefficients of these mappings might introduce instabilities, see [10].

For a structured, Cartesian, equidistant grid such as the one given above, the straightforward way to approximate a spatial derivative of second order of accuracy is

$$\frac{\partial E(x_i, y_j)}{\partial x} \approx \frac{1}{2\Delta x}\Big(E(x_{i+1}, y_j) - E(x_{i-1}, y_j)\Big). \tag{3.33}$$

This estimate will be used in our finite difference code, but in an attempt to increase accuracy, we will also go to higher-order methods. We will concentrate on orders 4 and 6 in this work. The fourth-order centered differentiation approximation will be

$$\begin{aligned}\frac{\partial E(x_i, y_j)}{\partial x} \approx \frac{1}{\Delta x}\Big(&\frac{-1}{12}E(x_{i+2}, y_j) + \frac{2}{3}E(x_{i+1}, y_j) \\ &- \frac{2}{3}E(x_{i-1}, y_j) + \frac{1}{12}E(x_{i-2}, y_j)\Big),\end{aligned} \tag{3.34}$$

and we will use

$$\begin{aligned}\frac{\partial E(x_i, y_j)}{\partial x} \approx \frac{1}{\Delta x}\Big(&\frac{1}{60}E(x_{i+3}, y_j) - \frac{3}{20}E(x_{i+2}, y_j) \\ &+ \frac{3}{4}E(x_{i+1}, y_j) - \frac{3}{4}E(x_{i-1}, y_j) \\ &+ \frac{3}{20}E(x_{i-2}, y_j) - \frac{1}{60}E(x_{i-3}, y_j)\Big)\end{aligned} \tag{3.35}$$

as our centered sixth-order approximation.

3.2.1 Computational Scheme

For a detailed discussion of the computational scheme of the finite difference method, we refer to [4]. Here, we just briefly summarize the topic.

We start by looking at the equations that we want to solve for our particular problem set-up. Maxwell's equations in the transverse electric mode are given in equations (2.18a), (2.18b) and (2.18c). Writing these in matrix form yields

$$S\tilde{\boldsymbol{u}}_t + A\tilde{\boldsymbol{u}}_x + B\tilde{\boldsymbol{u}}_y = 0, \tag{3.36}$$

with

$$S = \begin{bmatrix} \mu & 0 & 0 \\ 0 & \epsilon & 0 \\ 0 & 0 & \epsilon \end{bmatrix}, \quad \tilde{\boldsymbol{u}}(\boldsymbol{r}) = \begin{bmatrix} H_z(\boldsymbol{r}) \\ E_x(\boldsymbol{r}) \\ E_y(\boldsymbol{r}) \end{bmatrix}, \quad A = \begin{bmatrix} 0 & 0 & 1 \\ 0 & 0 & 0 \\ 1 & 0 & 0 \end{bmatrix}, \tag{3.37}$$

and

$$B = \begin{bmatrix} 0 & -1 & 0 \\ -1 & 0 & 0 \\ 0 & 0 & 0 \end{bmatrix}. \tag{3.38}$$

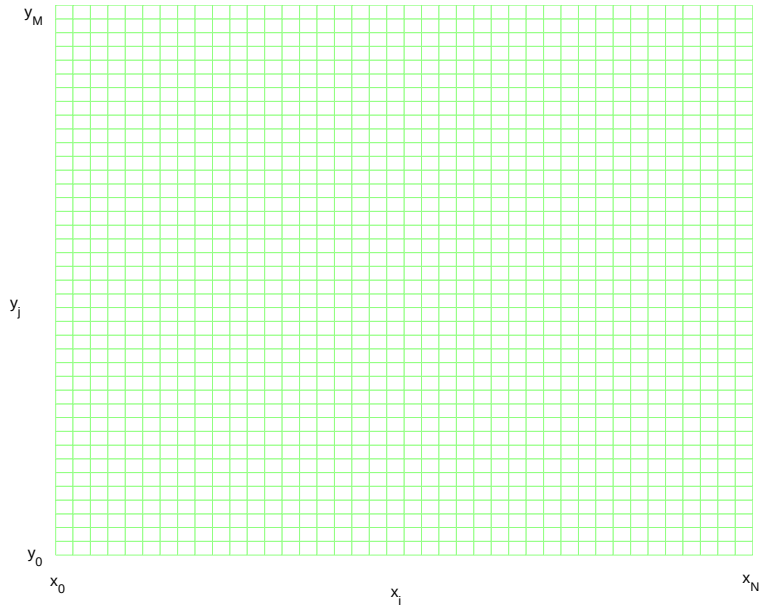

Figure 3.6. Discretization of a computational region for the finite difference scheme.

We first discretize the computational, two-dimensional region into node points (x_i, y_j), $i \in 0, 1, \ldots, N$, $j \in 0, 1, \ldots, M$ as shown in Figure 3.6. We construct a vector $\boldsymbol{u}$ where the entries themselves are vectors $\boldsymbol{u}_i(t)$ with the vector values at the nodes being $\tilde{\boldsymbol{u}}_{i,j}(t)$,

$$\boldsymbol{u} = \begin{bmatrix} \boldsymbol{u}_0(t) \\ \boldsymbol{u}_1(t) \\ \vdots \\ \boldsymbol{u}_N(t) \end{bmatrix}, \quad \boldsymbol{u}_i(t) = \begin{bmatrix} \tilde{\boldsymbol{u}}_{i,0}(t) \\ \tilde{\boldsymbol{u}}_{i,1}(t) \\ \vdots \\ \tilde{\boldsymbol{u}}_{i,M}(t) \end{bmatrix}, \quad \tilde{\boldsymbol{u}}_{i,j}(t) = \begin{bmatrix} H_z(x_i, y_j) \\ E_x(x_i, y_j) \\ E_y(x_i, y_j) \end{bmatrix}. \tag{3.39}$$

The vector $\boldsymbol{u}_i(t)$ stores all the field values from a column of grid points, i.e. it only looks at nodes placed on a specific x-value. In a similar fashion, we can define a vector

$$\boldsymbol{v}_j(t) = \begin{bmatrix} \tilde{\boldsymbol{u}}_{0,j}(t) \\ \tilde{\boldsymbol{u}}_{1,j}(t) \\ \vdots \\ \tilde{\boldsymbol{u}}_{N,j}(t) \end{bmatrix} \tag{3.40}$$

that only handles the field values from a row of grid points, i.e. the nodes situated at a single y-coordinate.

Using the finite difference approximations of the derivatives according to expressions (3.33), (3.34) and (3.35) above, we can construct a differential operator D_x that acts on the vector $\boldsymbol{u}_j(t)$, and in the same way an operator D_y that differentiates with respect to y and that acts on the vector $\boldsymbol{v}_j(t)$ described above. These operators are constructed as Summation By Parts operators, which means that $D = P^{-1}Q$, where the matrix P is symmetric, positive definite and bounded, i.e. $\Delta x p I \leq P \leq \Delta x q I$ where $p > 0$ and q are bounded independent of the size of the grid, i.e. independent of N and M. The matrix Q is to be almost skew-symmetric, i.e. $Q^T + Q = diag(-1, 0, 0, ..., 0, 0, 1)$.

With these operators in place, we would like to be able to write the system of differential equations in (3.36) acting on $\boldsymbol{u}$ in its entirety. This is accomplished through Kronecker multiplication by large identity matrices, and the result becomes

$$(I_{MN} \otimes S)\boldsymbol{u}_t + (D_x \otimes I_M \otimes A)\boldsymbol{u} + (I_N \otimes D_y \otimes B)\boldsymbol{u} = 0, \tag{3.41}$$

where we have introduced the identity matrices I_M, I_N and I_{MN} with sizes $(M+1)\times(M+1)$, $(N+1)\times(N+1)$ and $(M+1)(N+1)\times(M+1)(N+1)$ respectively, as well as the Kronecker product of matrices, $\otimes$, see appendix A. Through this composition, the differential operator D_x only acts on the x-components of $\boldsymbol{u}$ while D_y operates merely on $\boldsymbol{u}$'s y-components.

A way of imposing the boundary conditions is through the so-called Simultaneous Approximation Term (SAT) procedure, [7]. This is a penalty procedure entirely similar to the one used in the spectral method in Section 3.1. In the same fashion as we did there, we would like to base the boundary treatment on the notion of characteristic variables and upwind fluxes, see appendices B and C. We set the ingoing characteristic variables as the boundary data, and we will compare the actual solution at the boundaries to these given data. If the numerical solution differs from the boundary data, the scheme will be penalized. The SAT procedure affects the numerical scheme by replacing the zero on the right hand side of equation (3.41) by a term from each boundary, yielding

$$(I_{MN} \otimes S)\boldsymbol{u}_t + (D_x \otimes I_M \otimes A)\boldsymbol{u} + (I_N \otimes D_y \otimes B)\boldsymbol{u} = \sum_b BC_b. \tag{3.42}$$

For a rectangular geometry such as ours, we will have 4 boundary terms. If we utilize a geographical orientation where we call the borders east, north, west and

south, we will get the following boundary terms:

$$\begin{aligned} BC_{east} &= (P_x^{-1}E_{NN} \otimes I_M \otimes \Sigma_{east}) \\ &\quad \cdot \Big((I_N \otimes I_M \otimes K_{east})\boldsymbol{u} - \boldsymbol{e}_{NN} \otimes \boldsymbol{g}_{east} \Big), \qquad (3.43a) \\ BC_{west} &= (P_x^{-1}E_{0N} \otimes I_M \otimes \Sigma_{west}) \\ &\quad \cdot \Big((I_N \otimes I_M \otimes K_{west})\boldsymbol{u} - \boldsymbol{e}_{0N} \otimes \boldsymbol{g}_{west} \Big), \qquad (3.43b) \\ BC_{south} &= (I_N \otimes P_y^{-1}E_{0M} \otimes \Sigma_{south}) \\ &\quad \cdot \Big((I_N \otimes I_M \otimes K_{south})\boldsymbol{u} - \boldsymbol{g}_{south} \otimes \boldsymbol{e}_{0M} \Big), \qquad (3.43c) \\ BC_{north} &= (I_N \otimes P_y^{-1}E_{MM} \otimes \Sigma_{north}) \\ &\quad \cdot \Big((I_N \otimes I_M \otimes K_{north})\boldsymbol{u} - \boldsymbol{g}_{north} \otimes \boldsymbol{e}_{MM} \Big). \qquad (3.43d) \end{aligned}$$

Here, P_x^{-1} comes from the Summation By Parts operator $D_x = P_x^{-1}Q_x$, and P_y^{-1} likewise from $D_y = P_y^{-1}Q_y$. The matrices and vectors that make sure that the operators apply on the right things are E_{0k}, E_{kk}, $\boldsymbol{e}_{0k}$ and $\boldsymbol{e}_{kk}$. I_k is an identity matrix of size $(k+1)\times(k+1)$, E_{0k} and E_{kk} are matrices of size $(k+1)\times(k+1)$ where

$$E_{0k} = \begin{bmatrix} 1 & 0 & \cdots & 0 \\ 0 & 0 & \cdots & 0 \\ \vdots & \vdots & \ddots & \\ 0 & 0 & & 0 \end{bmatrix}, \quad E_{kk} = \begin{bmatrix} 0 & 0 & \cdots & 0 \\ 0 & 0 & \cdots & 0 \\ \vdots & \vdots & \ddots & \\ 0 & 0 & & 1 \end{bmatrix}, \qquad (3.44)$$

and $\boldsymbol{e}_{0k}$ and $\boldsymbol{e}_{kk}$ are vectors of length $k+1$ defined as

$$\boldsymbol{e}_{0k} = \begin{bmatrix} 1 \\ 0 \\ \vdots \\ 0 \end{bmatrix}, \quad \boldsymbol{e}_{kk} = \begin{bmatrix} 0 \\ 0 \\ \vdots \\ 1 \end{bmatrix}. \qquad (3.45)$$

The framework for the boundary terms in (3.43) is based on the notion of characteristic boundary conditions. Analysis shows (see Appendix B) that the characteristic variables at the eastern boundary become

$$\begin{aligned} c_1^{east}(\boldsymbol{r}) &= a_1^{east}\frac{1}{2}\Big(\eta(\boldsymbol{r})H_z(\boldsymbol{r}) + E_y(\boldsymbol{r})\Big), \qquad (3.46a) \\ c_2^{east}(\boldsymbol{r}) &= a_2^{east}E_x(\boldsymbol{r}), \qquad (3.46b) \\ c_3^{east}(\boldsymbol{r}) &= a_3^{east}\frac{1}{2}\Big(-\eta(\boldsymbol{r})H_z(\boldsymbol{r}) + E_y(\boldsymbol{r})\Big), \qquad (3.46c) \end{aligned}$$

where a_1^{east}, a_2^{east} and a_3^{east} are arbitrary constants. Variable c_1^{east} corresponds to the positive eigenvalue $\lambda_1 = \lambda^+ = c$ of equation (B.9) and this is the characteristic variable that remains constant on characteristic curves moving in the positive x-direction, i.e. out of the computational domain. c_3^{east} on the other hand corresponds to the negative eigenvalue $\lambda_3 = \lambda^- = -c$, and this is the variable that is connected to the ingoing characteristic curve, i.e. the one that we will make use of in the boundary condition on the eastern border, $x = 1$.

In the same way but at the other three outer boundaries, the characteristic variables are

$$c_1^{west}(\boldsymbol{r}) = a_3^{west}\frac{1}{2}\Big(-\eta(\boldsymbol{r})H_z(\boldsymbol{r}) + E_y(\boldsymbol{r})\Big), \tag{3.47a}$$
$$c_2^{west}(\boldsymbol{r}) = a_2^{west}E_x(\boldsymbol{r}), \tag{3.47b}$$
$$c_3^{west}(\boldsymbol{r}) = a_1^{west}\frac{1}{2}\Big(\eta(\boldsymbol{r})H_z(\boldsymbol{r}) + E_y(\boldsymbol{r})\Big), \tag{3.47c}$$

$$c_1^{north}(\boldsymbol{r}) = a_1^{north}\frac{1}{2}\Big(-\eta(\boldsymbol{r})H_z(\boldsymbol{r}) + E_x(\boldsymbol{r})\Big), \tag{3.48a}$$
$$c_2^{north}(\boldsymbol{r}) = a_2^{north}E_y(\boldsymbol{r}), \tag{3.48b}$$
$$c_3^{north}(\boldsymbol{r}) = a_3^{north}\frac{1}{2}\Big(\eta(\boldsymbol{r})H_z(\boldsymbol{r}) + E_x(\boldsymbol{r})\Big) \tag{3.48c}$$

$$c_1^{south}(\boldsymbol{r}) = a_3^{south}\frac{1}{2}\Big(\eta(\boldsymbol{r})H_z(\boldsymbol{r}) + E_x(\boldsymbol{r})\Big), \tag{3.49a}$$
$$c_2^{south}(\boldsymbol{r}) = a_2^{south}E_y(\boldsymbol{r}), \tag{3.49b}$$
$$c_3^{south}(\boldsymbol{r}) = a_1^{south}\frac{1}{2}\Big(-\eta(\boldsymbol{r})H_z(\boldsymbol{r}) + E_x(\boldsymbol{r})\Big), \tag{3.49c}$$

where a_1, a_2 and a_3 are arbitrary constants. Again, variable c_1 corresponds to the positive eigenvalue $\lambda_1 = \lambda^+ = c$ of equation (B.9) and c_3 belongs to $\lambda_3 = \lambda^- = -c$. Because of the general coordinate system in (B.9) where $\hat{\boldsymbol{e}}_\xi$ is the outward pointing normal, this means that c_3 will be the ingoing characteristic variable at any boundary. We choose $a_i = 1$ and denote the transformation from the field variables to characteristic variables K. This gives

$$\boldsymbol{c}(x,y) = \begin{bmatrix} c_1(x,y) \\ c_2(x,y) \\ c_3(x,y) \end{bmatrix} = K \begin{bmatrix} H_z(x,y) \\ E_x(x,y) \\ E_y(x,y) \end{bmatrix} = K\boldsymbol{u}(x,y) \tag{3.50}$$

where in particular the transformation matrices at the boundaries become

$$K_{east} = \begin{bmatrix} \frac{1}{2}\eta & 0 & \frac{1}{2} \\ 0 & 1 & 0 \\ -\frac{1}{2}\eta & 0 & \frac{1}{2} \end{bmatrix}, \quad K_{west} = \begin{bmatrix} -\frac{1}{2}\eta & 0 & \frac{1}{2} \\ 0 & 1 & 0 \\ \frac{1}{2}\eta & 0 & \frac{1}{2} \end{bmatrix}, \tag{3.51a}$$
$$K_{south} = \begin{bmatrix} \frac{1}{2}\eta & \frac{1}{2} & 0 \\ 0 & 0 & 1 \\ -\frac{1}{2}\eta & \frac{1}{2} & 0 \end{bmatrix}, \quad K_{north} = \begin{bmatrix} -\frac{1}{2}\eta & \frac{1}{2} & 0 \\ 0 & 0 & 1 \\ \frac{1}{2}\eta & \frac{1}{2} & 0 \end{bmatrix}. \tag{3.51b}$$

Now, in (3.43), $\boldsymbol{g}$ are the vectors containing the boundary data. With the explanation of characteristic variables above,

$$\tilde{\boldsymbol{g}}_{i,j}(t) = \begin{bmatrix} c_1(x_i,y_j) \\ c_2(x_i,y_j) \\ c_3(x_i,y_j) \end{bmatrix} \tag{3.52}$$

as the boundary data at grid point (x_i, y_j), our $\boldsymbol{g}$'s become

$$\boldsymbol{g}_{north} = \begin{bmatrix} \tilde{\boldsymbol{g}}_{0,M}(t) \\ \tilde{\boldsymbol{g}}_{1,M}(t) \\ \vdots \\ \tilde{\boldsymbol{g}}_{N,M}(t) \end{bmatrix}, \quad \boldsymbol{g}_{south} = \begin{bmatrix} \tilde{\boldsymbol{g}}_{0,0}(t) \\ \tilde{\boldsymbol{g}}_{1,0}(t) \\ \vdots \\ \tilde{\boldsymbol{g}}_{N,0}(t) \end{bmatrix}, \tag{3.53}$$

$$\boldsymbol{g}_{east} = \begin{bmatrix} \tilde{\boldsymbol{g}}_{N,0}(t) \\ \tilde{\boldsymbol{g}}_{N,1}(t) \\ \vdots \\ \tilde{\boldsymbol{g}}_{N,M}(t) \end{bmatrix}, \quad \boldsymbol{g}_{west} = \begin{bmatrix} \tilde{\boldsymbol{g}}_{0,0}(t) \\ \tilde{\boldsymbol{g}}_{0,1}(t) \\ \vdots \\ \tilde{\boldsymbol{g}}_{0,M}(t) \end{bmatrix}. \tag{3.54}$$

Finally to be explained in (3.43), the matrices Σ are 3×3 penalty matrices that should pick out the proper characteristic variable at each of the boundaries. Also, the choices of Σ determine the stability of the scheme, more on this topic in Section 4.6. Our choices of Σ are

$$\Sigma_{north} = \begin{bmatrix} 0 & 0 & -\frac{1}{2} \\ 0 & 0 & -\frac{1}{2\eta} \\ 0 & 0 & 0 \end{bmatrix}, \quad \Sigma_{south} = \begin{bmatrix} 0 & 0 & \frac{1}{2} \\ 0 & 0 & -\frac{1}{2\eta} \\ 0 & 0 & 0 \end{bmatrix}, \tag{3.55}$$

$$\Sigma_{east} = \begin{bmatrix} 0 & 0 & \frac{1}{2} \\ 0 & 0 & 0 \\ 0 & 0 & -\frac{1}{2\eta} \end{bmatrix}, \quad \Sigma_{west} = \begin{bmatrix} 0 & 0 & -\frac{1}{2} \\ 0 & 0 & 0 \\ 0 & 0 & -\frac{1}{2\eta} \end{bmatrix}. \tag{3.56}$$

Now that we have the framework for the boundary terms, all we have to do is to solve for $\boldsymbol{u}_t$ in equation (3.42), and let a standard Runge-Kutta method take care of the time-stepping required to yield EM-field values at different times t.

3.2.1.1 Problem Specific Scheme

In the previous section, we outlined a scheme that dealt with the case of a one-material domain. Our main interest is to look at the material discontinuity between our two materials. To do that we must connect two such single material regions. This requires a bigger grid matrix, and a set of interface conditions between the regions. These interface conditions can be handled much like ordinary boundary conditions, only with a slightly different penalty matrix. For specific choices of interface conditions and penalty matrices pertaining to these we refer to Section 4.6 where stability will be considered, and penalty matrices chosen.

4 Numerical Results

The methods outlined in chapter 3 have been implemented into computer codes. The program for the spectral element method was written in MATLAB, and the finite difference method implemented in FORTRAN. With these codes, a few simple tests were carried out to test the performance of the methods. Although the problem set-up was identical for the two cases, and the numerical schemes both utilize characteristic boundary conditions, the codes were implemented in different computer languages, and consequently the comparisons must be taken with a pinch of salt. They might however be able to show some general tendencies.

4.1 Total Field Solutions

What one ultimately seeks, are the electric and magnetic fields in space and time. Here, we first take a look at the electric field $\boldsymbol{E}(\boldsymbol{r}, t)$.

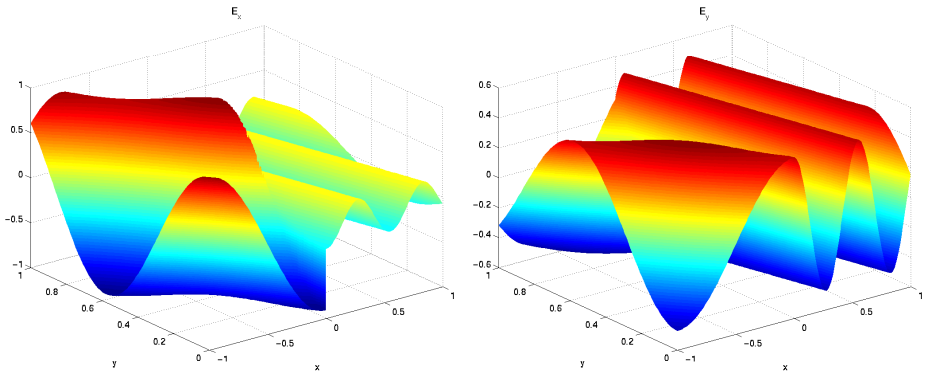

Figure 4.1. Spectral method 10^{th} order solution for the total $\boldsymbol{E}$-field at $t = 1$. A wave with amplitude 1 is incident from the left at an angle $\theta_i = \pi/3$ to the discontinuity normal. The graphs show the E_x and E_y components respectively.

In the plots in Figure 4.1 we see the x and y-components of the electric field solution with the spectral method scheme at time $t = 1$. A polynomial order of 10 has been used in the interpolation, and the wave is incident at the angle $\theta_i = \frac{\pi}{3}$. The base mesh has triangles of edge size 0.1, glance at Figure 3.1 for this grid. We notice that E_y is continuous over the material interface, as predicted by the interface conditions in Maxwell's equations (2.5a), while E_x shows a discontinuity at $x = 0$ due to the different material constants.

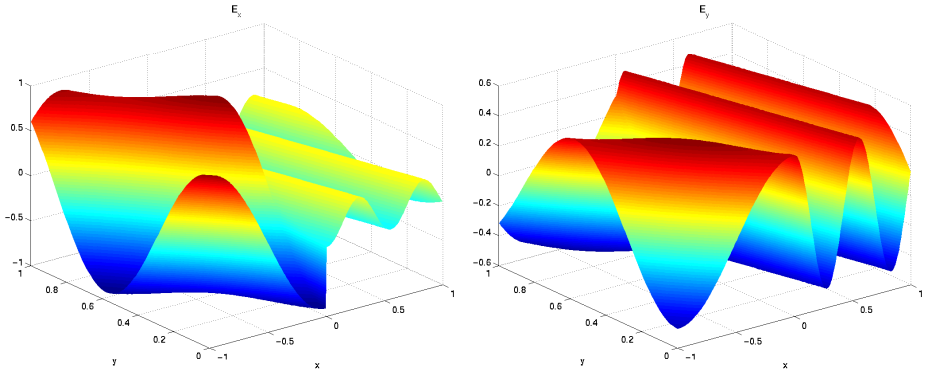

Figure 4.2. Finite difference method 6^{th} order solution for the total $\boldsymbol{E}$-field at $t = 1$. A wave with amplitude 1 is incident from the left at an angle $\theta_i = \pi/3$ to the discontinuity normal. The graphs show the E_x and E_y components respectively.

The results of the finite difference calculations can be viewed in Figure 4.2. These calculations were performed with a 6^{th} order scheme, on a $\Delta x = \Delta y = 0.01$

structured rectangular grid. Both the E_x and the E_y components of the electric field show the same properties as previously discussed for the spectral method calculation.

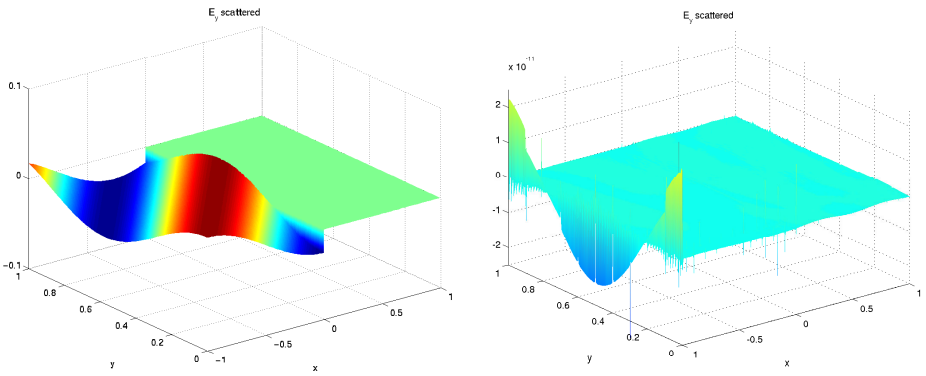

Figure 4.3. Spectral method 10^{th} order solution for the reflected $\boldsymbol{E}_y$-field travelling to the left at $t = 1$. a.) The incoming wave with amplitude 1 is incident from the left at an angle $\theta_i = \pi/3$ to the discontinuity normal. b.) The wave is incident at the so-called Brewster angle, $\theta_i = \theta_B$.

A characteristic physical property of our setup is that a wave entering the second material refracts and changes direction as well as amplitude. This can clearly be seen in the solutions in Figures 4.1 and 4.2. The material discontinuity also produces a reflected wave, which is of variable magnitude depending on the angle of incidence θ_i. Figure 4.3 shows the scattered fields, i.e. the part of $\boldsymbol{E}$ that travels to the left, calculated by means of the spectral method. For $\theta_i = \pi/3$ there is a significant reflection, but for the Brewster angle, there is a vanishingly small reflection, which is clearly indicated by the scale factor of 10^{-11} on the vertical axis in Figure 4.3.b. This is as it should be since the Brewster angle is defined as the angle that produces a reflection coefficient $\Gamma_{||} = 0$, see relation (2.34a).

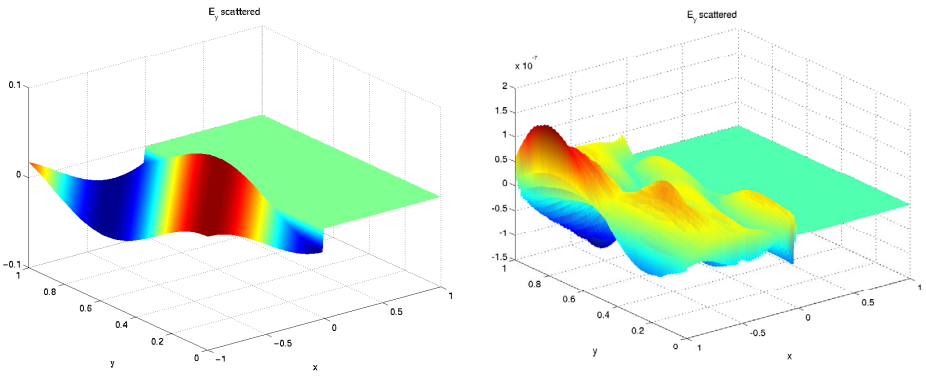

Figure 4.4. Finite difference method 6^{th} order solution for the reflected $\boldsymbol{E}_y$-field travelling to the left at $t = 1$. a.) The incoming wave with amplitude 1 is incident from the left at an angle $\theta_i = \pi/3$ to the discontinuity normal. b.) The wave is incident at the so-called Brewster angle, $\theta_i = \theta_B$.

Finally, by looking merely at the scattered fields for the finite difference method in Figure 4.4, we can see that the code accurately reproduces a reflection of the wave at the material discontinuity. The case where the incident angle is the Brewster angle, is also handled well. The scale factor on the vertical axis in Figure 4.4.b is 10^{-7} which indicates that there is essentially no reflection. The Brewster-reflections in 4.3.b and 4.4.b have different structures and are of different size. Worth mentioning in this context is that the spectral scheme and the finite difference schemes are of different order, and also of different grid size. Nevertheless, the schemes do have in common that the Brewster-reflections are very small.

4.2 Errors

There are numerous different types of errors to look at, but the perhaps most frequently used measure is the L_2-norm. If the displacement between the analytical solution $\boldsymbol{E}_A$ and the numerical solution $\boldsymbol{E}_N$ is $\boldsymbol{e} = \boldsymbol{E}_A - \boldsymbol{E}_N$, then the L_2-norm of this error is

$$\|\boldsymbol{e}\|_{L_2} = \sqrt{\frac{\sum_{i=1}^{N} \boldsymbol{e}_i^2}{N}}. \tag{4.1}$$

Here, the summation runs over all the N discrete points $\boldsymbol{r}_i$ where we have an approximation to the electric field solution available. In this way, the L_2-error becomes a mean value estimate of the local errors in each point of the computational domain. The L_2-norm will be used for all error estimates in this report.

4.3 Order Verification

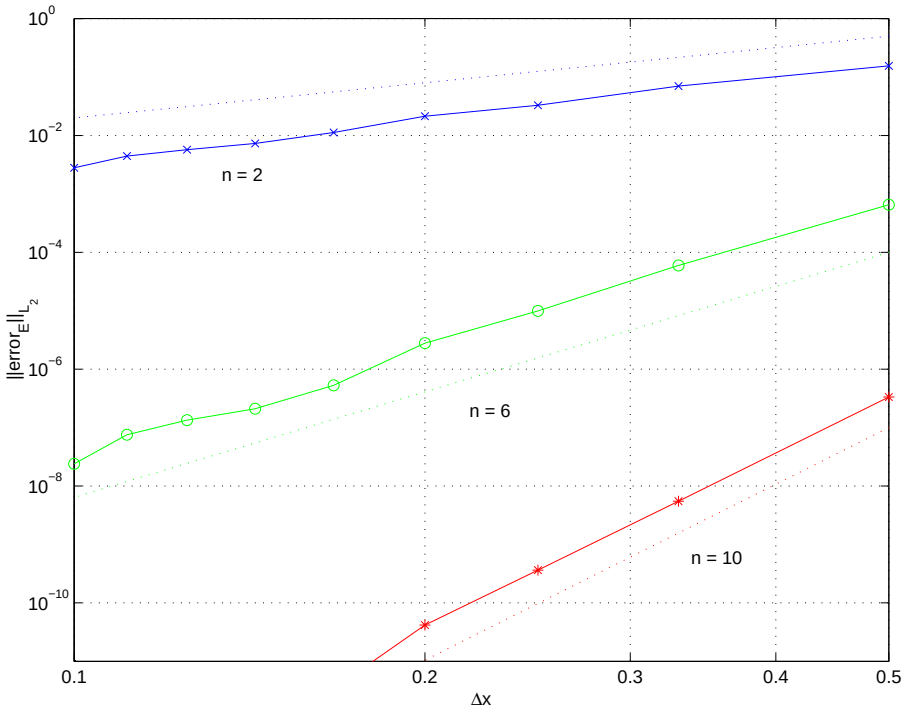

Figure 4.5. Spectral methods of the 2^{nd}, 6^{th} and 10^{th} order schemes at $t = 1$ for $\theta_i = \pi/3$. The $\boldsymbol{E}$-error in the numerical solution is plotted versus a characteristic sidelength Δx of a grid triangle. The dotted lines are the theoretical slopes.

Figure 4.5 shows the error reduction of the spectral method for polynomial orders 2, 6 and 10. With decreasing grid size, the errors of the numerical solution shrink accordingly. The discrepancy from the theoretical slopes of n^{th} order methods in general, i.e. the dotted curves that show $\|\boldsymbol{e}\|_{L_2} = \mathcal{O}(\Delta x)^n$, is small, which indicates that the schemes are performing as they should.

One reason why the numerical results do not show completely straight lines is most likely because the calculations are performed on unstructured grids where it is difficult to get a good estimate of a "characteristic triangle length" Δx. Here, Δx is chosen as the edge length of all the mesh triangles at the outer boundary.

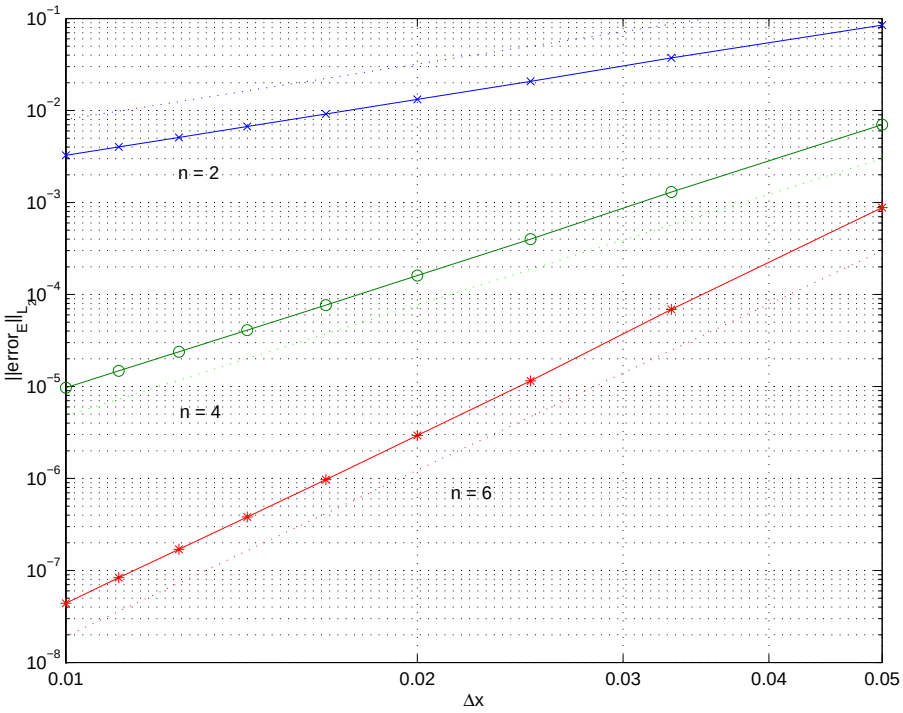

Figure 4.6. Finite difference methods of the 2^{nd}, 4^{th} and 6^{th} order schemes at $t = 1$ for $\theta_i = \pi/3$. The $\boldsymbol{E}$-error in the numerical solution is plotted versus the grid point spacing Δx. The dotted lines are the theoretical slopes.

The finite difference scheme also performs properly as we change the grid spacing, which can be seen in Figure 4.6. As the grid spacing Δx decreases, the $\boldsymbol{E}$-errors decrease as predicted by the theory, whose results are depicted by the dotted lines.

4.4 Memory Consumption

A vital point a large scale calculation is the one concerning the memory requirements. To store the electric and magnetic field values in each discretization point requires an amount of computer memory proportional to the number of discretization points. The memory of our particular computer limits the discretization density of the problem at hand, and therefore it is interesting to analyze how the error of the calculation varies with degree of freedom, i.e. the number of discretization points.

In Figure 4.7 the $\boldsymbol{E}$-errors of the spectral calculations are graphed related to the degrees of freedom. Naturally, increasing the number of discretization points shrinks the error, but more importantly, by increasing the order of the calculation it is possible to reach a smaller error with fewer degrees of freedom. This means that by using a higher order method it is possible to use less computer memory and still reach the same error level as with a lower order method.

The same type of results, i.e. how the error varies with the number of grid points, are drawn in Figure 4.8 for the finite difference calculations.

Figure 4.9 shows a comparison of the spectral method and the finite difference method in terms of degrees of freedom. Spectral method results are the dotted lines whereas the finite difference results are drawn in solid lines. Ideally, one

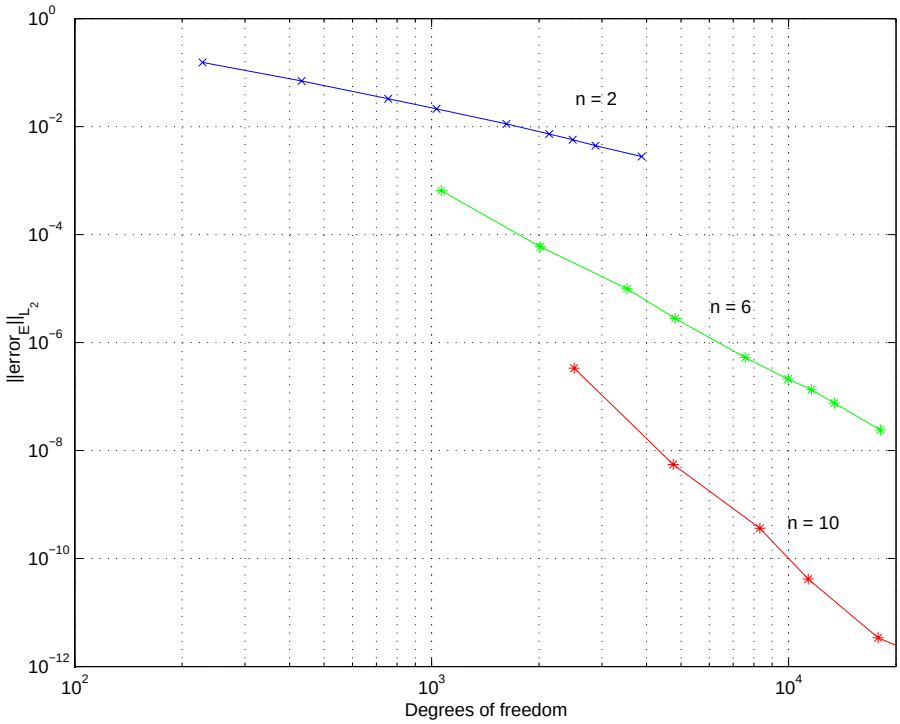

Figure 4.7. Spectral methods of the 2^{nd}, 6^{th} and 10^{th} order schemes at $t = 1$ for $\theta_i = \pi/3$. The $\boldsymbol{E}$-error in the numerical solution is plotted versus the degrees of freedom.

seeks small errors and few degrees of freedom. A spectral method and a finite difference method of the same order show similar growths in error as the number of discretization points is decreased. There is however a small but noticeable difference for the lowest order methods. Here, a given error value can be reached with slightly fewer degrees of freedom with the spectral method.

A major difference between the methods is that the finite difference method can raise the order of accuracy and keep the degrees of freedom constant. The disadvantage of the spectral method is that the number of discretization points automatically increases as the order grows.

4.5 Efficiency

An efficient calculation would compute an accurate solution quickly. One would therefore be interested in the elapsed total computational time needed to reach a certain accuracy level. We would like to compare the efficiencies of our two different schemes, and since we in both cases use the same Runge-Kutta scheme to do the time integration, it suffices to look at the time needed to perform a single time step. However, the computer programs used in the calculations were written in FORTRAN for the finite difference method and in MATLAB for the spectral method. They were also coded by different people, making it unfair to just clock the calculations and compare the results straight off. Another approach would be to estimate the number of floating point operations needed for the two methods.

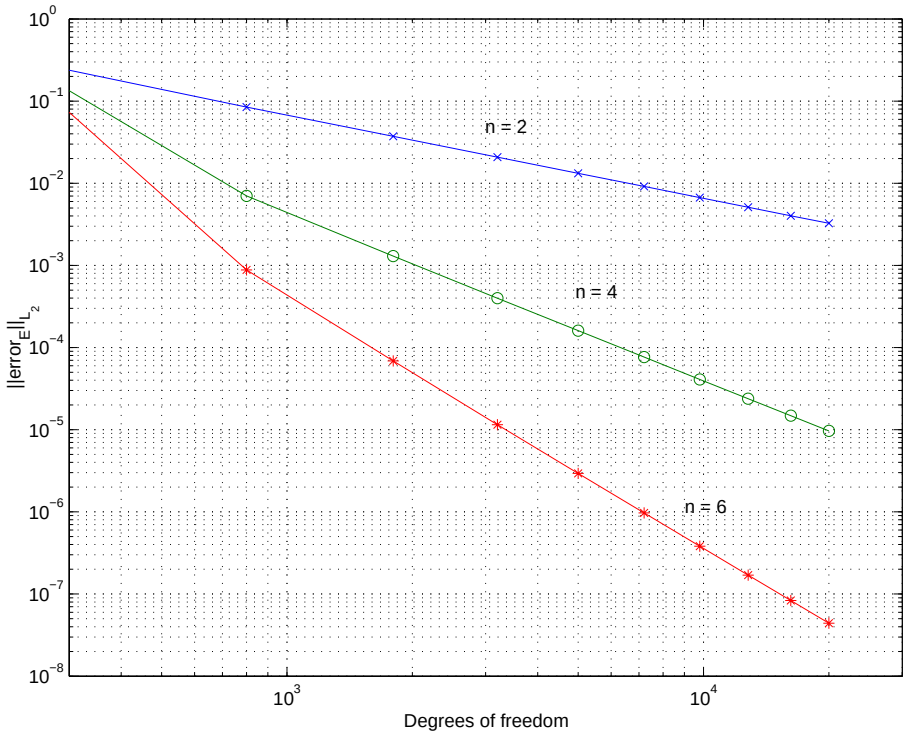

Figure 4.8. Finite difference methods of the 2^{nd}, 4^{th} and 6^{th} order schemes at $t = 1$ for $\theta_i = \pi/3$. The $\boldsymbol{E}$-error in the numerical solution is plotted versus the degrees of freedom.

4.5.1 Finite Difference Operations Count

Let us first try to count the number of floating point operations needed to advance one time step in the leanest, most efficient form of a possible finite difference computational code. Such a code is somewhat of a utopia because there are usually extra organizatory functions needed. In addition, the more efficient a code is written, the more fancy tricks it uses, and hence the program becomes less clear and lucid. In order not to leave an incomprehensible code contribution to posterity, a slightly simpler but also slightly less efficient program might be the preferable choice. However, in order to make a simple comparison for our purposes, these theoretical high efficiency limits will do.

For both the finite difference and the spectral method, we are solving the transverse electric mode equations (2.18a), (2.18b) and (2.18c).

In the case of an arbitrary even n-th order finite difference scheme, a single partial derivative is written $\frac{\partial K(\boldsymbol{r}_i)}{\partial x_j} = \sum_{l=1}^{n} a_l K(\boldsymbol{r}_l)$, where $x_j \in \{x, y, z\}$ and K is anything differentiable at the discrete point $\boldsymbol{r}_i$, e.g. $E_x(\boldsymbol{r}_i)$, $E_y(\boldsymbol{r}_i)$ or $H_z(\boldsymbol{r}_i)$. Such a differentiation is in general going to include $n - 1$ addition operations as well as n multiplications. Take a quick peek at equations (3.33), (3.34) and (3.35) to verify this. So, one differentiation corresponds to $2n - 1$ floating point

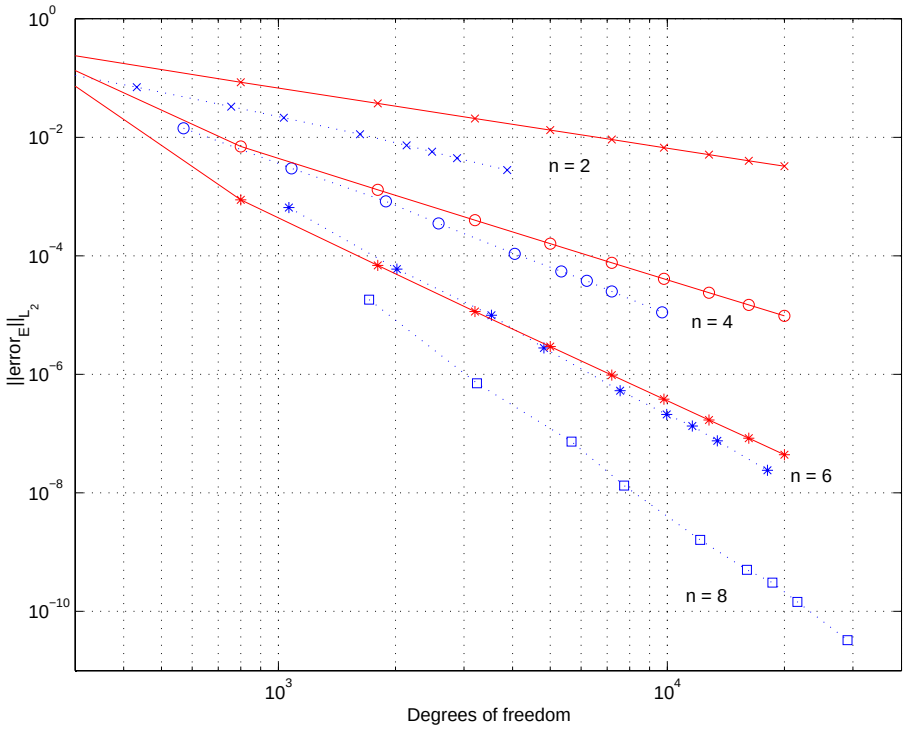

Figure 4.9. Spectral methods of the 2^{nd}, 4^{th}, 6^{th} and 8^{th} order schemes and finite difference results of orders 2, 4 and 6 at $t = 1$ for $\theta_i = \pi/3$. The $\boldsymbol{E}$-error in the numerical solution is plotted versus the degrees of freedom. The dotted lines are from the calculations with the spectral method and the solid lines are from the finite difference computations.

operations. If we reformulate equations (2.18a), (2.18b) and (2.18c) as

$$\frac{\partial E_x}{\partial t} = \frac{1}{\epsilon}\frac{\partial H_z}{\partial y} \tag{4.2a}$$

$$\frac{\partial E_y}{\partial t} = \frac{-1}{\epsilon}\frac{\partial H_z}{\partial x} \tag{4.2b}$$

$$\frac{\partial H_z}{\partial t} = \frac{1}{\mu}\left(\frac{\partial E_x}{\partial y} - \frac{\partial E_y}{\partial x}\right), \tag{4.2c}$$

we need $2n-1$ operations for the derivative in (4.2a), and one operation to include the multiplicative factor $\frac{1}{\epsilon}$. In the same way, we need $2n$ operations to evaluate the right hand side of (4.2b). Because (4.2c) has two derivatives and an extra subtraction, it takes $4n$ operations to calculate $\frac{\partial H_z}{\partial t}$. When we add all this up, we get $8n$ floating point operations per discretization point and time iteration. With a total of N_{pts}^{FD} discretization points in the entire computational domain, the calculation requires

$$^{2D}N_{flops}^{FD} = 8nN_{pts}^{FD} \tag{4.3}$$

floating point operations, i.e. the work effort is linear in the order n and in the number of grid points. This estimate disregards all influences of boundary conditions, but unless the domain is dominated by the boundary, which is not the case for our "bulky" rectangle, the boundary flops will only provide a minor contribution to the total number of operations.

As a generalization of the two-dimensional result (4.3) to three dimensions we need to remember that the transverse electric and magnetic mode simplifications do not hold in a general three-dimensional geometry. Instead, we have to solve the six scalar equations included in (2.17a) and (2.17b). Adding up the floating

point operations in the same way as above yields

$$ {}^{3D}N_{flops}^{FD} = 24nN_{pts}^{FD}. \tag{4.4} $$

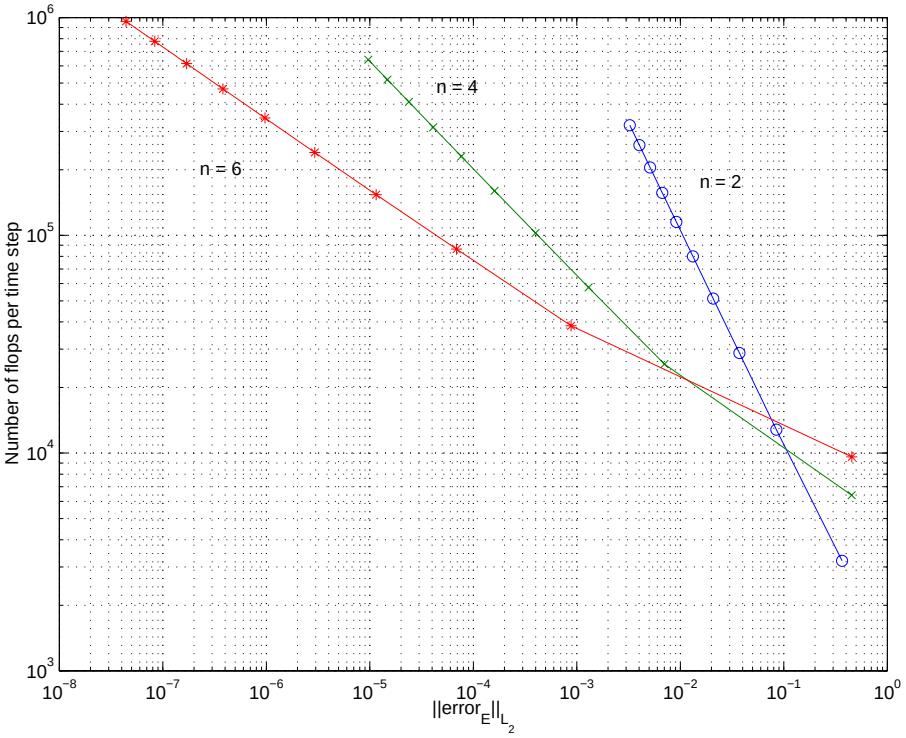

Figure 4.10. The number of floating point operations per time step for the ideal numerical finite difference method is plotted versus the $\boldsymbol{E}$-error for different orders n at $t = 1$ for $\theta_i = \pi/3$.

Figure 4.10 shows the variation of the number of floating point operations needed for one time iteration with the finite difference scheme in our specific two-dimensional case. Varying the grid size of the mesh has produced the results. If we disregard the rightmost points, i.e. where the grid is so coarsely spaced that error becomes greater than 10%, we see that a specific error level is reached with significantly fewer floating point operations when we utilize methods with a higher order. When the order of the scheme is increased, the need for densely spaced grid points decreases, and hence the performance of the code is improved.

4.5.2 Spectral Method Operations Count

Counting the number of operations for an ideal finite difference scheme was easy. For the spectral method outlined in this report, it is slightly more complicated. Instead of merely looking at a specific discretization point, we have to deal with all the interpolation points within a simplex, which in our two-dimensional material discontinuity case becomes a triangle.

The general spectral scheme in equation (3.16) can be simplified to the following two-dimensional transverse electric mode scheme for straight-sided triangles with constant material parameters:

$$\frac{\partial E_x}{\partial t} = \frac{1}{\epsilon}\left(\frac{\partial H_z}{\partial y} + \frac{|\nabla u|}{\bar{Z}}\Big(Z^n n_y[H_z] - n_x\big(\hat{\boldsymbol{n}}\cdot[\boldsymbol{E}]\big) - [E_x]\Big)_{\partial D}\right), \tag{4.5a}$$

$$\frac{\partial E_y}{\partial t} = \frac{-1}{\epsilon}\left(\frac{\partial H_z}{\partial x} - \frac{|\nabla u|}{\bar{Z}}\Big(Z^n n_x[H_z] - n_y\big(\hat{\boldsymbol{n}}\cdot[\boldsymbol{E}]\big) - [E_y]\Big)_{\partial D}\right), \tag{4.5b}$$

$$\frac{\partial H_z}{\partial t} = \frac{1}{\mu}\left(\frac{\partial E_x}{\partial y} - \frac{\partial E_y}{\partial x} + \frac{|\nabla u|}{\bar{Y}}\Big(Y^n n_x[E_y] - Y^n n_y[E_x] - [H_z]\Big)_{\partial D}\right). \tag{4.5c}$$

This spectral scheme consists of two contributions in each triangle, the fluxes over the triangle edges and the interpolation approximations to the differentiation operator in the entire triangle. In the flux-facial terms, u is the parametrical description of the triangle face, $\hat{\boldsymbol{n}}$ is the outward pointing normal to the face u, and $Z^{l,n} = \frac{1}{Y^{l,n}} = \sqrt{\frac{\mu^{l,n}}{\epsilon^{l,n}}}$, $\bar{Z} = Z^l + Z^n$, $\bar{Y} = Y^l + Y^n$ where 'n' indicates the neighbor triangle while 'l' refers to the local triangle. In addition, we remember that $[\boldsymbol{E}] = \boldsymbol{E}^n - \boldsymbol{E}^l$.

All but the factors including field variables can be precomputed, and they need not be re-evaluated each time step. Hence, all that needs to be done is to summarize the precalculated parameters in one constant for each term that will be multiplied by either the field bracket or the derivative.

The '∂D-terms' only include bracketed field terms, which means that the discretization points on the triangle faces only interact with a single neighbor point. The approximation of the spatial partial derivative, on the other hand, is in general dependent on all the field values in triangle D. This means that the differentiation will be implemented in terms of a matrix, multiplied by a vector of the field values at all interpolation points. There are two such differentiation matrices $D^{\xi}_{ij} = \frac{\partial L_j(\boldsymbol{\xi}_i)}{\partial \xi}$ and $D^{\eta}_{ij} = \frac{\partial L_j(\boldsymbol{\xi}_i)}{\partial \eta}$, and they are defined on a standard element I, so that the matrices operate with respect to the coordinate system $\boldsymbol{\xi}$ local to I. Because of this, a coordinate transformation has to be done to get back to the Cartesian coordinates.

The partial derivative $\frac{\partial H_z(\boldsymbol{r}_i)}{\partial y}$ can be approximated by $\sum_j \left(\frac{\partial \xi}{\partial y}D^{\xi}_{ij} + \frac{\partial \eta}{\partial y}D^{\eta}_{ij}\right)H_z(\boldsymbol{r}_j)$. To get all the derivatives in all points $\boldsymbol{r}_j$, this becomes our matrix multiplication $\left(\frac{\partial \xi}{\partial y}D^{\xi} + \frac{\partial \eta}{\partial y}D^{\eta}\right)\boldsymbol{H}_z$. If we utilize an n^{th} order scheme, our triangle will have $n+1$ interpolation points on each face and $N = \frac{1}{2}(n+1)(n+2)$ points total in the triangle. The differentiation matrix $\left(\frac{\partial \xi}{\partial y}D^{\xi} + \frac{\partial \eta}{\partial y}D^{\eta}\right)$ can be precomputed and it will be of size $N \times N$ operating on a vector consisting of N points. This gives $N(2N-1)$ floating point operations per matrix multiplication. We need 4 such matrix operations since we have 4 physical spatial derivatives. Hence, in a total of $4N(2N-1)$ operations, we have estimates of the derivatives in all points of the triangle.

In the flux terms, the brackets $[E_x]$, $[E_y]$, and $[H_z]$ are facial differences that have to be evaluated in $3(n+1)$ points each, thus requiring $9(n+1)$ operations altogether in one element. The dot product $\hat{\boldsymbol{n}}\cdot[\boldsymbol{E}]$ can be calculated in all face points using $9(n+1)$ flops. With these calculated we can multiply out and add the

factors of the flux terms. In each of (4.5a), (4.5b) and (4.5c) a number of $15(n+1)$ operations is necessary to do these multiplications and additions, i.e. $45(n+1)$ in total. Since each face is shared by two elements, we can save some work by re-using the scalar product $\hat{\boldsymbol{n}} \cdot [\boldsymbol{E}]$ in the neighbor elements, where it will be the same. This means that we can reduce the effort to compute the three flux terms from $63(n+1)$ to $58.5(n+1)$ on average.

Adding the flux terms to the differentiated fields and multiplying by the material constants costs $N + 3(n+1)$ operations for equations (4.5a) and (4.5b) respectively, and $2N + 3(n+1)$ operations for equation (4.5c).

Summing up all the floating point operations required for one time iteration in the spectral scheme in the entire computational domain, we get

$$\begin{aligned} {}^{2D}N^S_{flops} &= \Big(4N(2N-1) + 58.5(n+1) + 4N + 9(n+1)\Big)N^S_{el} \\ &= \Big(2(n+1)^2(n+2)^2 + 67.5(n+1)\Big)N^S_{el}, \end{aligned} \tag{4.6}$$

where N is the number of nodes per triangle, n the order of the interpolation polynomial and N^S_{el} is the total number of triangles in the whole region.

By the same kind of counting, this can also be generalized to three dimensions where the work effort will be

$$\begin{aligned} {}^{3D}N^S_{flops} = \Bigg(&\frac{2}{3}(n+1)^2(n+2)^2(n+3)^2 - \frac{2}{3}(n+1)(n+2)(n+3) \\ &+ 100(n+1)(n+2)\Bigg)N^S_{el}, \end{aligned} \tag{4.7}$$

n being the order of the method and N^S_{el} the number of tetrahedra filling out the domain.

If we vary the interpolation order n as we calculate the number of floating point operations, and at the same time relate this to the error in the calculation, we get an estimate of efficiency, represented in Figure 4.11. The graph shows that we can retain a certain error level by increasing the interpolation order and consequently get a slightly faster computation. The efficiency improvement reached by increasing the order n of the method, and at the same time reducing the number of elements N^S_{el} in the grid, grows larger as the requirements on the errors sharpen.

It is worth mentioning that in this theoretical estimate of the floating point operations for the spectral method, we have represented the differential operators with general, full matrices D^{ξ}_{ij} and D^{η}_{ij}. In the actual computer calculation, it turns out that many of the entries in these matrices actually are 0. By using an optimized matrix multiplication package in the computer code, sparser matrices will not require the same amount of computational power as full ones, and therefore the total number of floating point operations can be reduced in reality. This means that the results in (4.6) and (4.7) probably are underestimates of the actual efficiencies.

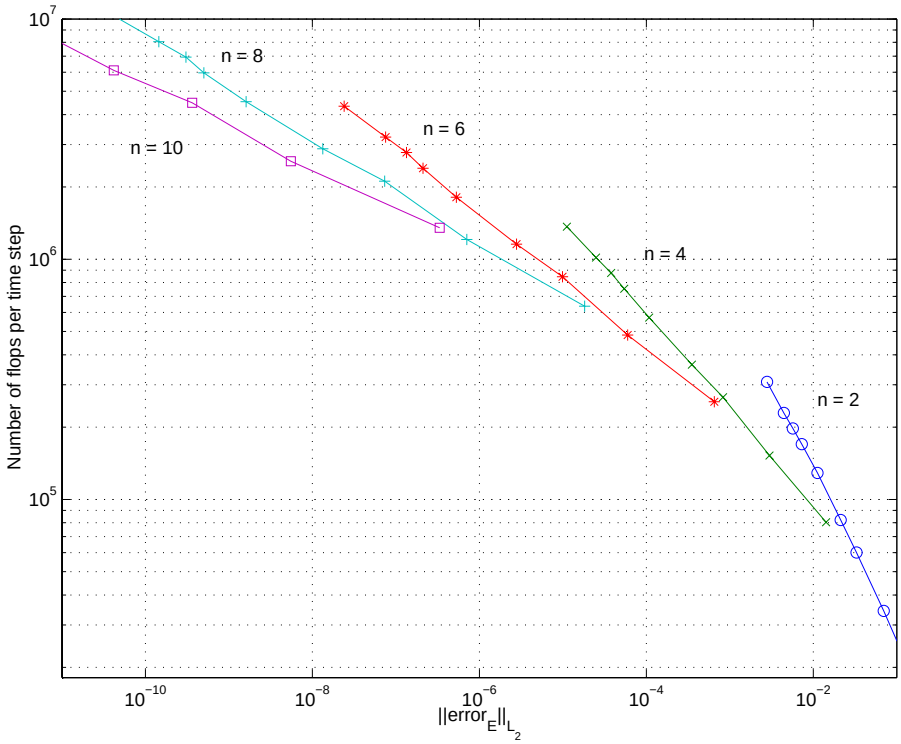

Figure 4.11. The number of floating point operations per time step for the ideal numerical spectral method is plotted versus the $\boldsymbol{E}$-error for different orders n at $t = 1$ for $\theta_i = \pi/3$.

4.5.3 Comparing the Methods

By putting the previously shown efficiency graphs for the spectral and finite difference methods on top of each other, we can make a fair comparison.

Figure 4.12 shows what one might have expected, i.e. that the finite difference scheme is more efficient than the spectral scheme. The largest difference between the finite difference curves and the spectral curves is about a factor of 6, and this occurs at the error level 10^{-3}. As the orders of the methods increase, the slopes of the curves tend to increase, and by a careful investigation, the slopes of the finite difference method appear to be slightly smaller than the slopes of the spectral method of equal order of accuracy. If we extrapolate the curves toward errors approaching zero, this means that the spectral methods will eventually outperform the finite difference schemes. This is only a theoretical scenario however; such low error levels are never used in practice.

When choosing a scheme for this simple two-dimensional problem, a high-order finite difference scheme would definitely be the one. However, the present problem is more or less tailored for the finite difference scheme. A more complicated geometry would definitely favor the spectral scheme, mainly because of the relative ease of constructing an unstructured grid. Besides, the performance of the spectral scheme is in reality better than our theoretical estimates show. This is due to optimized matrix-multiplying techniques that improve efficiency for the differentiation matrices that are not always full as they have been assumed to be in our reasoning.

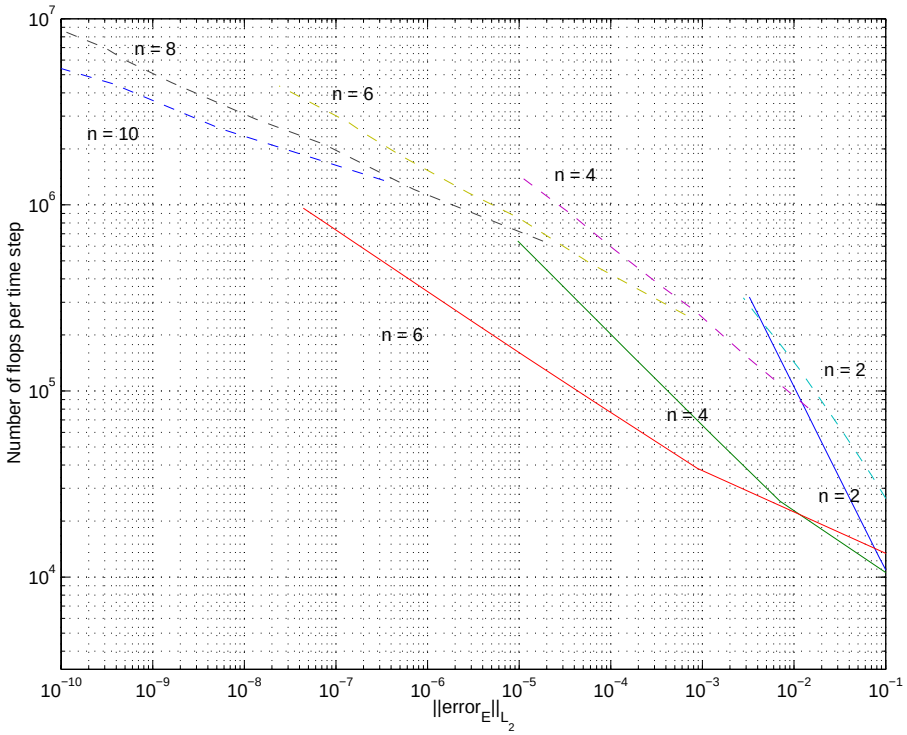

Figure 4.12. The number of floating point operations per time step plotted versus the $\boldsymbol{E}$-error for different grid point spacings Δx at $t = 1$ for $\theta_i = \pi/3$ as the order n is varied. The dashed lines correspond to the spectral scheme while the solid lines are from the finite difference calculations.

4.6 Stability

So far, we have only dealt with results of the calculations at $t = 1$. This is fine for the sake of comparing the schemes' performances, but what happens when we need to consider scenarios that elapse much longer in time? This brings out the question of stability.

4.6.1 Spectral Scheme

From a theoretical point of view, we can investigate stability by looking at the electric and magnetic energies and how they develop with time. The electric and magnetic energy densities are

$$\rho_{\boldsymbol{E}} = \frac{\epsilon|\boldsymbol{E}|^2}{2} \quad \text{and} \quad \rho_{\boldsymbol{H}} = \frac{\mu|\boldsymbol{H}|^2}{2} \tag{4.8}$$

respectively. If the electromagnetic energy in the system is non-growing, i.e. if

$$\frac{\partial}{\partial t}\int(\rho_{\boldsymbol{E}} + \rho_{\boldsymbol{H}})d\boldsymbol{r} \leq 0, \tag{4.9}$$

then certainly the system is stable.

We begin by looking at a single element D_k. If the $\boldsymbol{E}$-part of equation (3.12a) is multiplied by $\boldsymbol{E}_i = \boldsymbol{E}(\boldsymbol{r}_i)$ from the left, followed by a summation over i and

using that $\boldsymbol{E}_N = \sum_{i=1}^{N_D} \boldsymbol{E}_i L_i(\boldsymbol{r})$, then we reach

$$\begin{aligned}\int_{D_k} \left(\boldsymbol{E}_N \cdot \epsilon \frac{\partial \boldsymbol{E}_N}{\partial t} - \boldsymbol{E}_N \cdot (\boldsymbol{\nabla} \times \boldsymbol{H}_N) \right) d\boldsymbol{r} = \\ = \int_{\partial D_k} \tau \boldsymbol{E}_N \cdot \left(\hat{\boldsymbol{n}} \times \frac{Z^n[\boldsymbol{H}_N] - \hat{\boldsymbol{n}} \times [\boldsymbol{E}_N]}{Z^l + Z^n} \right) dS(\boldsymbol{r}).\end{aligned} \tag{4.10}$$

Rearranging this with $\frac{1}{2}\frac{\partial}{\partial t}\int_{D_k} \epsilon \boldsymbol{E}_N^2 d\boldsymbol{r} = \int_{D_k} \epsilon \boldsymbol{E}_N \frac{\partial \boldsymbol{E}_N}{\partial t} d\boldsymbol{r}$ yields

$$\begin{aligned}\frac{\partial}{\partial t}\int_{D_k} \rho_{\boldsymbol{E}} d\boldsymbol{r} = \frac{1}{2}\frac{\partial}{\partial t}\int_{D_k} \epsilon \boldsymbol{E}_N^2 d\boldsymbol{r} = \\ = \int_{D_k} \boldsymbol{E}_N \cdot (\boldsymbol{\nabla} \times \boldsymbol{H}_N) d\boldsymbol{r} \\ + \oint_{\partial D_k} \left(\tau \boldsymbol{E}_N \cdot \hat{\boldsymbol{n}} \times \frac{Z^n[\boldsymbol{H}_N] - \hat{\boldsymbol{n}} \times [\boldsymbol{E}_N]}{Z^l + Z^n} \right) dS(\boldsymbol{r}).\end{aligned} \tag{4.11}$$

In the same fashion, but with the $\boldsymbol{H}$-set of equations,

$$\begin{aligned}\frac{\partial}{\partial t}\int_{D_k} \rho_{\boldsymbol{H}} d\boldsymbol{r} = \frac{1}{2}\frac{\partial}{\partial t}\int_{D_k} \mu \boldsymbol{H}_N^2 d\boldsymbol{r} \\ = -\int_{D_k} \boldsymbol{H}_N \cdot (\boldsymbol{\nabla} \times \boldsymbol{E}_N) d\boldsymbol{r} \\ - \oint_{\partial D_k} \left(\tau \boldsymbol{H}_N \cdot \hat{\boldsymbol{n}} \times \frac{Y^n[\boldsymbol{E}_N] + \hat{\boldsymbol{n}} \times [\boldsymbol{H}_N]}{Y^l + Y^n} \right) dS(\boldsymbol{r})\end{aligned} \tag{4.12}$$

results. The total change in the energy $E_{D_k} = \int_{D_k} (\rho_{\boldsymbol{E}} + \rho_{\boldsymbol{H}}) d\boldsymbol{r}$ in element D_k becomes

$$\begin{aligned}\frac{\partial}{\partial t} E_{D_k} = \oint_{\partial D_k} \Bigg((\boldsymbol{H}_N \times \boldsymbol{E}_N) \cdot \hat{\boldsymbol{n}} - \tau \boldsymbol{H}_N \cdot \hat{\boldsymbol{n}} \times \frac{Y^n[\boldsymbol{E}_N] + \hat{\boldsymbol{n}} \times [\boldsymbol{H}_N]}{\bar{Y}} \\ + \tau \boldsymbol{E}_N \cdot \hat{\boldsymbol{n}} \times \frac{Z^n[\boldsymbol{H}_N] - \hat{\boldsymbol{n}} \times [\boldsymbol{E}_N]}{\bar{Z}} \Bigg) dS(\boldsymbol{r}),\end{aligned} \tag{4.13}$$

after utilizing the divergence theorem.

The total energy change in the entire computational domain, $\frac{\partial}{\partial t} E = \sum_k \frac{\partial}{\partial t} E_{D_k}$, will be a sum of the contributions of the surface integrals over all element faces. The inner faces will be counted twice, while the outer boundary faces only contribute once each.

Let us first look at the contributions from the boundary faces. At a boundary, $\boldsymbol{H}_N^n$ and $\boldsymbol{E}_N^n$ are set as boundary conditions, but it suffices to consider the case with homogeneous boundary conditions, $\boldsymbol{H}_N^n = \boldsymbol{E}_N^n = 0$. This means that $[\boldsymbol{E}_N] = -\boldsymbol{E}_N^l = -\boldsymbol{E}_N$ and putting this into equation (4.13) yields

$$\begin{aligned}\frac{\partial}{\partial t} E_{D_k} = \oint_{\partial D_k} \Bigg((\boldsymbol{H}_N \times \boldsymbol{E}_N) \cdot \hat{\boldsymbol{n}} \\ + \frac{\tau Y^n}{\bar{Y}} \boldsymbol{H}_N \cdot \hat{\boldsymbol{n}} \times \boldsymbol{E}_N - \frac{\tau Z^n}{\bar{Z}} \boldsymbol{E}_N \cdot \hat{\boldsymbol{n}} \times \boldsymbol{H}_N \\ + \frac{\tau}{\bar{Y}} \boldsymbol{H}_N \cdot \hat{\boldsymbol{n}} \times \hat{\boldsymbol{n}} \times \boldsymbol{H}_N + \frac{\tau}{\bar{Z}} \boldsymbol{E}_N \cdot \hat{\boldsymbol{n}} \times \hat{\boldsymbol{n}} \times \boldsymbol{E}_N \Bigg) dS(\boldsymbol{r}).\end{aligned} \tag{4.14}$$

Rearranging this using some vector identities gives

$$\frac{\partial}{\partial t}E_{D_k} = \oint_{\partial D_k} \Bigg(\Big(\tau \Big(\frac{Y^n}{\bar{Y}} + \frac{Z^n}{\bar{Z}} \Big) - 1 \Big) \boldsymbol{H}_N \cdot \hat{\boldsymbol{n}} \times \boldsymbol{E}_N + \frac{\tau}{\bar{Y}} \boldsymbol{H}_N \cdot \hat{\boldsymbol{n}} \times \hat{\boldsymbol{n}} \times \boldsymbol{H}_N + \frac{\tau}{\bar{Z}} \boldsymbol{E}_N \cdot \hat{\boldsymbol{n}} \times \hat{\boldsymbol{n}} \times \boldsymbol{E}_N \Bigg) dS(\boldsymbol{r}), \tag{4.15}$$

but

$$\frac{Y^n}{\bar{Y}} + \frac{Z^n}{\bar{Z}} = \frac{\frac{1}{Z^n}}{\frac{1}{Z^n} + \frac{1}{Z^l}} + \frac{Z^n}{\bar{Z}} = \frac{Z^l}{\bar{Z}} + \frac{Z^n}{\bar{Z}} = 1, \tag{4.16}$$

so the resulting boundary integral turns out to be

$$\frac{\partial}{\partial t}E_{D_k} = \oint_{\partial D_k} \Bigg((\tau - 1) \boldsymbol{H}_N \cdot \hat{\boldsymbol{n}} \times \boldsymbol{E}_N + \frac{\tau}{\bar{Y}} \boldsymbol{H}_N \cdot \hat{\boldsymbol{n}} \times \hat{\boldsymbol{n}} \times \boldsymbol{H}_N + \frac{\tau}{\bar{Z}} \boldsymbol{E}_N \cdot \hat{\boldsymbol{n}} \times \hat{\boldsymbol{n}} \times \boldsymbol{E}_N \Bigg) dS(\boldsymbol{r}). \tag{4.17}$$

Demanding that the integrand is less than or equal to 0 in accordance with (4.9), yields an inequality written in matrix quadratic form,

$$\boldsymbol{q}_N^T A \boldsymbol{q}_N = (\tau - 1) \boldsymbol{H}_N^T R \boldsymbol{E}_N + \frac{\tau}{\bar{Z}} \boldsymbol{E}_N^T R^2 \boldsymbol{E}_N + \frac{\tau}{\bar{Y}} \boldsymbol{H}_N^T R^2 \boldsymbol{H}_N \leq 0, \tag{4.18}$$

that will ensure stability for the scheme. Here R is the rotational operator matrix corresponding to '$\hat{\boldsymbol{n}}\times$',

$$R = \begin{bmatrix} 0 & -n_z & n_y \\ n_z & 0 & -n_x \\ -n_y & n_x & 0 \end{bmatrix}, \tag{4.19}$$

the vector $\boldsymbol{q}_N$ is defined as

$$\boldsymbol{q}_N = \begin{bmatrix} \boldsymbol{E}_N \\ \boldsymbol{H}_N \end{bmatrix} \tag{4.20}$$

moreover, the matrix A becomes

$$A = \begin{bmatrix} \frac{\tau}{\bar{Z}} R^2 & -\frac{1}{2}(\tau - 1) R \\ \frac{1}{2}(\tau - 1) R & \frac{\tau}{\bar{Y}} R^2 \end{bmatrix}. \tag{4.21}$$

A quadratic form can always be re-written like $\boldsymbol{q}_N^T A \boldsymbol{q}_N = \sum_i \lambda_i |\tilde{\boldsymbol{q}}_N|^2$, where λ_i are the eigenvalues to the matrix A. Here, the eigenvalues turn out to be

$$\lambda_{1-2} = 0 \tag{4.22a}$$

$$\lambda_{3-6} = \frac{-\tau(\bar{Y} + \bar{Z}) \pm \sqrt{\tau^2(\bar{Y} + \bar{Z})^2 + \bar{Y}^2\bar{Z}^2(\tau - 1)^2 - 4\tau^2\bar{Y}\bar{Z}}}{2\bar{Y}\bar{Z}}. \tag{4.22b}$$

Since we have positive material parameters ϵ and μ, Z and Y become positive, and therefore, $\bar{Z}$ and $\bar{Y}$ will also be positive. To make sure that relation (4.18) is

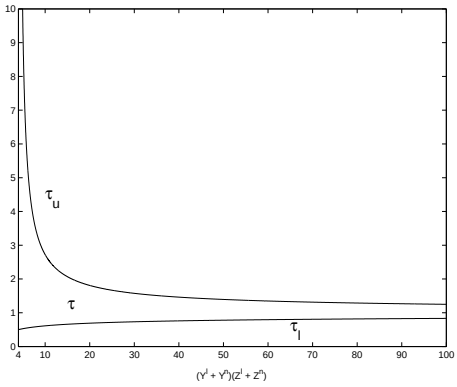

Figure 4.13. The limits on tau as $\bar{Y}\bar{Z}$ goes from 4 to ∞. The upper limit $\tau_u = (\bar{Y}\bar{Z} + 2\sqrt{\bar{Y}\bar{Z}})/(\bar{Y}\bar{Z} - 4)$ and the lower limit is $\tau_l = (\bar{Y}\bar{Z} - 2\sqrt{\bar{Y}\bar{Z}})/(\bar{Y}\bar{Z} - 4)$.

fulfilled, we need to require eigenvalues that are less than or equal to zero. The only way for this to hold for all eigenvalues λ_{1-6} is if

$$\bar{Y}^2\bar{Z}^2(\tau - 1)^2 - 4\tau^2\bar{Y}\bar{Z} \leq 0, \tag{4.23}$$

which means that

$$\frac{\bar{Y}\bar{Z} - 2\sqrt{\bar{Y}\bar{Z}}}{\bar{Y}\bar{Z} - 4} \leq \tau \leq \frac{\bar{Y}\bar{Z} + 2\sqrt{\bar{Y}\bar{Z}}}{\bar{Y}\bar{Z} - 4}. \tag{4.24}$$

A closer examination shows that $\bar{Y}\bar{Z} \geq 4$. When $\bar{Y}\bar{Z} = 4$, the allowed interval for τ is $[\frac{1}{2}, \infty)$, but as $\bar{Y}\bar{Z}$ grows, the interval shrinks continuously, and as $\bar{Y}\bar{Z} \to \infty$, $\tau \to 1$ which is shown graphically in Figure 4.13.

So, if we choose

$$\tau = 1, \tag{4.25}$$

inequality (4.18) will be fulfilled for all possible choices of real material parameters.

Looking at a single element like we just did, corresponds to the contribution to the energy growth from the outer boundaries only. Let us now consider the case when the computational domain consists of two elements D_l and D_n.

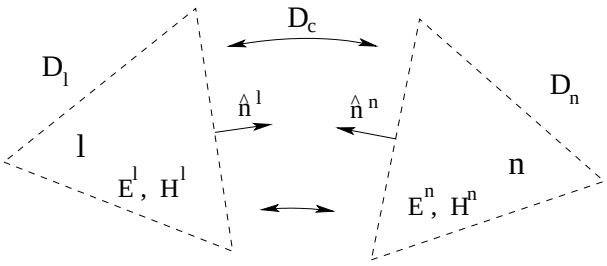

Figure 4.14. Two elements D_l and D_n connected at the face D_c where the surface normals of the two are $\hat{\boldsymbol{n}}^n = -\hat{\boldsymbol{n}}^l$.

In addition to the energy contributions from the outer faces described above, the inner faces will now also contribute. The extra feature of these is that they share the face with their neighboring element. The total energy growth in this system will be a sum of the surface integrals over both elements

$$\frac{\partial}{\partial t}E_{D_l+D_n} = \oint_{D_l}(\cdots) + \oint_{D_n}(\cdots) = \int_{\text{face}_{\text{inner}}} + \int_{\text{faces}_{\text{outer}}}. \tag{4.26}$$

Performing these integrations, there will be outer faces along which the integration will take exactly the same form as it did in equation (4.13). The difference is the integration over the inner face. Here, we need to set up equation (4.13) for the neighbor cell as well as for our local cell and then combine them.

For the local cell which we denote by D_l, we have

$$\begin{aligned}\frac{\partial}{\partial t}E_{D_l} = \oint_{\partial D_l}\Big((\boldsymbol{H}_N^l \times \boldsymbol{E}_N^l)\cdot\hat{\boldsymbol{n}}^l \\ - \tau\boldsymbol{H}_N^l\cdot\hat{\boldsymbol{n}}^l \times \frac{Y^n(\boldsymbol{E}_N^n - \boldsymbol{E}_N^l) + \hat{\boldsymbol{n}}^l\times(\boldsymbol{H}_N^n - \boldsymbol{H}_N^l)}{\bar{Y}} \\ + \tau\boldsymbol{E}_N^l\cdot\hat{\boldsymbol{n}}^l \times \frac{Z^n(\boldsymbol{H}_N^n - \boldsymbol{H}_N^l) - \hat{\boldsymbol{n}}^l\times(\boldsymbol{E}_N^n - \boldsymbol{E}_N^l)}{\bar{Z}}\Big)dS(\boldsymbol{r}),\end{aligned} \tag{4.27}$$

while the neighbor cell D_n has the following energy estimate:

$$\begin{aligned}\frac{\partial}{\partial t}E_{D_n} = \oint_{\partial D_n}\Big((\boldsymbol{H}_N^n \times \boldsymbol{E}_N^n)\cdot\hat{\boldsymbol{n}}^n \\ - \tau\boldsymbol{H}_N^n\cdot\hat{\boldsymbol{n}}^n \times \frac{Y^l(\boldsymbol{E}_N^l - \boldsymbol{E}_N^n) + \hat{\boldsymbol{n}}^n\times(\boldsymbol{H}_N^l - \boldsymbol{H}_N^n)}{\bar{Y}} \\ + \tau\boldsymbol{E}_N^n\cdot\hat{\boldsymbol{n}}^n \times \frac{Z^l(\boldsymbol{H}_N^l - \boldsymbol{H}_N^n) - \hat{\boldsymbol{n}}^n\times(\boldsymbol{E}_N^l - \boldsymbol{E}_N^n)}{\bar{Z}}\Big)dS(\boldsymbol{r}).\end{aligned} \tag{4.28}$$

Keeping in mind that $\hat{\boldsymbol{n}}^n = -\hat{\boldsymbol{n}}^l$, we can add the contributions to the integral over the common edge ∂D_c from element D_l and D_n and reach

$$\begin{aligned}\int_{\partial D_c}\Big((\boldsymbol{H}_N^l\times\boldsymbol{E}_N^l - \boldsymbol{H}_N^n\times\boldsymbol{E}_N^n)\cdot\hat{\boldsymbol{n}}^l \\ - \frac{\tau Y^n}{\bar{Y}}\boldsymbol{H}_N^l\cdot\hat{\boldsymbol{n}}^l\times\boldsymbol{E}_N^n + \frac{\tau Y^n}{\bar{Y}}\boldsymbol{H}_N^l\cdot\hat{\boldsymbol{n}}^l\times\boldsymbol{E}_N^l \\ + \frac{\tau Z^n}{\bar{Z}}\boldsymbol{E}_N^l\cdot\hat{\boldsymbol{n}}^l\times\boldsymbol{H}_N^n - \frac{\tau Z^n}{\bar{Z}}\boldsymbol{E}_N^l\cdot\hat{\boldsymbol{n}}^l\times\boldsymbol{H}_N^l \\ + \frac{\tau Y^l}{\bar{Y}}\boldsymbol{H}_N^n\cdot\hat{\boldsymbol{n}}^l\times\boldsymbol{E}_N^l - \frac{\tau Y^l}{\bar{Y}}\boldsymbol{H}_N^n\cdot\hat{\boldsymbol{n}}^l\times\boldsymbol{E}_N^n \\ - \frac{\tau Z^l}{\bar{Z}}\boldsymbol{E}_N^n\cdot\hat{\boldsymbol{n}}^l\times\boldsymbol{H}_N^l + \frac{\tau Z^l}{\bar{Z}}\boldsymbol{E}_N^n\cdot\hat{\boldsymbol{n}}^l\times\boldsymbol{H}_N^n \\ - \frac{\tau}{\bar{Y}}\boldsymbol{H}_N^l\cdot\hat{\boldsymbol{n}}^l\times\hat{\boldsymbol{n}}^l\times\boldsymbol{H}_N^n + \frac{\tau}{\bar{Y}}\boldsymbol{H}_N^l\cdot\hat{\boldsymbol{n}}^l\times\hat{\boldsymbol{n}}^l\times\boldsymbol{H}_N^l \\ - \frac{\tau}{\bar{Z}}\boldsymbol{E}_N^l\cdot\hat{\boldsymbol{n}}^l\times\hat{\boldsymbol{n}}^l\times\boldsymbol{E}_N^n + \frac{\tau}{\bar{Z}}\boldsymbol{E}_N^l\cdot\hat{\boldsymbol{n}}^l\times\hat{\boldsymbol{n}}^l\times\boldsymbol{E}_N^l \\ - \frac{\tau}{\bar{Y}}\boldsymbol{H}_N^n\cdot\hat{\boldsymbol{n}}^l\times\hat{\boldsymbol{n}}^l\times\boldsymbol{H}_N^l + \frac{\tau}{\bar{Y}}\boldsymbol{H}_N^n\cdot\hat{\boldsymbol{n}}^l\times\hat{\boldsymbol{n}}^l\times\boldsymbol{H}_N^n \\ - \frac{\tau}{\bar{Z}}\boldsymbol{E}_N^n\cdot\hat{\boldsymbol{n}}^l\times\hat{\boldsymbol{n}}^l\times\boldsymbol{E}_N^l + \frac{\tau}{\bar{Z}}\boldsymbol{E}_N^n\cdot\hat{\boldsymbol{n}}^l\times\hat{\boldsymbol{n}}^l\times\boldsymbol{E}_N^n\Big)dS(\boldsymbol{r}).\end{aligned} \tag{4.29}$$

Rearranged, (4.29) becomes

$$\begin{aligned}\int_{\partial D_c}\Big(\Big(&-1+\frac{\tau Y^n}{\bar{Y}}+\frac{\tau Z^n}{\bar{Z}}\Big)\boldsymbol{H}_N^l\cdot\hat{\boldsymbol{n}}^l\times\boldsymbol{E}_N^l\\&+\Big(1-\frac{\tau Y^l}{\bar{Y}}-\frac{\tau Z^l}{\bar{Z}}\Big)\boldsymbol{H}_N^n\cdot\hat{\boldsymbol{n}}^l\times\boldsymbol{E}_N^n\\&+(\frac{\tau Z^l}{\bar{Z}}-\frac{\tau Y^n}{\bar{Y}})\boldsymbol{H}_N^l\cdot\hat{\boldsymbol{n}}^l\times\boldsymbol{E}_N^n+(\frac{\tau Y^l}{\bar{Y}}-\frac{\tau Z^n}{\bar{Z}})\boldsymbol{H}_N^n\cdot\hat{\boldsymbol{n}}^l\times\boldsymbol{E}_N^l\\&+\frac{\tau}{\bar{Y}}\boldsymbol{H}_N^l\cdot\hat{\boldsymbol{n}}^l\times\hat{\boldsymbol{n}}^l\times\boldsymbol{H}_N^l+\frac{\tau}{\bar{Z}}\boldsymbol{E}_N^l\cdot\hat{\boldsymbol{n}}^l\times\hat{\boldsymbol{n}}^l\times\boldsymbol{E}_N^l\\&+\frac{\tau}{\bar{Z}}\boldsymbol{E}_N^n\cdot\hat{\boldsymbol{n}}^l\times\hat{\boldsymbol{n}}^l\times\boldsymbol{E}_N^n+\frac{\tau}{\bar{Y}}\boldsymbol{H}_N^n\cdot\hat{\boldsymbol{n}}^l\times\hat{\boldsymbol{n}}^l\times\boldsymbol{H}_N^n\\&-2\frac{\tau}{\bar{Z}}\boldsymbol{E}_N^n\cdot\hat{\boldsymbol{n}}^l\times\hat{\boldsymbol{n}}^l\times\boldsymbol{E}_N^l-2\frac{\tau}{\bar{Y}}\boldsymbol{H}_N^n\cdot\hat{\boldsymbol{n}}^l\times\hat{\boldsymbol{n}}^l\times\boldsymbol{H}_N^l\Big)dS(\boldsymbol{r}).\end{aligned}\tag{4.30}$$

Simplifying this using

$$\frac{Y^n}{\bar{Y}}+\frac{Z^n}{\bar{Z}}=\frac{\frac{1}{Z^n}}{\frac{1}{Z^n}+\frac{1}{Z^l}}+\frac{Z^n}{\bar{Z}}=\frac{Z^l}{\bar{Z}}+\frac{Z^n}{\bar{Z}}=1,\tag{4.31a}$$

$$\frac{Y^l}{\bar{Y}}+\frac{Z^l}{\bar{Z}}=\frac{\frac{1}{Z^l}}{\frac{1}{Z^n}+\frac{1}{Z^l}}+\frac{Z^l}{\bar{Z}}=\frac{Z^n}{\bar{Z}}+\frac{Z^l}{\bar{Z}}=1,\tag{4.31b}$$

$$\frac{Y^n}{\bar{Y}}-\frac{Z^l}{\bar{Z}}=\frac{\frac{1}{Z^n}}{\frac{1}{Z^n}+\frac{1}{Z^l}}-\frac{Z^l}{\bar{Z}}=\frac{Z^l}{\bar{Z}}-\frac{Z^l}{\bar{Z}}=0,\tag{4.31c}$$

$$\frac{Y^l}{\bar{Y}}-\frac{Z^n}{\bar{Z}}=\frac{\frac{1}{Z^l}}{\frac{1}{Z^n}+\frac{1}{Z^l}}-\frac{Z^n}{\bar{Z}}=\frac{Z^n}{\bar{Z}}-\frac{Z^n}{\bar{Z}}=0,\tag{4.31d}$$

yields

$$\begin{aligned}\int_{\partial D_c}\Big((\tau-1)\big(&\boldsymbol{H}_N^l\cdot\hat{\boldsymbol{n}}^l\times\boldsymbol{E}_N^l-\boldsymbol{H}_N^n\cdot\hat{\boldsymbol{n}}^l\times\boldsymbol{E}_N^n\big)\\&+\frac{\tau}{\bar{Y}}\boldsymbol{H}_N^l\cdot\hat{\boldsymbol{n}}^l\times\hat{\boldsymbol{n}}^l\times\boldsymbol{H}_N^l+\frac{\tau}{\bar{Z}}\boldsymbol{E}_N^l\cdot\hat{\boldsymbol{n}}^l\times\hat{\boldsymbol{n}}^l\times\boldsymbol{E}_N^l\\&+\frac{\tau}{\bar{Y}}\boldsymbol{H}_N^n\cdot\hat{\boldsymbol{n}}^l\times\hat{\boldsymbol{n}}^l\times\boldsymbol{H}_N^n+\frac{\tau}{\bar{Z}}\boldsymbol{E}_N^n\cdot\hat{\boldsymbol{n}}^l\times\hat{\boldsymbol{n}}^l\times\boldsymbol{E}_N^n\\&-2\frac{\tau}{\bar{Y}}\boldsymbol{H}_N^l\cdot\hat{\boldsymbol{n}}^l\times\hat{\boldsymbol{n}}^l\times\boldsymbol{H}_N^n-2\frac{\tau}{\bar{Z}}\boldsymbol{E}_N^l\cdot\hat{\boldsymbol{n}}^l\times\hat{\boldsymbol{n}}^l\times\boldsymbol{E}_N^n\Big)dS(\boldsymbol{r}).\end{aligned}\tag{4.32}$$

Representing this in a quadratic matrix form where R is the rotation matrix corresponding to the operation '$\hat{\boldsymbol{n}}^l\times$' in (4.19) we get

$$\begin{aligned}\int_{\partial D_c}\Big((\tau-1)&(\boldsymbol{H}_N^l)^TR\boldsymbol{E}_N^l-(\tau-1)(\boldsymbol{H}_N^n)^TR\boldsymbol{E}_N^n\\&+\frac{\tau}{\bar{Y}}(\boldsymbol{H}_N^l)^TR^2\boldsymbol{H}_N^l+\frac{\tau}{\bar{Z}}(\boldsymbol{E}_N^l)^TR^2\boldsymbol{E}_N^l\\&+\frac{\tau}{\bar{Y}}(\boldsymbol{H}_N^n)^TR^2\boldsymbol{H}_N^n+\frac{\tau}{\bar{Z}}(\boldsymbol{E}_N^n)^TR^2\boldsymbol{E}_N^n\\&-2\frac{\tau}{\bar{Y}}(\boldsymbol{H}_N^l)^TR^2\boldsymbol{H}_N^n-2\frac{\tau}{\bar{Z}}(\boldsymbol{E}_N^l)^TR^2\boldsymbol{E}_N^n\Big)dS(\boldsymbol{r}).\end{aligned}\tag{4.33}$$

If we can make sure that the contribution to the energy growth from the edge ∂D_c is not larger than 0, then we know, due to the prior analysis of the energy growth of the outer boundary faces, that there will be no energy growth in the multi-element system. This can be accomplished by requiring the integrand in (4.33) to be ≤ 0. In the same fashion as for the single element we express the integrand as $\boldsymbol{q}_N^T A \boldsymbol{q}_N$ where we have designed $\boldsymbol{q}_N$ as

$$\boldsymbol{q}_N = \begin{bmatrix} \boldsymbol{E}_N^n \\ \boldsymbol{E}_N^l \\ \boldsymbol{H}_N^n \\ \boldsymbol{H}_N^l \end{bmatrix} \tag{4.34}$$

which means that the matrix A becomes

$$A = \begin{bmatrix} \tau\bar{Z}^{-1}R^2 & -\tau\bar{Z}^{-1}R^2 & \frac{\tau-1}{2}R & 0 \\ -\tau\bar{Z}^{-1}R^2 & \tau\bar{Z}^{-1}R^2 & 0 & -\frac{\tau-1}{2}R \\ -\frac{\tau-1}{2}R & 0 & \tau\bar{Y}^{-1}R^2 & -\tau\bar{Y}^{-1}R^2 \\ 0 & \frac{\tau-1}{2}R & -\tau\bar{Y}^{-1}R^2 & \tau\bar{Y}^{-1}R^2 \end{bmatrix}. \tag{4.35}$$

A quadratic form can always be re-written like $\boldsymbol{q}_N^T A \boldsymbol{q}_N = \sum_i \lambda_i |\tilde{\boldsymbol{q}}_N|^2$, where λ_i are the eigenvalues to the matrix A. Here, the eigenvalues λ_i turn out to be

$$\lambda_{1-4} = 0, \tag{4.36a}$$

$$\lambda_{5-8} = \frac{1}{2\bar{Z}}\Big(-2\tau \pm \sqrt{4\tau^2 + \bar{Z}^2(\tau-1)^2}\Big), \tag{4.36b}$$

$$\lambda_{9-12} = \frac{1}{2\bar{Y}}\Big(-2\tau \pm \sqrt{4\tau^2 + \bar{Y}^2(\tau-1)^2}\Big). \tag{4.36c}$$

The only way we can make all the eigenvalues less than or equal to 0 is if

$$\tau = 1. \tag{4.37}$$

With this choice of τ, the quadratic form $\boldsymbol{q}_N^T A \boldsymbol{q}_N$ will be ≤ 0, which means that the contribution to $\frac{\partial}{\partial t}E$ from the common face ∂D_c is ≤ 0. We previously showed that the contributions to the energy growth from the outer boundaries are ≤ 0 if τ fulfills the requirements in (4.24). This interval takes different forms depending on the material properties at hand, but $\tau = 1$ always meets these conditions. This means that the spectral computational scheme is semi-discretely stable for the two-element system with $\tau = 1$. A larger computation consists of more elements with more boundary faces and shared faces, but the same reasoning holds. The total energy will still not grow and the scheme will remain stable.

Enough theoretical reasoning, let us look at some results from our calculations instead.

The error development for the spectral scheme that is displayed in Figure 4.15 is truly astonishing. The methods show no signs at all of error growth. They all seem to converge to a certain error level, around which there is a small amount of controlled fluctuation.

The transient course of events, i.e. the error development for the first units of time, is shown in Figure 4.16. Here it is clearer that methods of order 4, 6, 8 and

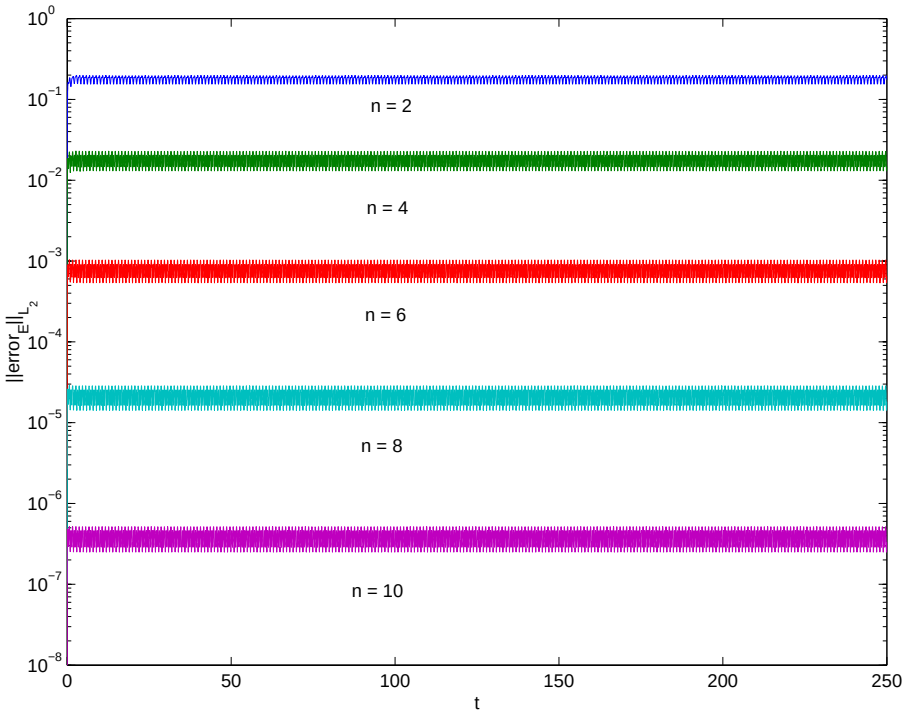

Figure 4.15. Development of the L_2-error of $\boldsymbol{E}$ during calculations to $t = 250$ for 2^{nd}, 4^{th}, 6^{th}, 8^{th} and 10^{th} order spectral element schemes with $\Delta x = 0.5$ and $\theta_i = \pi/3$.

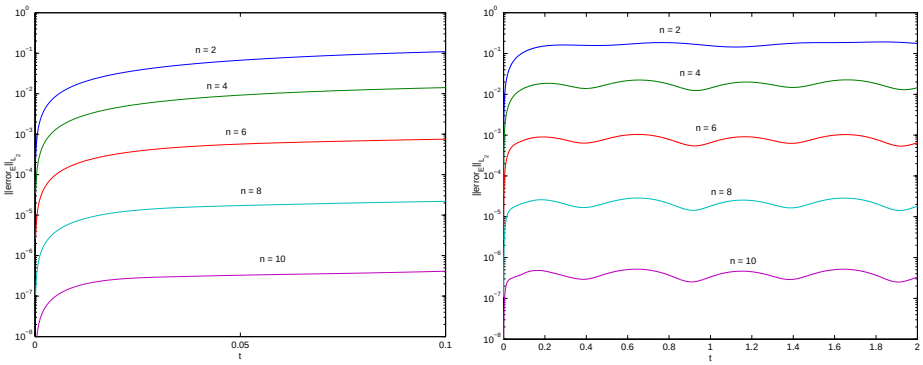

Figure 4.16. Development of the L_2-error of $\boldsymbol{E}$ during the early stages of the calculations for 2^{nd}, 4^{th}, 6^{th}, 8^{th} and 10^{th} order spectral element schemes with $\Delta x = 0.5$ and $\theta_i = \pi/3$.

10 have the same error fluctuation frequencies, in fact the frequency $2f$, when f is the frequency of the wave itself. Significant is that all orders converge to the maximum error level very quickly.

4.6.2 Finite Difference Scheme

Just as in the stability analysis of the spectral scheme, we construct an energy measure and see how this develops with time. If the total energy of the system does not increase with time, then the computational method is certainly stable.

The scheme for the finite difference method in equation (3.42) needs to be modified in order to handle the multiple materials we have in our problem. If we denote the solution in $x \leq 0$ $\boldsymbol{u}_l$ and likewise by $\boldsymbol{u}_r$ mean the solution in $x \geq 0$, then we

can introduce

$$\boldsymbol{w} = \begin{bmatrix} \boldsymbol{u}_l \\ \boldsymbol{u}_r \end{bmatrix}, \quad \tilde{S} = \begin{bmatrix} S_l & 0 \\ 0 & S_r \end{bmatrix}, \quad \tilde{A} = \begin{bmatrix} A & 0 \\ 0 & A \end{bmatrix}, \quad \tilde{B} = \begin{bmatrix} B & 0 \\ 0 & B \end{bmatrix}, \tag{4.38}$$

and in this notation the continuous problem becomes

$$\tilde{S}\boldsymbol{w}_t + \tilde{A}\boldsymbol{w}_x + \tilde{B}\boldsymbol{w}_y = 0. \tag{4.39}$$

We observe that by taking

$$\|\boldsymbol{w}\|^2 \equiv \int_\Omega \boldsymbol{w}^T \tilde{S}\boldsymbol{w} dxdy \tag{4.40}$$

we automatically get the electromagnetic energy, apart from a factor 2,

$$\|\boldsymbol{w}\|^2 = 2\int_\Omega (\rho_{\boldsymbol{E}} + \rho_{\boldsymbol{H}}) dxdy, \tag{4.41}$$

where $\rho_{\boldsymbol{E}}(\boldsymbol{r}) = \frac{1}{2}\epsilon(\boldsymbol{r})\Big|\boldsymbol{E}(\boldsymbol{r})\Big|^2$ and $\rho_{\boldsymbol{H}}(\boldsymbol{r}) = \frac{1}{2}\mu(\boldsymbol{r})\Big|\boldsymbol{H}(\boldsymbol{r})\Big|^2$.

If we multiply (4.39) by $\boldsymbol{w}$ from the left and integrate over the entire computational area Ω we eventually get

$$\begin{aligned} \frac{d}{dt}\|\boldsymbol{w}\|^2 = &- 2\int_0^1 H_z E_y dy\Big|_{x=1} + 2\int_0^1 H_z E_y dy\Big|_{x=-1} \\ &+ 2\int_{-1}^1 H_z E_x dx\Big|_{y=1} - 2\int_{-1}^1 H_z E_x dx\Big|_{y=0}. \end{aligned} \tag{4.42}$$

Using the results of (3.46) - (3.49) where we have chosen $a_i = 1$, we can express the energy norm in terms of characteristic variables which will come in handy as we will see shortly.

$$\begin{aligned} \frac{d}{dt}\|\boldsymbol{w}\|^2 = &- 2\int_0^1 \frac{1}{\eta}\Big((c_1^x)^2 - (c_3^x)^2\Big) dy\Big|_{x=1} + 2\int_0^1 \frac{1}{\eta}\Big((c_3^x)^2 - (c_1^x)^2\Big) dy\Big|_{x=-1} \\ &+ 2\int_0^1 \frac{1}{\eta}\Big((c_3^y)^2 - (c_1^y)^2\Big) dx\Big|_{y=1} - 2\int_{-1}^1 \frac{1}{\eta}\Big((c_1^y)^2 - (c_3^y)^2\Big) dx\Big|_{y=0}. \end{aligned} \tag{4.43}$$

Now, as we leave the continuous formulation and switch to the discrete numerical approximation, our multi-material problem formulation becomes in the language of block matrices

$$\begin{aligned} \begin{bmatrix} BC_l + IT_l \\ BC_r + IT_r \end{bmatrix} = &\begin{bmatrix} I_{N_l} \otimes I_M \otimes S_l & 0 \\ 0 & I_{N_r} \otimes I_M \otimes S_r \end{bmatrix} \boldsymbol{w}_t \\ &+ \begin{bmatrix} P_{xl}^{-1}Q_{xl} \otimes I_M \otimes A & 0 \\ 0 & P_{xr}^{-1}Q_{xr} \otimes I_M \otimes A \end{bmatrix} \boldsymbol{w} \\ &+ \begin{bmatrix} I_{N_l} \otimes P_y^{-1}Q_y \otimes B & 0 \\ 0 & I_{N_r} \otimes P_y^{-1}Q_y \otimes B \end{bmatrix} \boldsymbol{w}, \end{aligned} \tag{4.44}$$

where $\boldsymbol{w} = [\boldsymbol{u}_l\, \boldsymbol{u}_r]^T$ is the numerical solution in the discrete nodes and $\boldsymbol{u}_l$, $\boldsymbol{u}_r$, S_l, S_r, A and B are according to equations (3.37) - (3.39). I_a is an identity matrix

of size $(a+1)\times(a+1)$ and $P_x^{-1}Q_x$ and $P_y^{-1}Q_y$ are the summation by parts differentiation matrices. BC_l and BC_r are the SAT boundary terms as given by

$$\begin{aligned} BC_l = \quad & (P_{xl}^{-1}E_{0N_l}\otimes I_M\otimes\Sigma_{west}) \\ & \Big((I_{N_l}\otimes I_M\otimes K_{west})\boldsymbol{u_l} - \boldsymbol{e}_{0N_l}\otimes\boldsymbol{g}_{west}\Big) \\ & + (I_{N_l}\otimes P_y^{-1}E_{0M}\otimes\Sigma_{south_l}) \\ & \Big((I_{N_l}\otimes I_M\otimes K_{south_l})\boldsymbol{u}_l - \boldsymbol{g}_{south_l}\otimes\boldsymbol{e}_{0M}\Big) \\ & + (I_{N_l}\otimes P_y^{-1}E_{MM}\otimes\Sigma_{north_l}) \\ & \Big((I_{N_l}\otimes I_M\otimes K_{north_l})\boldsymbol{u}_l - \boldsymbol{g}_{north_l}\otimes\boldsymbol{e}_{MM}\Big), \end{aligned} \tag{4.45}$$

$$\begin{aligned} BC_r = \quad & (P_{xr}^{-1}E_{N_rN_r}\otimes I_M\otimes\Sigma_{east}) \\ & \Big((I_{N_r}\otimes I_M\otimes K_{east})\boldsymbol{u}_r - \boldsymbol{e}_{N_rN_r}\otimes\boldsymbol{g}_{east}\Big) \\ & + (I_{N_r}\otimes P_y^{-1}E_{0M}\otimes\Sigma_{south_r}) \\ & \Big((I_{N_r}\otimes I_M\otimes K_{south_r})\boldsymbol{u}_r - \boldsymbol{g}_{south_r}\otimes\boldsymbol{e}_{0M}\Big) \\ & + (I_{N_r}\otimes P_y^{-1}E_{MM}\otimes\Sigma_{north}) \\ & \Big((I_{N_r}\otimes I_M\otimes K_{north_r})\boldsymbol{u}_r - \boldsymbol{g}_{north_r}\otimes\boldsymbol{e}_{MM}\Big), \end{aligned} \tag{4.46}$$

with P_x and P_y as above and E_{ab} and $\boldsymbol{e}_{ab}$ according to (3.44) and (3.45). The transformation matrices K to characteristic variables are given by (3.51) and (3.51b) whereas the exact boundary data $\boldsymbol{g}$ of the characteristic variables come from (3.52), (3.53) and (3.54). The Σ's are the boundary penalty matrices to be determined.

The part of the scheme that takes special care of the interface between the two materials is

$$IT_l = (P_{xl}^{-1}E_{N_lN_l}\otimes I_M\otimes\Sigma_{x=0l})\Big(\boldsymbol{e}_{N_lN_l}\otimes(I_M\otimes\Gamma)(\boldsymbol{u}_{lN_l}-\boldsymbol{u}_{r0})\Big) \tag{4.47a}$$

$$IT_r = (P_{xr}^{-1}E_{0N_r}\otimes I_M\otimes\Sigma_{x=0r})\Big(\boldsymbol{e}_{0N_r}\otimes(I_M\otimes\Gamma)(\boldsymbol{u}_{r0}-\boldsymbol{u}_{lN_l})\Big). \tag{4.47b}$$

Here, the vectors and matrices P_x, P_y, I_M, E_{ab}, and e_{ab} are as above. The continuity of the tangential fields over the interface is established through the matrix Γ that provides the following:

$$\Gamma\tilde{\boldsymbol{u}}_l(0,y_j) = \Gamma\tilde{\boldsymbol{u}}_r(0,y_j), \quad \Gamma = \begin{bmatrix} 1 & 0 & 0 \\ 0 & 0 & 0 \\ 0 & 0 & 1 \end{bmatrix}. \tag{4.48}$$

The nodes that this interface term acts on are given by

$$\boldsymbol{u}_{r0} = \begin{bmatrix} \tilde{\boldsymbol{u}}_{\boldsymbol{r}0,0} \\ \tilde{\boldsymbol{u}}_{\boldsymbol{r}0,1} \\ \vdots \\ \tilde{\boldsymbol{u}}_{\boldsymbol{r}0,M} \end{bmatrix}, \quad \boldsymbol{u}_{lN_l} = \begin{bmatrix} \tilde{\boldsymbol{u}}_{\boldsymbol{l}N_l,0} \\ \tilde{\boldsymbol{u}}_{\boldsymbol{l}N_l,1} \\ \vdots \\ \tilde{\boldsymbol{u}}_{\boldsymbol{l}N_l,M} \end{bmatrix}. \tag{4.49}$$

Finally, we have introduced the 3×3 interface penalty matrices $\Sigma_{x=0l}$ and $\Sigma_{x=0r}$. These have to be chosen suitably in order to yield a stable numerical scheme.

To simplify further analysis, we multiply equation (4.44) from the right with

$$\begin{bmatrix} P_{xl} \otimes P_y \otimes I_3 & 0 \\ 0 & P_{xr} \otimes P_y \otimes I_3 \end{bmatrix}, \tag{4.50}$$

which yields

$$P\boldsymbol{w}_t + (Q_x + \Sigma_{int})\boldsymbol{w} + Q_y\boldsymbol{w} = BC \tag{4.51}$$

where $\boldsymbol{w} = [\boldsymbol{u}_l\, \boldsymbol{u}_r]$,

$$P = \begin{bmatrix} (P_{xl} \otimes P_y \otimes I_3)S_l & 0 \\ 0 & (P_{xr} \otimes P_y \otimes I_3)S_r \end{bmatrix}, \tag{4.52a}$$

$$Q_x = \begin{bmatrix} Q_{xl} \otimes P_y \otimes A & 0 \\ 0 & Q_{xr} \otimes P_y \otimes A \end{bmatrix}, \tag{4.52b}$$

$$Q_y = \begin{bmatrix} P_{xl} \otimes Q_y \otimes B & 0 \\ 0 & P_{xr} \otimes Q_y \otimes B \end{bmatrix}, \tag{4.52c}$$

$$\Sigma_{int} = \begin{bmatrix} 0 & \cdots & & & \cdots & 0 \\ \vdots & \ddots & & & \cdots & 0 \\ & & -P_y \otimes \Sigma_{x=0l} & P_y \otimes \Sigma_{x=0l} & & \\ & & P_y \otimes \Sigma_{x=0r} & -P_y \otimes \Sigma_{x=0r} & & \\ \vdots & & & & \ddots & \vdots \\ 0 & \cdots & & & \cdots & 0 \end{bmatrix}, \tag{4.52d}$$

and the boundary terms

$$\begin{aligned} BC = {} & (E_l \otimes E_{0N_l} \otimes P_y \otimes \Sigma_w) \\ & \Big((E_l \otimes E_{0N_l} \otimes I_M \otimes K_w)\boldsymbol{w} - \boldsymbol{e}_l \otimes \boldsymbol{e}_{0N_l} \otimes \boldsymbol{g}_w\Big) \\ & + (E_l \otimes P_{xl} \otimes E_{0M} \otimes \Sigma_{s_l}) \\ & \Big((E_l \otimes I_{N_l} \otimes E_{0M} \otimes K_{s_l})\boldsymbol{w} - \boldsymbol{e}_l \otimes \boldsymbol{g}_{s_l} \otimes \boldsymbol{e}_{0M}\Big) \\ & + (E_l \otimes P_{xl} \otimes E_{MM} \otimes \Sigma_{n_l}) \\ & \Big((E_l \otimes I_{N_l} \otimes E_{MM} \otimes K_{n_l})\boldsymbol{w} - \boldsymbol{e}_l \otimes \boldsymbol{g}_{n_l} \otimes \boldsymbol{e}_{MM}\Big) \\ & + (E_r \otimes P_{xr} \otimes E_{0M} \otimes \Sigma_{s_r}) \\ & \Big((E_r \otimes I_{N_r} \otimes E_{0M} \otimes K_{s_r})\boldsymbol{w} - \boldsymbol{e}_r \otimes \boldsymbol{g}_{s_r} \otimes \boldsymbol{e}_{0M}\Big) \\ & + (E_r \otimes P_{xr} \otimes E_{MM} \otimes \Sigma_{n_r}) \\ & \Big((E_r \otimes I_{N_r} \otimes E_{MM} \otimes K_{n_r})\boldsymbol{w} - \boldsymbol{e}_r \otimes \boldsymbol{g}_{n_r} \otimes \boldsymbol{e}_{MM}\Big) \\ & + (E_r \otimes E_{N_rN_r} \otimes P_y \otimes \Sigma_e) \\ & \Big((E_r \otimes E_{N_rN_r} \otimes I_M \otimes K_e)\boldsymbol{w} - \boldsymbol{e}_r \otimes \boldsymbol{e}_{N_rN_r} \otimes \boldsymbol{g}_e\Big). \end{aligned} \tag{4.53}$$

In (4.52d) we have introduced the scaling

$$\Sigma_{x=0l} = \Sigma_{x=0l}\Gamma, \quad \Sigma_{x=0r} = \Sigma_{x=0r}\Gamma, \tag{4.54}$$

and in expressions (4.52) - (4.52d) above, we have also used the block matrix notation. In Σ_{int} in particular, the only non-zero elements are the ones in the

center of the matrix coupling the left and right regions to each other. In the term (4.53) originating from the boundary conditions, we have abbreviated

$$\begin{array}{ccc} \boldsymbol{g}_w = \boldsymbol{g}_{west}, & \boldsymbol{g}_{s_l} = \boldsymbol{g}_{south_l}, & \boldsymbol{g}_{n_l} = \boldsymbol{g}_{north_l}, \\ \boldsymbol{\Sigma}_w = \boldsymbol{\Sigma}_{west}, & \boldsymbol{\Sigma}_{s_l} = \boldsymbol{\Sigma}_{south_l}, & \boldsymbol{\Sigma}_{n_l} = \boldsymbol{\Sigma}_{north_l}, \\ \boldsymbol{g}_{s_r} = \boldsymbol{g}_{south_r}, & \boldsymbol{g}_{n_r} = \boldsymbol{g}_{north_r}, & \boldsymbol{g}_e = \boldsymbol{g}_{east}, \\ \boldsymbol{\Sigma}_{s_r} = \boldsymbol{\Sigma}_{south_r}, & \boldsymbol{\Sigma}_{n_r} = \boldsymbol{\Sigma}_{north_r}, & \boldsymbol{\Sigma}_e = \boldsymbol{\Sigma}_{east}, \end{array} \tag{4.55}$$

and we use the matrices and vectors

$$E_l = \begin{bmatrix} 1 & 0 \\ 0 & 0 \end{bmatrix}, \quad E_r = \begin{bmatrix} 0 & 0 \\ 0 & 1 \end{bmatrix}, \quad \boldsymbol{e}_l = \begin{bmatrix} 1 \\ 0 \end{bmatrix}, \quad \boldsymbol{e}_r = \begin{bmatrix} 0 \\ 1 \end{bmatrix}, \tag{4.56}$$

to pick out if the boundary belongs to the left or the right region. Written in this form, we have assumed the number of grid points in the left and right regions to be equal, i.e. $N_l = N_r$.

To check the stability of (4.51), we will use the energy method and it is convenient to use a norm that looks like the one in (4.40), only with the difference that we here discuss the discrete problem. In (4.40), $\boldsymbol{w}$ denoted the field variables at an arbitrary coordinate (x, y), but here $\boldsymbol{w}$ takes the meaning of the field values at all discrete points (x_i, y_j). Because of this, we can remove the integral from the norm. We define

$$\|\boldsymbol{w}\|_P^2 \equiv \boldsymbol{w}^T P \boldsymbol{w} \tag{4.57}$$

and we make the following observation about the power T:

$$T = \frac{d}{dt}\|\boldsymbol{w}\|_P^2 = \boldsymbol{w}^T P \boldsymbol{w}_t + \boldsymbol{w}_t^T P^T \boldsymbol{w}, \tag{4.58}$$

since P_{xl}, P_{xr},P_y, S_l and S_l are all symmetric which means that P is also symmetric.

If we multiply equation (4.51) from the right by $\boldsymbol{w}^T$ and to that add the transposed resulting equation, aided by the help of observation (4.58) above, we reach

$$\begin{aligned} \frac{d}{dt}\|\boldsymbol{w}\|_P^2 = \boldsymbol{w}^T BC + (\boldsymbol{w}^T BC)^T - \boldsymbol{w}^T (Q_x + \Sigma_{int} + Q_y)\boldsymbol{w} \\ - (\boldsymbol{w}^T (Q_x + \Sigma_{int} + Q_y)\boldsymbol{w})^T. \end{aligned} \tag{4.59}$$

The fact that P_{xl}, P_{xr}, P_y, Q_{xl}, Q_{xr} and Q_y are summation by parts operators forces them to have the following properties:

$$P_{xl} = P_{xl}^T, \quad P_{xr} = P_{xr}^T, \quad P_y = P_y^T, \tag{4.60}$$

$$Q_{xl} + Q_{xl}^T = -E_{0N_l} + E_{N_l N_l}, \tag{4.61a}$$

$$Q_{xr} + Q_{xr}^T = -E_{0N_r} + E_{N_r N_r}, \tag{4.61b}$$

$$Q_y + Q_y^T = -E_{0M} + E_{MM}, \tag{4.61c}$$

with E_{0k} and E_{kk} as in (3.44). This makes some of the terms in (4.59) really simple, e.g.

$$\begin{aligned} \boldsymbol{w}^T (Q_x + Q_y)\boldsymbol{w} + (w^T (Q_x + Q_y)\boldsymbol{w})^T = \\ = - \boldsymbol{v}_{l0}^T (P_{xl} \otimes B)\boldsymbol{v}_{l0} + \boldsymbol{v}_{lM}^T (P_{xl} \otimes B)\boldsymbol{v}_{lM} - \boldsymbol{v}_{r0}^T (P_{xl} \otimes B)\boldsymbol{v}_{r0} \\ + \boldsymbol{v}_{rM}^T (P_{xl} \otimes B)\boldsymbol{v}_{rM} - \boldsymbol{u}_{l0}^T (P_y \otimes A)\boldsymbol{u}_{l0} + \boldsymbol{u}_{rN_r}^T (P_y \otimes A)\boldsymbol{u}_{rN_r} \\ + \boldsymbol{u}_{lN_l}^T (P_y \otimes A)\boldsymbol{u}_{lN_l} - \boldsymbol{u}_{r0}^T (P_y \otimes A)\boldsymbol{u}_{r0}. \end{aligned} \tag{4.62}$$

In (4.62) and in the following equations we use the row and column notation given in (3.39) and (3.40), i.e. $\boldsymbol{u}_{li}$ denotes a column of M gridpoints located at x_i in the left region while $\boldsymbol{v}_{rj}$ denotes a row of N_r gridpoints located at y_j in the domain on the right. We can see in (4.62) that the only values that matter in the energy measure are those at the boundaries of the computational region as well as on the material interface.

The term in (4.59) pertaining to the interface conditions becomes

$$\begin{aligned}
\boldsymbol{w}^T\Sigma_{int}\boldsymbol{w} + (w^T\Sigma_{int}\boldsymbol{w})^T = \\
= \quad & \boldsymbol{u}_{lN_l}^T\Big(P_y \otimes (-\Sigma_{x=0l} - \Sigma_{x=0l}^T)\Big)\boldsymbol{u}_{lN_l} \\
& + \boldsymbol{u}_{r0}^T\Big(P_y \otimes (-\Sigma_{x=0r} - \Sigma_{x=0r}^T)\Big)\boldsymbol{u}_{r0} \\
& + \boldsymbol{u}_{lN_l}^T\Big(P_y \otimes (\Sigma_{x=0l} + \Sigma_{x=0r}^T)\Big)\boldsymbol{u}_{r0} \\
& + \boldsymbol{u}_{r0}^T\Big(P_y \otimes (\Sigma_{x=0l}^T + \Sigma_{x=0r})\Big)\boldsymbol{u}_{lN_l}.
\end{aligned} \tag{4.63}$$

Finally, the term with the boundary conditions becomes

$$\begin{aligned}
\boldsymbol{w}^T BC + (\boldsymbol{w}^T BC)^T = \quad & \boldsymbol{v}_{l0}^T\Big(P_{xl} \otimes \big(\Sigma_{s_l}K_{s_l} + (\Sigma_{s_l}K_{s_l})^T\big)\Big)\boldsymbol{v}_{l0} \\
& + \boldsymbol{v}_{lM}^T\Big(P_{xl} \otimes \big(\Sigma_{n_l}K_{n_l} + (\Sigma_{n_l}K_{n_l})^T\big)\Big)\boldsymbol{v}_{lM} \\
& + \boldsymbol{v}_{r0}^T\Big(P_{xl} \otimes \big(\Sigma_{s_r}K_{s_r} + (\Sigma_{s_r}K_{s_r})^T\big)\Big)\boldsymbol{v}_{r0} \\
& + \boldsymbol{v}_{rM}^T\Big(P_{xl} \otimes \big(\Sigma_{n_r}K_{n_r} + (\Sigma_{n_r}K_{n_r})^T\big)\Big)\boldsymbol{v}_{rM} \\
& + \boldsymbol{u}_{l0}^T\Big(P_y \otimes \big(\Sigma_w K_w + (\Sigma_w K_w)^T\big)\Big)\boldsymbol{u}_{l0} \\
& + \boldsymbol{u}_{rN_r}^T\Big(P_y \otimes \big(\Sigma_e K_e + (\Sigma_e K_e)^T\big)\Big)\boldsymbol{u}_{rN_r} \\
& - 2\boldsymbol{u}_{l0}^T\Big(P_y \otimes \Sigma_w\Big)\boldsymbol{g}_w - 2\boldsymbol{u}_{rN_r}^T\Big(P_y \otimes \Sigma_e\Big)\boldsymbol{g}_e \\
& - 2\boldsymbol{v}_{l0}^T\Big(P_{xl} \otimes \Sigma_{s_l}\Big)\boldsymbol{g}_{s_l} - 2\boldsymbol{v}_{lM}^T\Big(P_{xl} \otimes \Sigma_{n_l}\Big)\boldsymbol{g}_{n_l} \\
& - 2\boldsymbol{v}_{r0}^T\Big(P_{xr} \otimes \Sigma_{s_r}\Big)\boldsymbol{g}_{s_r} - 2\boldsymbol{v}_{rM}^T\Big(P_{xr} \otimes \Sigma_{n_r}\Big)\boldsymbol{g}_{n_r}
\end{aligned} \tag{4.64}$$

Now comes the work of collecting the terms from (4.62), (4.63) and (4.64) and putting them into (4.59). The purpose is to find choices of the Σ so that $\frac{d}{dt}\|\boldsymbol{w}\|_P^2 \leq 0$, in which case we know that the electromagnetic energy of the problem will not grow with time, i.e. we have a stable method. First, we deal with the terms that arise from and at the material interface. We have

$$\begin{aligned}
T_{int} = \quad & \boldsymbol{u}_{lN_l}^T\Big(P_y \otimes (-A + \Sigma_{x=0l} + \Sigma_{x=0l}^T)\Big)\boldsymbol{u}_{lN_l} \\
& + \boldsymbol{u}_{r0}^T\Big(P_y \otimes (A + \Sigma_{x=0r} + \Sigma_{x=0r}^T)\Big)\boldsymbol{u}_{r0} \\
& - \boldsymbol{u}_{lN_l}^T\Big(P_y \otimes (\Sigma_{x=0l} + \Sigma_{x=0r}^T)\Big)\boldsymbol{u}_{r0} \\
& - \boldsymbol{u}_{r0}^T\Big(P_y \otimes (\Sigma_{x=0l}^T + \Sigma_{x=0r})\Big)\boldsymbol{u}_{lN_l} \equiv \\
\equiv \quad & \boldsymbol{w}_{int}^T\tilde{D}\boldsymbol{w}_{int},
\end{aligned} \tag{4.65}$$

where $\boldsymbol{w}_{int}^T = [u_{lN_l}^T u_{r0}^T]$ and

$$\tilde{D} = \begin{bmatrix} P_y \otimes (-A + \Sigma_{x=0l} + \Sigma_{x=0l}^T) & P_y \otimes (-\Sigma_{x=0l} - \Sigma_{x=0r}^T) \\ P_y \otimes (-\Sigma_{x=0l}^T - \Sigma_{x=0r}) & P_y \otimes (A + \Sigma_{x=0r} + \Sigma_{x=0r}^T) \end{bmatrix}. \quad (4.66)$$

It is sufficient to find a $\tilde{D}$ that is negative semidefinite in order to obtain stability at the inner material interface. To do this, we have the freedom to choose our penalty matrices $\Sigma_{x=0l}$, $\Sigma_{x=0r}$ as we desire. It is suitable to require $\Sigma_{x=0l}$ and $\Sigma_{x=0r}$ to be symmetric, and to let $\Sigma_{x=0r} = \Sigma_{x=0l} - A$ which preserves the conservative character of the method (see [4]). This yields

$$\Sigma_{x=0l} = \begin{bmatrix} \lambda_1 & 0 & \frac{1}{2} \\ 0 & 0 & 0 \\ \frac{1}{2} & 0 & \lambda_2 \end{bmatrix}, \quad \Sigma_{x=0r} = \begin{bmatrix} \lambda_1 & 0 & -\frac{1}{2} \\ 0 & 0 & 0 \\ -\frac{1}{2} & 0 & \lambda_2 \end{bmatrix}. \quad (4.67)$$

These simplifications amount to

$$\tilde{D} = \begin{bmatrix} -1 & 1 \\ 1 & -1 \end{bmatrix} \otimes P_y \otimes (A - 2\Sigma_{x=0l}). \quad (4.68)$$

$\begin{bmatrix} -1 & 1 \\ 1 & -1 \end{bmatrix}$ is negative semidefinite, and P_y is by definition positive definite.

This along with the properties of Kronecker matrix multiplication implies that $(A - 2\Sigma_{x=0l})$ must be chosen such that it is positive semidefinite in order to make $\tilde{D}$ negative semidefinite. But

$$A - 2\Sigma_{x=0l} = \begin{bmatrix} -2\lambda_1 & 0 & 0 \\ 0 & 0 & 0 \\ 0 & 0 & -2\lambda_2 \end{bmatrix}, \quad (4.69)$$

and hence, all we have to do to ensure a stable method over the interface is to choose λ_1, $\lambda_2 \leq 0$. For the actual numerical calculations, we have used $\lambda_1 = \lambda_2 = \frac{-1}{2}$.

This means that we have chosen our penalty parameters $\Sigma_{x=0l}$ and $\Sigma_{x=0r}$ for the interface terms in (4.59). We now concentrate on the terms from the outer boundaries, and to start out, we examine the contribution from the western side. We have

$$\begin{aligned} T_{west} = \quad & \boldsymbol{u}_{l0}^T \Big(P_y \otimes \big(A + \Sigma_w K_w + (\Sigma_w K_w)^T \big) \Big) \boldsymbol{u}_{l0} \\ & - 2\boldsymbol{u}_{l0}^T \Big(P_y \otimes \Sigma_w \Big) \boldsymbol{g}_w, \end{aligned} \quad (4.70)$$

which is to compare with the western contribution from the continuous energy estimate in equation (4.43),

$$T_{west} = 2 \int_0^1 \frac{1}{\eta} \Big((c_3^x)^2 - (c_1^x)^2 \Big) dy \Big|_{x=-1}. \quad (4.71)$$

Ideally, we would like the discrete energy measure to mimic the continuous as closely as possible. We can try to re-write (4.70) expressed in characteristic variables so that it resembles (4.71). As discussed in Appendix B, on the western

border, the boundary data is the ingoing characteristic variable, $c_3^x(x=-1,y_j)$. It suffices to look at homogeneous boundary conditions, i.e. $c_3^x = 0$, which means that (4.71) turns into

$$T_{west} = -2\int_0^1 \frac{1}{\eta}(c_1^x)^2 dy\Big|_{x=-1}, \tag{4.72}$$

and (4.70) into

$$T_{west} = \boldsymbol{u}_{l0}^T\Big(P_y \otimes \big(A + \Sigma_w K_w + (\Sigma_w K_w)^T\big)\Big)\boldsymbol{u}_{l0}, \tag{4.73}$$

if we choose Σ_w to pick out only the c_3 components of $\boldsymbol{g}_w$, i.e.

$$\Sigma_w = \begin{bmatrix} 0 & 0 & \Sigma_{02} \\ 0 & 0 & \Sigma_{12} \\ 0 & 0 & \Sigma_{22} \end{bmatrix}. \tag{4.74}$$

In (4.72), we see that the continuous energy estimate is dissipative. This is something we would like to hold for the discrete energy estimate as well. The goal is hence to choose Σ_w in such a way that it reformulates (4.73) to the same form as (4.72). The integral in the continuous energy estimate corresponds to the summation carried out by multiplication by P_y is in the discrete case, so what remains is to re-write (4.73) with the characteristic variables. We observe that

$$\tilde{\boldsymbol{u}}_{0,j}^T (E_{02}K_w)^T E_{02}K_w \tilde{\boldsymbol{u}}_{0,j} = (c_1^x)^2, \tag{4.75}$$

where

$$E_{02} = \begin{bmatrix} 1 & 0 & 0 \\ 0 & 0 & 0 \\ 0 & 0 & 0 \end{bmatrix}, \tag{4.76}$$

which leads us to the form

$$\begin{aligned}\frac{d}{dt}\|\boldsymbol{w}\|_{P_{west}}^2 = \boldsymbol{u}_{l0}^T\Big(P_y \otimes \big(&-\frac{2}{\eta}(E_{02}K_w)^T E_{02}K_w + \frac{2}{\eta}(E_{02}K_w)^T E_{02}K_w \\ &+ A + \Sigma_w K_w + (\Sigma_w K_w)^T\big)\Big)\boldsymbol{u}_{l0}.\end{aligned} \tag{4.77}$$

(4.77) will match (4.72) if we can choose

$$\frac{2}{\eta}(E_{02}K_w)^T E_{02}K_w + A + \Sigma_w K_w + (\Sigma_w K_w)^T = 0. \tag{4.78}$$

With the assumption that Σ_w has the appearance of (4.74), this condition leads to the following overspecified system:

$$-2\Sigma_{02} = 1 \tag{4.79a}$$
$$-\Sigma_{12}\eta = 0 \tag{4.79b}$$
$$-\Sigma_{02} - \Sigma_{22}\eta = 1 \tag{4.79c}$$
$$-2\Sigma_{22} = \frac{1}{\eta}, \tag{4.79d}$$

which is consistently solved by $\Sigma_{02} = -\frac{1}{2}$, $\Sigma_{12} = 0$ and $\Sigma_{22} = -\frac{1}{2\eta}$. With this choice of Σ_w we have forced the discrete method to have the equivalent amount of dissipation as the continuous case has at the western border. Repeating this procedure, we can deduce the rest of the penalty matrices Σ_e, Σ_{n_l}, Σ_{n_r}, Σ_{s_l}, Σ_{s_r}, and make sure that the method is stable by the dissipation condition on the boundaries. The result becomes

$$\Sigma_{n_l} = \begin{bmatrix} 0 & 0 & -\frac{1}{2} \\ 0 & 0 & -\frac{1}{2\eta_l} \\ 0 & 0 & 0 \end{bmatrix}, \quad \Sigma_{n_r} = \begin{bmatrix} 0 & 0 & -\frac{1}{2} \\ 0 & 0 & -\frac{1}{2\eta_r} \\ 0 & 0 & 0 \end{bmatrix}, \tag{4.80}$$

$$\Sigma_{s_l} = \begin{bmatrix} 0 & 0 & \frac{1}{2} \\ 0 & 0 & -\frac{1}{2\eta_l} \\ 0 & 0 & 0 \end{bmatrix}, \quad \Sigma_{s_r} = \begin{bmatrix} 0 & 0 & \frac{1}{2} \\ 0 & 0 & -\frac{1}{2\eta_r} \\ 0 & 0 & 0 \end{bmatrix}, \tag{4.81}$$

$$\Sigma_e = \begin{bmatrix} 0 & 0 & \frac{1}{2} \\ 0 & 0 & 0 \\ 0 & 0 & -\frac{1}{2\eta_r} \end{bmatrix}, \quad \Sigma_w = \begin{bmatrix} 0 & 0 & -\frac{1}{2} \\ 0 & 0 & 0 \\ 0 & 0 & -\frac{1}{2\eta_l} \end{bmatrix}. \tag{4.82}$$

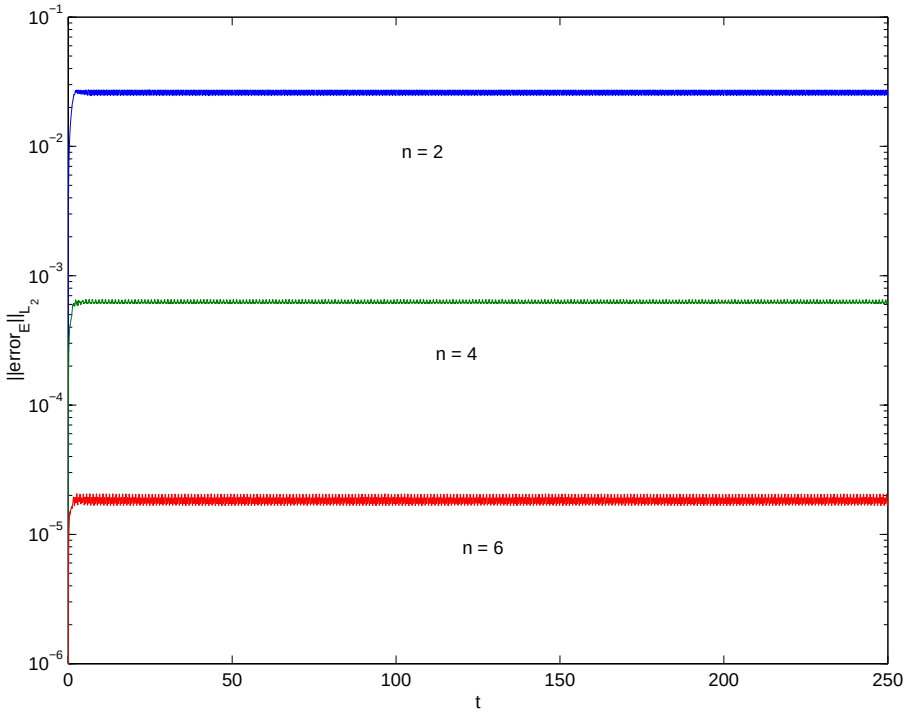

Figure 4.17. Development of the L_2-error of $\boldsymbol{E}$ during calculations to $t = 250$ for 2^{nd}, 4^{th} and 6^{th} order finite difference schemes at $\theta_i = \frac{\pi}{3}$ with $\Delta x = 0.025$.

Now we have (4.59) in the form

$$\begin{aligned} T = \frac{d}{dt}\|\boldsymbol{w}\|_P^2 = \quad & T_{int} + T_{west} + T_{east} \\ & + T_{south_l} + T_{south_r} + T_{north_l} + T_{north_r}, \end{aligned} \tag{4.83}$$

where all the terms T_i are ≤ 0. To summarize,

$$T = \frac{d}{dt}\|\boldsymbol{w}\|_P^2 \leq 0, \tag{4.84}$$

i.e. the finite difference method is stable.

In Figure 4.17 are the $\boldsymbol{E}$-errors with respect to time when we let the calculation traverse to $t = 250$. These calculations were performed on a grid with spacing $\Delta x = 0.025$. Clearly, all the methods show an error that is very stable in time, very much like the error development in the spectral methods in Figure 4.15.

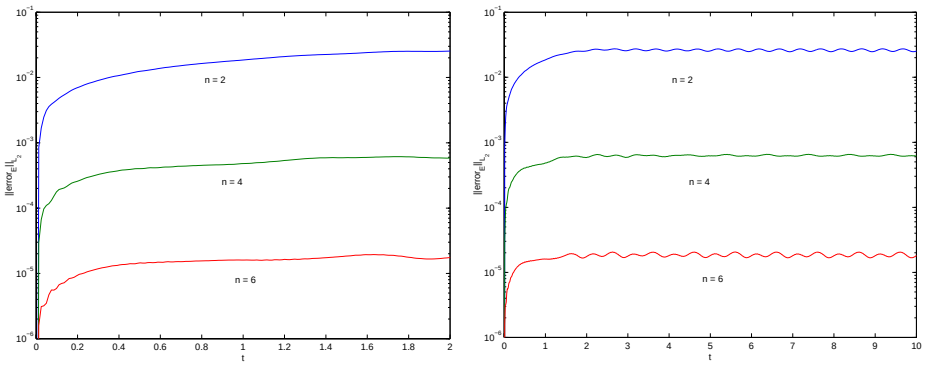

Figure 4.18. Development of the L_2-error of $\boldsymbol{E}$ during the early stages of the calculations for 2^{nd}, 4^{th} and 6^{th} order finite difference schemes with $\Delta x = 0.025$ and $\theta_i = \pi/3$.

The error for the finite difference scheme that is displayed in Figure 4.15 seems to be bounded. The method show no signs at all of error growth. Just like in the spectral scheme, the finite difference schemes all seem to converge to a certain error level, around which there is a small amount of controlled fluctuation.

The transient course of events, i.e. the error development for the first units of time, is shown in Figure 4.18. The error convergence here is somewhat slower than for the spectral scheme, but the error still settles quite early at the level where it stays for the remainder of the time where the calculation is performed. It is also evident that the error fluctuations, especially in the second and sixth order cases, occur with a frequency of $2f$, when f is the frequency of the wave itself.

5 Conclusion

Both the finite difference and the spectral methods can simulate the simple case of wave reflection and refraction at a material discontinuity in a two-dimensional rectangular geometry very accurately. For this particular geometry, the finite difference scheme is better suited because of its significantly higher efficiency.

For a more complicated and detailed geometry however, an unstructured grid would be easier to implement, and the advantages of the spectral element method would grow larger. As all spectral elements decouple, this method is also well suited for parallel implementations required for large computations.

Both the spectral scheme and the finite difference method show terrific stability properties for this test case. There is virtually no error growth as the calculation is allowed to run for a long period of time. The numerical results indicate that these methods are error-bounded, which is a very desirable property when long-term steady state calculations for applications such as radar scattering are needed.

Appendix A

The Kronecker Product

Definition 1 *Let A be a $p \times q$ matrix and let B be an $m \times n$ matrix, then*

$$A \otimes B = \begin{pmatrix} a_{0,0}B & \cdots & a_{0,q-1}B \\ \vdots & \ddots & \vdots \\ a_{p-1,0}B & \cdots & a_{p-1,q-1}B \end{pmatrix}. \tag{A.1}$$

The $p \times q$ block matrix $A \otimes B$ is called a Kronecker product.

Presented below are some useful properties of the Kronecker product.

Let A, B, C and D be matrices of arbitrary sizes, such that the specified operations are defined, then

1. $(A \otimes B)(C \otimes D) = (AC) \otimes (BD)$, (A.2a)
2. $(A + B) \otimes C = A \otimes C + B \otimes C$, (A.2b)
3. $(A \otimes B)^T = A^T \otimes B^T$, (A.2c)
4. $(A \otimes B)^{-1} = A^{-1} \otimes B^{-1}$, (A.2d)
5. $A > 0 \quad , \quad B > 0 \Rightarrow (A \otimes B) > 0.$ (A.2e)

Appendix B

Eigenvalue Calculation and Characteristic Variables

Maxwell's equations in three spatial dimensions for sourceless regions are

$$S\boldsymbol{u}_t + A\boldsymbol{u}_x + B\boldsymbol{u}_y + C\boldsymbol{u}_z = 0, \tag{B.1}$$

where

$$\boldsymbol{u} = \begin{bmatrix} \boldsymbol{E} \\ \boldsymbol{H} \end{bmatrix}, \quad S = \begin{bmatrix} \breve{\epsilon} & 0 \\ 0 & \breve{\mu} \end{bmatrix}, \tag{B.2}$$

$$A = \begin{bmatrix} 0 & -\breve{A} \\ \breve{A} & 0 \end{bmatrix}, \quad B = \begin{bmatrix} 0 & -\breve{B} \\ \breve{B} & 0 \end{bmatrix}, \quad C = \begin{bmatrix} 0 & -\breve{C} \\ \breve{C} & 0 \end{bmatrix}. \tag{B.3}$$

Here, we have the block matrices

$$\breve{\epsilon} = \begin{bmatrix} \epsilon & 0 & 0 \\ 0 & \epsilon & 0 \\ 0 & 0 & \epsilon \end{bmatrix}, \quad \breve{\mu} = \begin{bmatrix} \mu & 0 & 0 \\ 0 & \mu & 0 \\ 0 & 0 & \mu \end{bmatrix}, \tag{B.4}$$

$$\breve{A} = \begin{bmatrix} 0 & 0 & 0 \\ 0 & 0 & -1 \\ 0 & 1 & 0 \end{bmatrix}, \quad \breve{B} = \begin{bmatrix} 0 & 0 & 1 \\ 0 & 0 & 0 \\ -1 & 0 & 0 \end{bmatrix}, \quad \breve{C} = \begin{bmatrix} 0 & -1 & 0 \\ 1 & 0 & 0 \\ 0 & 0 & 0 \end{bmatrix}. \tag{B.5}$$

Equation (B.1) is re-written like

$$\boldsymbol{u}_t + S^{-1}A\boldsymbol{u}_x + S^{-1}B\boldsymbol{u}_y + S^{-1}C\boldsymbol{u}_z = 0, \tag{B.6}$$

and this can be transformed to

$$\boldsymbol{u}_t + \tilde{A}\boldsymbol{u}_\xi + \tilde{B}\boldsymbol{u}_\eta + \tilde{C}\boldsymbol{u}_\zeta = 0, \tag{B.7}$$

under the linear coordinate transformation $\xi = \xi(x, y, z)$, $\eta = \eta(x, y, z)$, $\zeta = \zeta(x, y, z)$ where $\hat{\boldsymbol{e}}_\xi$ is the outward pointing normal to a surface, and $\hat{\boldsymbol{e}}_\eta$ and $\hat{\boldsymbol{e}}_\zeta$ are the tangential unit vectors to the same surface as displayed in Figure B.1.

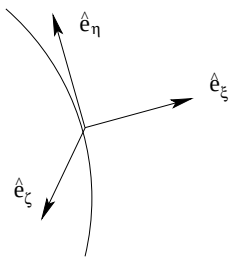

Figure B.1. General orthonormal coordinates (ξ, η, ζ). $\hat{\boldsymbol{e}}_\xi$ is the normal to a surface, and $\hat{\boldsymbol{e}}_\eta$ and $\hat{\boldsymbol{e}}_\zeta$ are the tangential unit vectors.

In this new coordinate system the matrices become

$$\tilde{A} = S^{-1}A\xi_x + S^{-1}B\xi_y + S^{-1}C\xi_z, \tag{B.8a}$$

$$\tilde{B} = S^{-1}A\eta_x + S^{-1}B\eta_y + S^{-1}C\eta_z, \tag{B.8b}$$

$$\tilde{C} = S^{-1}A\zeta_x + S^{-1}B\zeta_y + S^{-1}C\zeta_z. \tag{B.8c}$$

Characteristics are curves in $(\boldsymbol{r}, t)$-space upon which certain quantities, called characteristic variables, of a differential equation are constant. These variables are intimately connected with the solution of the equation. Characteristics entering a spatial computational domain are therefore vital as the prescribed boundary values of the characteristic variables determine the future solutions in the domain. On the other hand, characteristics that cross the border, and leave the computational region, are of no interest since their values at the boundary give no information at future times t. Finding the characteristic variables of Maxwell's equations and calculating the fluxes over an interface are both related to what happens along the direction of the interface normal. I.e., we are only interested in the action in the ξ-direction. If we discard all derivatives in the η and ζ-directions, we arrive at

$$\boldsymbol{u}_t + \tilde{A}\boldsymbol{u}_\xi = 0. \tag{B.9}$$

We can diagonalize $\tilde{A}$ with $\tilde{A} = L\Lambda L^{-1}$ in (B.9) to reach

$$\frac{\partial \boldsymbol{v}}{\partial t} + \Lambda \frac{\partial \boldsymbol{v}}{\partial \xi} = 0. \tag{B.10}$$

Here, Λ is the diagonal matrix containing $\tilde{A}$'s eigenvalues λ on the diagonal, and $\boldsymbol{v} = L^{-1}\boldsymbol{u}$ is the vector of characteristic variables where the matrix L's columns are made up of the eigenvectors of $\tilde{A}$. The six eigenvalues of $\tilde{A}$ can independently of the choice of orthonormal coordinates be found to be

$$\lambda^+ = c = \frac{1}{\sqrt{\epsilon\mu}}, \quad \lambda^- = -c = -\frac{1}{\sqrt{\epsilon\mu}}, \quad \lambda^0 = 0, \tag{B.11}$$

each with a degeneracy of two.

Since Λ is diagonal, we can write each row of (B.11) as

$$\frac{\partial v_i}{\partial t} + \lambda_i \frac{\partial v_i}{\partial \xi} = 0. \tag{B.12}$$

As mentioned, the characteristic variables $v_i(\xi, t)$ are constant along the characteristic curves, i.e.

$$\frac{dv_i(\xi, t)}{dt} = \frac{\partial v_i}{\partial \xi}\frac{d\xi}{dt} + \frac{\partial v_i}{\partial t} = 0. \tag{B.13}$$

Comparing this to equation (B.12) yields that $\frac{d\xi}{dt} = \lambda_i$, i.e.

$$\xi = \lambda_i t + C. \tag{B.14}$$

These curves in (ξ, t)-space are the characteristics, and for $\lambda^+ = c$, they are headed in the positive ξ-direction as time passes, i.e. they exit the region bounded by the surface S and head in the direction indicated by the normal vector $\hat{\boldsymbol{e}}_\xi$, while for $\lambda^- = -c$ the characteristics head in the negative ξ-direction and enter the computational domain of interest.

For our particular two-dimensional problem, we will be interested in the characteristics at the outer boundaries. As described above, we choose $\hat{\boldsymbol{e}}_\xi$ to be the outward pointing normal direction of the boundary. This means that $\xi(x, y, x)$ is

the coordinate pointing away from the specific boundary considered. Doing this, we get, at each boundary

$$\begin{aligned} &\xi_{east} = x, && \tfrac{\partial \xi_{east}}{\partial x} = 1, \\ &\xi_{west} = -x, && \tfrac{\partial \xi_{west}}{\partial x} = -1, \\ &\xi_{south} = -y, && \tfrac{\partial \xi_{south}}{\partial y} = -1, \\ &\xi_{north} = y, && \tfrac{\partial \xi_{north}}{\partial y} = 1, \end{aligned} \tag{B.15}$$

while the rest of the partial derivatives of ξ will be zero. Utilizing the variable substitutions in (B.15), we can calculate a matrix $\tilde{A}$ according to equation (B.8a) and put this into equation (B.9). After diagonalizing $\tilde{A} = L\Lambda L^{-1}$ explicitly, Λ being the diagonal matrix of the eigenvalues of$\tilde{A}$ and L being the matrix with the eigenvectors of $\tilde{A}$ as columns, we can construct $\boldsymbol{v} = L^{-1}u$ which is the vector of the six characteristic variables. As expected by the theory, it turns out that the derived characteristic variables decouple into two equivalent sets of three variables, the transverse magnetic (TM) mode including E_z, H_x and H_y, and the transverse electric (TE) mode, i.e. the set including the variables H_z, E_x and E_y. In this report, we have chosen to deal only with the transverse electric (TE) mode, and hence, explicit algebraic calculations show that our three characteristic variables picked out of $\boldsymbol{v} = L^{-1}u$ become

$$c_1^{east}(\boldsymbol{r}) = a_1^{east}\frac{1}{2}\Big(\eta(\boldsymbol{r})H_z(\boldsymbol{r}) + E_y(\boldsymbol{r})\Big), \tag{B.16a}$$

$$c_2^{east}(\boldsymbol{r}) = a_2^{east}E_x(\boldsymbol{r}), \tag{B.16b}$$

$$c_3^{east}(\boldsymbol{r}) = a_3^{east}\frac{1}{2}\Big(-\eta(\boldsymbol{r})H_z(\boldsymbol{r}) + E_y(\boldsymbol{r})\Big), \tag{B.16c}$$

at the eastern border, and equivalently

$$c_1^{west}(\boldsymbol{r}) = a_3^{west}\frac{1}{2}\Big(-\eta(\boldsymbol{r})H_z(\boldsymbol{r}) + E_y(\boldsymbol{r})\Big), \tag{B.17a}$$

$$c_2^{west}(\boldsymbol{r}) = a_2^{west}E_x(\boldsymbol{r}), \tag{B.17b}$$

$$c_3^{west}(\boldsymbol{r}) = a_1^{west}\frac{1}{2}\Big(\eta(\boldsymbol{r})H_z(\boldsymbol{r}) + E_y(\boldsymbol{r})\Big), \tag{B.17c}$$

$$c_1^{north}(\boldsymbol{r}) = a_1^{north}\frac{1}{2}\Big(-\eta(\boldsymbol{r})H_z(\boldsymbol{r}) + E_x(\boldsymbol{r})\Big), \tag{B.18a}$$

$$c_2^{north}(\boldsymbol{r}) = a_2^{north}E_y(\boldsymbol{r}), \tag{B.18b}$$

$$c_3^{north}(\boldsymbol{r}) = a_3^{north}\frac{1}{2}\Big(\eta(\boldsymbol{r})H_z(\boldsymbol{r}) + E_x(\boldsymbol{r})\Big) \tag{B.18c}$$

$$c_1^{south}(\boldsymbol{r}) = a_3^{south}\frac{1}{2}\Big(\eta(\boldsymbol{r})H_z(\boldsymbol{r}) + E_x(\boldsymbol{r})\Big), \tag{B.19a}$$

$$c_2^{south}(\boldsymbol{r}) = a_2^{south}E_y(\boldsymbol{r}), \tag{B.19b}$$

$$c_3^{south}(\boldsymbol{r}) = a_1^{south}\frac{1}{2}\Big(-\eta(\boldsymbol{r})H_z(\boldsymbol{r}) + E_x(\boldsymbol{r})\Big), \tag{B.19c}$$

for the other outer boundaries. a_i^j is a free parameter, and we will choose $a_i^j = 1$ for all i and j. c_1 is the variable that belongs to the positive eigenvalue, $\lambda = c$, and c_2 and c_3 pertain to the eigenvalues $\lambda = 0$ and $\lambda = -c$ respectively. This means that the ingoing characteristic variables, those that we are interested in, are given by c_3.

Appendix C

Flux Splitting

Let us perform the flux splitting which will explicitly yield $\hat{\boldsymbol{n}} \cdot [\boldsymbol{F}^-]$, the factor used in the penalty term in the spectral method. We can use the diagonalization procedure from appendix B to determine the numerical fluxes. The flux $\boldsymbol{F}$ is defined by the governing equation, which in our case is the set of Maxwell equations, equation (B.6),

$$S\boldsymbol{u}_t + A\boldsymbol{u}_x + B\boldsymbol{u}_y + C\boldsymbol{u}_z = 0. \tag{C.1}$$

Written on this form, the flux can be identified through

$$S\boldsymbol{u}_t + \boldsymbol{\nabla} \cdot \boldsymbol{F} = 0. \tag{C.2}$$

Now, according to the spectral scheme in (3.7), we are only interested in the flux in the normal direction to some element boundary. Performing the linear coordinate transformation $\xi = \xi(x, y, z)$, $\eta = \eta(x, y, z)$, $\zeta = \zeta(x, y, z)$ with orthonormal unit vectors $\hat{\boldsymbol{e}}_\xi$, $\hat{\boldsymbol{e}}_\eta$ and $\hat{\boldsymbol{e}}_\zeta$ as displayed in Figure B.1, the properties of linear orthonormal coordinate transformations yield

$$\begin{aligned} \hat{\boldsymbol{e}}_\xi &= x_\xi \hat{\boldsymbol{e}}_x + y_\xi \hat{\boldsymbol{e}}_y + z_\xi \hat{\boldsymbol{e}}_z \\ &= \xi_x \hat{\boldsymbol{e}}_x + \xi_y \hat{\boldsymbol{e}}_y + \xi_z \hat{\boldsymbol{e}}_z. \end{aligned} \tag{C.3}$$

$\hat{\boldsymbol{e}}_\xi$ is the outward pointing normal vector. Another important property of our orthonormal coordinates is that

$$\boldsymbol{\nabla} \cdot \boldsymbol{F} = \frac{\partial F_\xi}{\partial \xi} + \frac{\partial F_\eta}{\partial \eta} + \frac{\partial F_\zeta}{\partial \zeta}. \tag{C.4}$$

Concentrating only on the ξ-direction and aided by (C.4) we can write equation (C.2) as

$$S\boldsymbol{u}_t + \hat{\boldsymbol{e}}_\xi \cdot \frac{\partial}{\partial \xi} \boldsymbol{F} = 0. \tag{C.5}$$

Here, $\hat{\boldsymbol{e}}_\xi \cdot \boldsymbol{F}$ is the component of the flux normal to the interface. This normal flux component can be written

$$\hat{\boldsymbol{e}}_\xi \cdot \boldsymbol{F} = S\tilde{A}\boldsymbol{u}, \tag{C.6}$$

with $\tilde{A}$ given in (B.8a).

It would be of interest to decompose the flux into two parts, one being written using only the incoming characteristic variables and the other part being written in terms of the outgoing characteristic variables. $\tilde{A}$ can be diagonalized by

$$\tilde{A} = L\Lambda L^{-1} \tag{C.7}$$

where Λ contains $\tilde{A}$'s eigenvalues on the diagonal, and the columns of L are the eigenvectors of $\tilde{A}$. According to (B.11), the eigenvalues are c, 0 and $-c$, each eigenvalue occurring twice in Λ. If we split this matrix into two, i.e.

$$\Lambda = \Lambda^+ + \Lambda^-, \tag{C.8}$$

where

$$\Lambda^+ = \begin{bmatrix} c & 0 & 0 & 0 & 0 & 0 \\ 0 & c & 0 & 0 & 0 & 0 \\ 0 & 0 & 0 & 0 & 0 & 0 \\ 0 & 0 & 0 & 0 & 0 & 0 \\ 0 & 0 & 0 & 0 & 0 & 0 \\ 0 & 0 & 0 & 0 & 0 & 0 \end{bmatrix}, \quad \Lambda^- = \begin{bmatrix} 0 & 0 & 0 & 0 & 0 & 0 \\ 0 & 0 & 0 & 0 & 0 & 0 \\ 0 & 0 & 0 & 0 & 0 & 0 \\ 0 & 0 & 0 & 0 & 0 & 0 \\ 0 & 0 & 0 & 0 & -c & 0 \\ 0 & 0 & 0 & 0 & 0 & -c \end{bmatrix}, \quad \text{(C.9)}$$

we can construct the following:

$$\hat{\boldsymbol{e}}_\xi \cdot \boldsymbol{F}^- = SL\Lambda^- L^{-1}\boldsymbol{u}, \quad \text{(C.10a)}$$

$$\hat{\boldsymbol{e}}_\xi \cdot \boldsymbol{F}^+ = SL\Lambda^+ L^{-1}\boldsymbol{u}, \quad \text{(C.10b)}$$

denoted by the upwind and downwind flux respectively. The upwind flux is the one relating to the ingoing characteristics. Since we have $\hat{\boldsymbol{e}}_\xi$ oriented out of the computational domain of interest, the eigenvalue $-c$ will according to (B.14) yield a characteristic curve entering the domain.

With the observation (C.3) connecting the coordinate metrics to the normal vector $\hat{\boldsymbol{e}}_\xi$, we can perform the explicit algebraic calculations that yield the eigenvalues and eigenvectors in Λ^+, $\Lambda^-$and L. With explicit simplifying of (C.10a) and (C.10b) we can find the upwind and downwind fluxes to be

$$\hat{\boldsymbol{e}}_\xi \cdot \boldsymbol{F}^- = \begin{bmatrix} -\frac{1}{2Z}\hat{\boldsymbol{e}}_\xi \times (Z\boldsymbol{H} - \hat{\boldsymbol{e}}_\xi \times \boldsymbol{E}) \\ \frac{1}{2Y}\hat{\boldsymbol{e}}_\xi \times (Y\boldsymbol{E} + \hat{\boldsymbol{e}}_\xi \times \boldsymbol{H}) \end{bmatrix}, \quad \text{(C.11a)}$$

$$\hat{\boldsymbol{e}}_\xi \cdot \boldsymbol{F}^+ = \begin{bmatrix} -\frac{1}{2Z}\hat{\boldsymbol{e}}_\xi \times (Z\boldsymbol{H} + \hat{\boldsymbol{e}}_\xi \times \boldsymbol{E}) \\ \frac{1}{2Y}\hat{\boldsymbol{e}}_\xi \times (Y\boldsymbol{E} - \hat{\boldsymbol{e}}_\xi \times \boldsymbol{H}) \end{bmatrix}, \quad \text{(C.11b)}$$

where the impedance is $Z = \eta = \sqrt{\frac{\mu}{\epsilon}}$ and the conductance is $Y = 1/Z = \sqrt{\frac{\epsilon}{\mu}}$.

This flux-splitting works absolutely fine as long as we are dealing with continuous materials, but the question of how to deal with material discontinuities and field discontinuities due to the spectral element discretization naturally arises. In order to study this, we look at the sketch in Figure C.1. Here we denote the region to the left l for local and the one on the right n for neighbor. Below the characteristic curves λ^- and λ^+, the names of the regions switch to * and ** respectively.

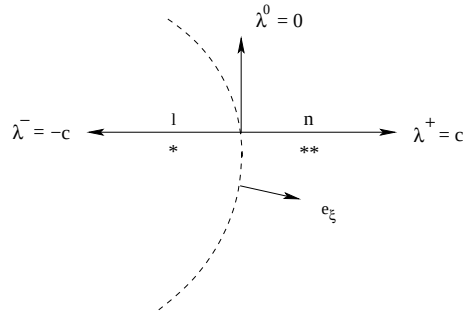

Figure C.1. Characteristics of equation (B.9) originating from a virtual boundary. When moving from region ** across characteristic λ^+ to region n, the field values satisfy the jump condition in (C.12). This also holds when moving from * to l across λ^- and from * to ** across λ^0.

Across such a characteristic curve, the following jump condition is satisfied [12]:

$$-\lambda[\boldsymbol{u}] + [\tilde{A}\boldsymbol{u}] = 0, \quad \text{(C.12)}$$

with the field variables $\boldsymbol{u}$ and the normal flux $\tilde{A}\boldsymbol{u}$ as given above and $[f] = f_2 - f_1$ denoting the jump of a variable f from region 1 across a characteristic λ to region 2.

If we use Figure C.1 and let the dotted boundary be the interface between two homogeneous isotropic dielectric materials (ϵ^l, μ^l) and (ϵ^n, μ^n), then moving from region l to region * across characteristic $\lambda^- = -c$, equation (C.12) gives

$$Z^l(\boldsymbol{H}^* - \boldsymbol{H}^l) = -\hat{\boldsymbol{e}}_x \times (\boldsymbol{E}^* - \boldsymbol{E}^l). \tag{C.13}$$

Here, Z^l is the impedance $\sqrt{\frac{\mu^l}{\epsilon^l}}$ in region l, and ($\boldsymbol{H}^*$, $\boldsymbol{E}^*$) and ($\boldsymbol{H}^l$, $\boldsymbol{E}^l$) are the fields in regions * and l respectively. In the same way, a jump over characteristic λ^+ from region n to region ** yields

$$Z^n(\boldsymbol{H}^{**} - \boldsymbol{H}^n) = \hat{\boldsymbol{e}}_x \times (\boldsymbol{E}^{**} - \boldsymbol{E}^n). \tag{C.14}$$

Jumping over the characteristic given by $\lambda^0 = 0$ from * to ** gives

$$\hat{\boldsymbol{e}}_\xi \times (\boldsymbol{E}^{**} - \boldsymbol{E}^*) = 0, \tag{C.15a}$$
$$\hat{\boldsymbol{e}}_\xi \times (\boldsymbol{H}^{**} - \boldsymbol{H}^*) = 0 \tag{C.15b}$$

which is not surprising when we think about the physical boundary conditions in (2.5a) and (2.5b). These in combination with (2.7) state that the tangential components of the fields are continuous for materials with finite conductivities, which is true in particular for dielectrica where $\sigma = 0$.

If we simultaneously solve equations (C.13), (C.14), (C.15a) and (C.15a), we come up with

$$\hat{\boldsymbol{e}}_\xi \times \boldsymbol{E}^* = \hat{\boldsymbol{e}}_\xi \times \frac{Y^l\boldsymbol{E}^l - \hat{\boldsymbol{e}}_\xi \times \boldsymbol{H}^l + Y^n\boldsymbol{E}^n + \hat{\boldsymbol{e}}_\xi \times \boldsymbol{H}^n}{\bar{Y}}, \tag{C.16a}$$
$$\hat{\boldsymbol{e}}_\xi \times \boldsymbol{H}^* = \hat{\boldsymbol{e}}_\xi \times \frac{Z^l\boldsymbol{H}^l + \hat{\boldsymbol{e}}_\xi \times \boldsymbol{E}^l + Z^n\boldsymbol{H}^n - \hat{\boldsymbol{e}}_\xi \times \boldsymbol{E}^n}{\bar{Z}}. \tag{C.16b}$$

Z is the material impedance and Y the material conductance defined as

$$Z^{l,n} = \eta^{l,n} = \frac{1}{Y^{l,n}} = \sqrt{\frac{\mu^{l,n}}{\epsilon^{l,n}}}, \tag{C.17}$$

and $\bar{Z}$ and $\bar{Y}$ are the sums of them over the interface

$$\bar{Z} = Z^n + Z^l, \tag{C.18a}$$
$$\bar{Y} = Y^n + Y^l. \tag{C.18b}$$

Looking back on (3.5), the definition of our flux, we discover that

$$\hat{\boldsymbol{n}} \cdot \boldsymbol{F} = \begin{bmatrix} -\hat{\boldsymbol{n}} \times \boldsymbol{H} \\ \hat{\boldsymbol{n}} \times \boldsymbol{E} \end{bmatrix}, \tag{C.19}$$

i.e. the normal component of the flux is nothing else than the tangential EM-field components.

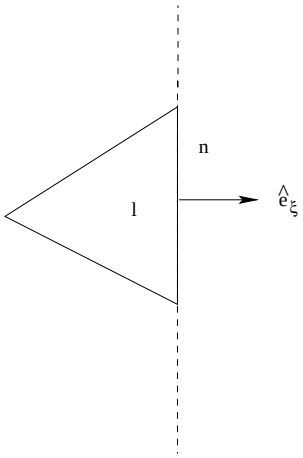

Figure C.2. Cell residing in the l-material, i.e. the material into which the characteristics corresponding to $\lambda = -c$ move. The cell face is placed right on the interface between materials l and n.

If we align a cell face with the dotted boundary defining the normal vector $\hat{\boldsymbol{e}}_\xi$ in Figure C.1 and let the simplex reside in the material on the left side, i.e. the material indicated by l or *, then we get the outward pointing normal vector $\hat{\boldsymbol{n}} = \hat{\boldsymbol{e}}_\xi$ and we can write our flux

$$\hat{\boldsymbol{n}} \cdot \boldsymbol{F} = \begin{bmatrix} -\bar{Z}^{-1}\hat{\boldsymbol{n}} \times \Big((Z^l \boldsymbol{H}^l + \hat{\boldsymbol{n}} \times \boldsymbol{E}^l) + (Z^n \boldsymbol{H}^n - \hat{\boldsymbol{n}} \times \boldsymbol{E}^n) \Big) \\ \bar{Y}^{-1}\hat{\boldsymbol{n}} \times \Big((Y^l \boldsymbol{E}^l - \hat{\boldsymbol{n}} \times \boldsymbol{H}^l) + (Y^n \boldsymbol{E}^n + \hat{\boldsymbol{n}} \times \boldsymbol{H}^n) \Big) \end{bmatrix}. \tag{C.20}$$

Now, we want to pick out the upwind flux from this, i.e. the part of the flux that coincides with the negative eigenvalues and hence the ingoing characteristics. Thus, we compare the form of (C.20) to that of (C.11) where we have calculated the upwind flux for a point in a continuous material. We see that by choosing

$$\hat{\boldsymbol{n}} \cdot \boldsymbol{F}^- = \begin{bmatrix} -\bar{Z}^{-1}\hat{\boldsymbol{n}} \times \Big(Z^n \boldsymbol{H}^n - \hat{\boldsymbol{n}} \times \boldsymbol{E}^n \Big) \\ \bar{Y}^{-1}\hat{\boldsymbol{n}} \times \Big(Y^n \boldsymbol{E}^n + \hat{\boldsymbol{n}} \times \boldsymbol{H}^n \Big) \end{bmatrix}, \tag{C.21}$$

and

$$\hat{\boldsymbol{n}} \cdot \boldsymbol{F}^+ = \begin{bmatrix} -\bar{Z}^{-1}\hat{\boldsymbol{n}} \times \Big(Z^l \boldsymbol{H}^l + \hat{\boldsymbol{n}} \times \boldsymbol{E}^l \Big) \\ \bar{Y}^{-1}\hat{\boldsymbol{n}} \times \Big(Y^l \boldsymbol{E}^l - \hat{\boldsymbol{n}} \times \boldsymbol{H}^l \Big) \end{bmatrix}, \tag{C.22}$$

we can make the forms, (C.21) and (C.11a) agree as well as (C.22) and (C.11b), for the special case when $Z^l = Z^n$, i.e. when the material varies smoothly over the element interface. We keep in mind that the boundary conditions to Maxwell's equations, i.e. (2.5a) and (2.5b), state that the tangential components of the fields $\boldsymbol{E}$ and $\boldsymbol{H}$ are continuous in the absence of surface currents. In dielectrica with zero conductivity, this is always the case. This means that we will be able to substitute $\hat{\boldsymbol{n}} \times \boldsymbol{E}$ and $\hat{\boldsymbol{n}} \times \boldsymbol{H}$, where $\boldsymbol{E}$ can mean either $\boldsymbol{E}^l$ or $\boldsymbol{E}^n$, into our upwind and downwind fluxes in (C.21) and (C.22). Hence we reach

$$\hat{\boldsymbol{n}} \cdot \boldsymbol{F}^- = \begin{bmatrix} -\bar{Z}^{-1}\hat{\boldsymbol{n}} \times \Big(Z^n \boldsymbol{H} - \hat{\boldsymbol{n}} \times \boldsymbol{E} \Big) \\ \bar{Y}^{-1}\hat{\boldsymbol{n}} \times \Big(Y^n \boldsymbol{E} + \hat{\boldsymbol{n}} \times \boldsymbol{H} \Big) \end{bmatrix}, \tag{C.23}$$

and

$$\hat{\boldsymbol{n}} \cdot \boldsymbol{F}^+ = \begin{bmatrix} -\bar{Z}^{-1}\hat{\boldsymbol{n}} \times \Big(Z^l \boldsymbol{H} + \hat{\boldsymbol{n}} \times \boldsymbol{E} \Big) \\ \bar{Y}^{-1}\hat{\boldsymbol{n}} \times \Big(Y^l \boldsymbol{E} - \hat{\boldsymbol{n}} \times \boldsymbol{H} \Big) \end{bmatrix}. \tag{C.24}$$

Now, the final formulation of the spectral scheme, (3.7), includes the difference between the upwind fluxes evaluated with the field values from the local element l and the neighboring element n. This is to measure the numerical error made at

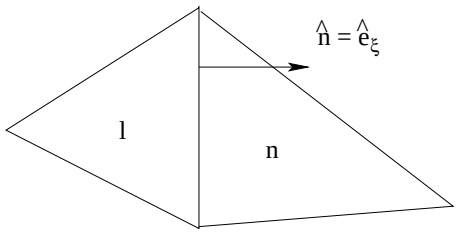

Figure C.3. Two neighboring elements at the interface.

the element interfaces and account for that by using it in the penalty term. In the real, continuous problem, the boundary conditions prescribe the continuity of the tangential fields,

$$\hat{\boldsymbol{n}} \times \boldsymbol{E}^l = \hat{\boldsymbol{n}} \times \boldsymbol{E}^n, \tag{C.25a}$$

$$\hat{\boldsymbol{n}} \times \boldsymbol{H}^l = \hat{\boldsymbol{n}} \times \boldsymbol{H}^n, \tag{C.25b}$$

but in the discrete problem, the equalities in (C.25a) and (C.25b) will not necessarily be established. Therefore, it makes sense to construct the differences

$$\hat{\boldsymbol{n}} \times (\boldsymbol{E}^l - \boldsymbol{E}^n), \tag{C.26a}$$

$$\hat{\boldsymbol{n}} \times (\boldsymbol{H}^l - \boldsymbol{H}^n), \tag{C.26b}$$

which serve as a gauge in terms of measuring the discrete numerical discrepancy from the continuous problem. Substituting these into (C.23) instead of $\hat{\boldsymbol{n}} \times \boldsymbol{E}$ and $\hat{\boldsymbol{n}} \times \boldsymbol{H}$, the differenced upwind flux formulation used in the scheme becomes

$$\hat{\boldsymbol{n}} \cdot [\boldsymbol{F}_N^-] = \begin{bmatrix} \bar{Z}^{-1}\hat{\boldsymbol{n}} \times \Big(Z^n[\boldsymbol{H}_N] - \hat{\boldsymbol{n}} \times [\boldsymbol{E}_N] \Big) \\ -\bar{Y}^{-1}\hat{\boldsymbol{n}} \times \Big(Y^n[\boldsymbol{E}_N] + \hat{\boldsymbol{n}} \times [\boldsymbol{H}_N] \Big) \end{bmatrix}, \tag{C.27}$$

where

$$[\boldsymbol{E}_N] = \boldsymbol{E}_N^n - \boldsymbol{E}_N^l, \tag{C.28a}$$

$$[\boldsymbol{H}_N] = \boldsymbol{H}_N^n - \boldsymbol{H}_N^l. \tag{C.28b}$$

and the subscript N stands for the numerical field solution.

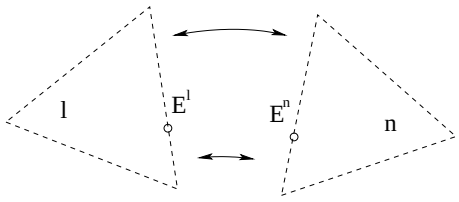

Figure C.4. Two neighboring elements split apart graphically to show the notion of the 'l' and 'n' superscripts. The values $\boldsymbol{E}^l$ and $\boldsymbol{E}^n$ are calculated for the same geometrical point $\boldsymbol{r}$, but $\boldsymbol{E}^l$ is computed in element 'l' whereas $\boldsymbol{E}^n$ is computed in element 'n'.

References

[1] D.K. Cheng, *Field and Wave Electromagnetics*, Addison-Wesley, 1989.

[2] J.D. Jackson, *Classical Electrodynamics*, John Wiley & Sons, 1999.

[3] J.S. Hesthaven, T. Warburton, *High-Order/Spectral Methods on Unstructured Grids I. Time-domain Solution of Maxwell's Equations*, ICASE Report (2001-6), 2001.

[4] J. Nordström, R. Gustafsson, *High Order Finite Difference Approximations of Electromagnetic Wave Propagation Close to Material Discontinuities*, Journal of Scientific Computing, Vol. 18, No. 2, 2003.

[5] J. Proriol, *Sur une Famille de Polynomes à deux Variables Orthogonaux dans un Triangle*, C.R. Acad. Sci. Paris 257(1957), pp. 2459-2461.

[6] T. Koornwinder, *Two-variable Analogues of the Classical Orthogonal Polynomials* in "Theory and Application of Spectral Functions", R.A. Askey ed., Academic Press, 1975, pp. 435-495.

[7] M.H. Carpenter, D. Gottlieb, S. Abarbanel, *Time-Stable Boundary Conditions for Finite-Difference Schemes Solving Hyperbolic Systems: Methodology and Application to High-Order Compact Schemes*, Journal of Computational Physics, 111:220-236, 1994.

[8] J.S. Hesthaven, C.H. Teng, *Stable Spectral Methods on Tetrahedral Elements*, SIAM Journal of Scientific Computing 21(2000), pp. 2352-2380.

[9] G.E. Karniadakis, S.J. Sherwin, *Spectral/hp Element Methods for CFD. Numerical Mathematics and Scientific Computation.* Clarendon Press, Oxford, 1999.

[10] J. Nordström, M. Carpenter, *High-Order Finite Difference Methods, Multidimensional Linear Problems, and Curvilinear Coordinates*, Journal of Computational Physics, 172:1-26, 2001.

[11] J.C. Tannehill, D.A. Anderson, R.H. Pletcher, *Computational Fluid Mechanics and Heat Transfer*, Taylor & Francis, 1997.

[12] A.H. Mohammadian, V. Shankar, W.F. Hall, *Computation of electromagnetic scattering and radiation using a time-domain finite-volume discretization procedure*, Computer Physics Communications 68(1991), pp. 175-196.

[13] A. Taflove, *Computational Electrodynamics. The Finite-Difference Time-Domain Method.* Artech House, Boston, 1995.

Issuing organisation
FOI – Swedish Defence Research Agency
Division of Aeronautics, FFA
SE-172 90 STOCKHOLM

Report number, ISRN
FOI-R–0489–SE

Report type
Scientific Report

Month year
October 2002

Project number
E 840347

Customers code
3. Aeronautical Research

Research area code
6. Electric Warfare

Sub area code
62. Stealth Technology

Author(s)
Martin Sjögren

Project manager
Jan Nordström

Approved by
Bengt Winzell
Head, Computational Aerodynamics Department

Scientifically and technically responsible
Jan Nordström

Report title
Comparison of Spectral Element and Finite Difference Methods for Electromagnetic Wave Propagation over a Material Discontinuity

Abstract
In this report, Maxwell's equations are solved for the case of an electromagnetic wave propagating over a material discontinuity. The numerical calculation of the solution to the problem is performed with a high-order spectral element method on an unstructured grid as well as with a high-order finite difference method on a structured grid. The results and errors of the two computational methods are compared, and efficiency, long-time stability and the order of accuracy are analyzed.

Keywords
electromagnetism, wave propagation, material discontinuity, spectral element method, high-order, finite difference method, efficiency, stability, accuracy

Further bibliographic information

ISSN
ISSN 1650-1942

Pages
79

Language
English

Price
Acc. to price list

Security classification
Unclassified

Utgivare	Rapportnummer, ISRN	Klassificering
Totalförsvarets Forskningsinstitut – FOI Avdelningen för Flygteknik, FFA SE-172 90 STOCKHOLM	FOI-R–0489–SE	Vetenskaplig rapport
	Månad år Oktober 2002	Projektnummer E 840347
	Verksamhetsgren 3. Flygteknisk forskning	
	Forskningsområde 6. Telekrig	
	Delområde 62. Signaturanpassning	
Författare Martin Sjögren	Projektledare Jan Nordström	
	Godkänd av Bengt Winzell Chef, Institutionen för beräkningsaerodynamik	
	Tekniskt och/eller vetenskapligt ansvarig Jan Nordström	

Rapporttitel

Jämförelse av finitdifferens- och spektralelementmetod för elektromagnetisk vågpropagering över materialdiskontinuitet

Sammanfattning

I denna rapport löses Maxwells ekvationer för en elektromagnetisk våg som propagerar över en materialdiskontinuitet. Den numeriska beräkningen av problemets lösning utförs dels av en högre ordningens spektralelementmetod på ett ostrukturerat nät och dels av en högre ordningens finitdifferensmetod på ett strukturerat nät. De två beräkningsmetodernas resultat och fel jämförs, och effektivitet, långtidsstabilitet samt noggrannhetsordning analyseras.

Nyckelord

elektromagnetism, vågutbredning, matrialdiskontinuitet, spektralelementmetod, hög ordning, finitdifferensmetod, effektivitet, stabilitet, noggrannhet

Övriga bibliografiska uppgifter

ISSN	Antal sidor	Språk
ISSN 1650-1942	79	Engelska
Distribution enligt missiv	Pris Enligt prislista	
	Sekretess Öppen	